Vortex Topology of a Pitching and Rolling Wing in Forward Flight

by

Kyle C. Johnson

A dissertation submitted to the Graduate Faculty of
Auburn University
in partial fulfillment of the
requirements for the Degree of
Doctor of Philosophy

Auburn, Alabama
December 14, 2019

Keywords: Plenoptic, PIV, Pitching, Rolling, Wing, Vortex

Approved by

Brian S. Thurow, Department Chair, W. Allen and Martha Reed Professor of Aerospace Engineering
Anwar Ahmed, Professor of Aerospace Engineering
David E. Scarborough, Assistant Professor of Aerospace Engineering
Vrishank Raghav, Assistant Professor of Aerospace Engineering
George Flowers, Dean of Graduate School

Abstract

Vortex topology is analyzed from measurements of flow over a flat, rectangular plate with an aspect ratio of 2 which was articulated in pitch and roll, individually and simultaneously. The plate was immersed into a $Re = 10,000$ flow (based on chord length) to provide forward flight component of the study. Measurements were made using a 3D-3C plenoptic PIV system to allow for the study of complete vortex topology of the entire wing. The prominent focus is the early development of the leading-edge vortex (LEV) and resulting topology. The effect of the wing kinematics on the topology was explored through a parameter space involving multiple values of pitch rate and roll rate at pitch and roll angles up to 50°. Characterization and comparisons across the expansive data set are made possible through the use of a newly defined dimensionless parameter, k_{Rg}. Termed the effective reduced pitch rate, k_{Rg} is a measure of the pitch rate that considers the relative rolling motion of the wing in addition to the pitching motion and freestream velocity. The study has found the addition of a rolling motion to a pitching wing removes the symmetries in the vortical structures, delays vortex evolution, and inhibits the extent of detachment of the LEV. Additionally, it was found that increasing the k_{Rg} parameter accelerates the evolution of the LEV, from formation to detachment, as well as advances the evolution of the LEV in nondimensionalized time.

Acknowledgments

This dissertation took a lot of time. I am fortunate that I have had such support to complete it. Thus I would like to formally acknowledge:

This dissertation:	Without having pursued this research, I would not have met my wife.
Molly:	I could not have finished without your encouragement, support, and excellent proofreading skills. Thank you for meticulously reading every one of my papers. With you, I am more than I could have ever dreamed to be.
Dr. Thurow:	I applied to Auburn out of curiosity, knowing little about it. Thank you for showing such enthusiasm and hospitality during my initial visit, it was the deciding factor for me to attend. I am grateful for all that I have learned under you guidance.
Travis	You are not only my brother, but my friend. Thanks for always being down for a beach day to help arrange my thoughts
Gary & Narda	The support you have given me throughout my life has been astounding. You have both fully backed each new endeavor I have chosen. Thank you for enabling me to get where I am today. And for answering all of my phone calls when I just want to chat.
Dr. Tim	Without your skills, I could not have conducted the experiments within this dissertation. Perhaps more importantly, thanks for going through it with me. It was nice to suffer together during the long days, all-nighters, and furniture moving.

Dr. Raghav — You are an excellent friend. Thanks for the encouragement, discussions, racquetball matches, and memorable times.

But there are more. Many more. I would like to acknowledge the following for helping me in completing this dissertation:

the AFDL	the Comittee	IHRL	Dr. Buchholz
Chris C.	Kevin W.	Tyler K.	Elise H.
Tucker the dog	Little Italy	MATLAB	Tecplot
Hopper	the HPC Team	Imperx	LaTeX
AU Water Polo	Football	the Red Barn Park	the Ocean
Airplanes	California	the Melnicks	BigHouse
the Radcliffe Estates	AeroVironment	Waterfalls	Piper the dog
Jeffrey B.	Alejandro P.	Chick-fil-a	my 2010 Ford Escape
AU ENS	CEGS		

Table of Contents

List of Figures

List of Tables

Nomenclature

α_{geo}	geometric angle of attack
$\boldsymbol{\Phi}$	optimized basis function, eigenvectors, modes
$\boldsymbol{\Psi}$	An arbitrary basis
$\boldsymbol{\Upsilon}$	an arbitrary basis
$\boldsymbol{C}$	two-point temporal correlation tensor
$\boldsymbol{u}$	a set of snapshots
$\boldsymbol{V}$	eigenvector comprised of coefficients $a(t_i)$
$\boldsymbol{X}$	a state of (x, y, z, t_n)
ϵ	noise error
ϵ_λ	noise error of swirling strength
k	reduced pitch rate
λ	eigenvalues
λ	wavelength of light in P
$\mathscr{R}$	a Fredholm Integral Operator
ϕ	spherical coordinate of P
$\phi^{(k)}(x)$	basis functions
τ	truncation error

θ	spherical coordinate of P
$a^{(k)}(t)$	time functions
D	the domain of interest
K	level of approximation
k	index of modes
P	plenoptic function
R	kernel of $\mathscr{R}$
r	correlation strenght
t	time
t_n	time steps
u	data set
V_x	x position of viewer in P
V_y	y position of viewer in P
V_z	z position of viewer in P
x	data at t
4D	four dimensional
5D	five dimensional
7D	seven dimensional
px	pixel
vx	voxel

AFDL	Advanced Flow Diagnostics Laboratory
FOV	field of view
KLT	Karhunen-Loève transform
LE	leading edge
LFIT	Light Field Imaging Toolbox
MLM	microlen mount
MP	megapixel
PCA	principle component analysis
POD	proper orthogonal decomposition
SOP	standard operating procedure
TEV	trailing edge vortex
TiV	tip vortex

Chapter 1

Introduction

1.1 Opening Remarks

The unsteady behavior of vortices present in flows over aerodynamic bodies is known to dramatically impact performance and aerodynamic loads. These flow phenomena are present in various aerospace applications including unsteady wings, aggressive maneuvers of fixed wing aircraft, rotorcraft, gas turbine engines, and wind turbines [3–9]. Additionally, there exists an extensive body of work on the elegant vortex dynamics of nature's flyers and swimmers [10–14], primarily focused on hovering flight or phenomena specific to flapping-wing flight, such as wing-body interactions, wing-wake interactions, and wing-wing interactions (e.g. "clap and fling") [3]. It has also been found that the flapping flight used throughout nature and by an increasing number of micro unmanned aerial vehicles (mUAVs) can exhibit similar vortex topology to the larger aerospace bodies [13]. Of principal interest is the leading edge vortex (LEV), which has been shown to greatly alter the flow field and, moreover, delay stall, increase lift, and increase drag. Nevertheless, few studies have addressed the formation and growth of an LEV on a revolving wing in forward flight, despite the significance throughout multiple disciplines, a few of which are shown in figure 1.1.

Of the studies that have focused on rotating wings in forward flight, the vast majority are concerning dynamic stall. Often associated with dynamic stall is the formation of a strong LEV, the dynamic stall vortex, which has been known to increase the lift production of the wing. While this event can be detrimental to the operation of helicopter rotors, wind turbines, and compressors [5, 6, 15], the LEV is fundamental to keeping the body aloft in natural and man-made flapping flight [4, 16–28]. Concerning a purely rolling wing, a handful of studies have made measurements when the wing is subjected to a freestream [29, 30]

(a) (b) (c)

Figure 1.1: Various scenarios where unsteady vortices are important: (a) high-performance aircraft such as the F-35 (b) natural flapping wing flight characteristic of the bumble bee, and (c) micro UAVs such at the AeroVironment Nano Hummingbird (all pictures from Wikipedia.)

using traditional 2D particle image velocimetry (PIV) or stereoscopic PIV. A consequence of using these measurement techniques is the arduous data collection required to produce the well-resolved three-dimensional, three-component (3D-3C) fields required to fully investigate the flow behavior and vortex structure, even utilizing phase averaging. When the pitching motion is combined with the rolling motion, there are far fewer studies that also employ a freestream flow and, those that do, are typically concerned with low Reynolds numbers and insect planforms [31, 32].

The field of rotating wings is rich with documented non-linear and intricate processes (recently reviewed by Eldredge and Jones [33]). Yet the 3D structures resulting from the combination of rotations about multiple wing axes remains less understood. Since the physical implications of such flow fields range from nature's nimble fliers to high-performance aircraft, this study seeks to examine a new dimensionless classifier for these flows. This parameter should relate the flow morphology to the body kinematics, akin to the reduced pitch rate ($k = \dot{\alpha}c/2U_\infty$) for a pitching wing and the advance ratio ($J = U_\infty/\dot{\phi}R_g$) for a rolling wing. Such an understanding will ultimately lead to insights into how to perturb the flow to achieve some desired end. Thus, the study presented here first documents the vortex topology formed by articulating an aspect ratio 2 wing in specific pitching and rolling

motions, while subjected to a $Re_c = 10000$ freestream flow. The prescribed kinematics have been selected such that the values of $k_{Rg} = \dot{\alpha}_{\text{eff}} c/2U_{R_g}$, for the simultaneously pitching and rolling cases will match the values of k for the purely pitching cases, through use of various pitch and roll rates. Additionally, the element of forward flight creates a competition of forces between: (1) the freestream velocity that convects the vortices away and (2) the rotational accelerations from wing rotation that have been shown to sustain LEV attachment. To explore the opposition between these physical factors, the parameter space encompasses a range of k, J, and k_{Rg} values, guided by past work [30] and previous dye visualization. The ranges were selected with the purpose of capturing two different classes of vortex structure as described by Garmann et al. [34]: stable leading-edge vortices and arch vortices. This dissertation seeks to describe the development of flow phenomena during the early stages of wing motion, where the flow structure is most susceptible to control and to assess the k_{Rg} parameter and draw conclusions on the physical implications of the pitch rate and roll rate on the formation of vortex structures. These goals are accomplished through use of a expansive data set of volumetric flow measurements. These results from this dataset represent what the author believe to be the first of their kind: showcasing a wide range of 3D-3C volumes, which quantitatively characterize the behavior of the LEV on a maneuvering wing.

1.2 Framework

The following thesis is organized with the goal of providing the reader with a comprehensive understanding on the findings from this research. As such, the subsequent chapters include the details of every facet.

Chapter 2 provides an extensive background and literature survey for the thesis. The chapter is divided into sections, each relevant to the final conclusions. To begin, the previous studies on flow over rotating wings is documented for pitching wings, plunging wings, rolling wings, and simultaneously pitching and rolling wings. While the thesis is focused on the findings regarding the fluid dynamics associated with a pitching and rolling wing, these

findings have only been made possible after extensive time creating and developing the processes associated with Plenoptic PIV. As such, section 2.2 describes previous work and efforts at by the author associated with light-field imaging and the realization of a plenoptic camera appropriate for PIV. The next two sections provide the details of algorithms critical for the the post processing of plenoptic images. The background is concluded with the preliminary research conducted to determine the feasibility of the experiments required to support this thesis.

Chapter 3 details the experimental arrangement of an extensive 2 week research visit to the University of Iowa to gather all of the data presented in this thesis. Also, the process of reducing the countless plenoptic images into digestible results about the flow field is explained.

Chapter 4 presents the ensemble-averaged flow fields for every combination of wing kinematics measured. These result are the crux of the thesis and represent the most extensive in the field to date. For a few cases, a glimpse into the instantaneous flow fields is provided.

Chapter 5 begins the thorough discussion and comparison of the results, with the specific goal of understanding the significance of the k_{Rg} parameter. Another method of comparing results, through correlation of vortex structure, is also used as an attempted to remove the subjectivity of comparing result. Also, the helical density of vortex structures is explored, which had been hypothesized by Wolfinger and Rockwell [35] to predict the vortex evolution of an LEV.

Chapter 6 lists the conclusions and contributions of the paper, as well as suggesting a future direction of the work.

Chapter 2

Background

The background required for this dissertation is deeply rooted in a variety of fields, yet the main focus are the contributions to the field of fluid dynamics. However, these contributions would not have been possible without the extensive research in the field of measurement science. As a result, this chapter will begin with a thorough description of related works on flow over rotating wings, then briefly discuss the development of the measuring system and related post processing techniques (much of which is left for the appendices), and conclude with a description of the preliminary experiments that were conducted to support this dissertation.

2.1 Flow Over Rotating Wings

Unsteady wings have various applications across multiple disciplines. In the most familiar application of a rotating wing, a helicopter, an airfoil is rotated as shown in figure 2.1a. The wing rotation becomes steady when maintaining a hover in quiescent air. A wind turbine, seemingly similar to rotorcraft, actually has a different type of rotation, shown in figure 2.1b. Here the incident wind flows over the airfoil, in which the lifting force causes the turbine to rotate in the direction of the lift force. For a steady wind, the rotational rate is constant. However, the same type of rotation is employed by natural flyers, such as birds and insects, to create lift. This leaves one final axis for rotation, shown in figure 2.1c. This type of rotation, often called "pitch-up", is employed by natural flyers as part of the flapping motion. Thus, this dissertation chooses to focus on the vortex dynamics of the rolling motion (figure 2.1b) and the pitching motion (figure 2.1c). However, there exist many similarities between flapping flight and the rotation shown in figure 2.1a at similar Reynolds numbers. It

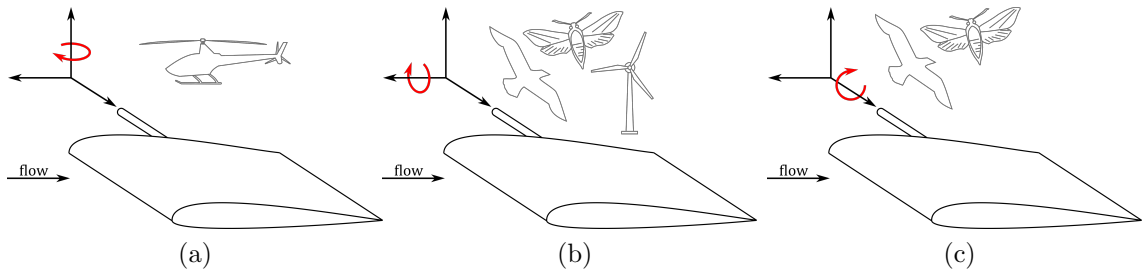

Figure 2.1: Schematic of common types of wing rotation

is worth mentioning a handful of studies that use rotorcraft-like rotation to study the effects of rotation on the LEV [5, 6] and designing a higher endurance rotary wing mUAVs [36].

2.1.1 Pitching Wings

A purely pitching wing has long been associated with the phenomenon of dynamic stall. When the wing is pitching rapidly compared to the direction of the airflow, a strong LEV is formed, which increases the lift production of the wing. However, when the vortex has been shed and is no longer over the surface of the wing, the airfoil is in stall and the lift production dramatically reduces. Dynamic stall is also found on helicopter rotors when in forward flight [5, 6, 15]. In natural and man-made flapping flight, dynamic stall is the key to augmented lift production often required to keep the body aloft [4, 16–27].

The flow regimes associated with a purely pitching wing are primarily function of the reduced pitch rate, the aspect ratio of the wing, and the center of rotation. The reduced pitch rate is defined as the ratio of the angular velocity at the mid chord versus the freestream velocity, mathematically: $k = \dot{\alpha}c/2U_\infty$, where $\dot{\alpha}$ is the rate of change of the geometric angle of attack, α_{geo}. Thus, a faster pitch rate corresponds to a larger reduced pitch rate, which is well-known to tighten the resulting LEV [17, 37]. At low aspect ratios ($AR < 8$), a pitching wing gives rise to 3D vortical structures and 3D flow fields [4, 38]. When the aspect ratio of the wing is increased, the 3D effect from the tip vortices is reduced and LEV is allowed to detach from the wing earlier compared to smaller AR cases [20]. Additionally, it is noted that spanwise flow through the vortex core can still exists in large AR and nominally 2D cases

[17, 38]. Changes in the center of rotation most notably produces a higher peak lift as the rotational axis is shifted closer to the leading edge (LE) [17]. Vortex topology resulting from the pitch-up maneuver is primarily a function of the reduced pitch rate. At substantially low reduced pitch rates ($k < 0.03$), an LEV does not form [17]. Further investigations into the 3D vortex topology are largely driven by flow visualization, however, stereoscopic PIV measurements made by Yilmaz and Rockwell [4] are most similar to this dissertation, characterizing the vortex evolution for an aspect ratio 2 plate at $k = 0.098$. For this scenario, the LEV is found to lift up from the surface of the wing in the middle region of the span, creating an arch-like structure. This behavior is seen as early as 27° and becomes more pronounced through 36° and 45°. This highly 3D LEV interacted with the wing tip vortices, contrasting the canonical 2D LEV often associated with dynamic stall.

Jantzen et al. [20] utilize an $AR = 2$, 4 and nominally 2D flat plate at reduced pitch frequencies of $k = 0.065$–0.39 for a physical and computational experiment. The physical experiment immersed the wings in a Re =20,000 flow whereas the computational experiments had a significantly lower Re =300. While the physical experiments are suitable for comparison to the present dissertation, the 3D vortex topology is presented only for the computational experiment, where the Re is 2 orders of magnitude lower than the present dissertation. Regardless, the vortex topology was characterized by the formation of a vortex loop combining the LEV, trailing edge vortex (TEV), and the two tip vortices (TiVs), before 38° of pitch. Also at this time in the pitching motion, a slight arching to the LEV is visible, although it is far less pronounced than the structure from Yilmaz and Rockwell [4]. Similarities were found in plots of aerodynamic coefficients despite the disparity in Re, but this does not guarantee that the vortex topology development is similar. Through comparison of dye injection in the physical model and vorticity magnitude contours in the computational results, some similarities are observed in the formation of the LEV, but there are noticeable differences. In the physical experiment, structures are shed from the LE, while this is not apparent in the computational results.

A flow visualization study using a parameter space most similar to this dissertation, ($k = 0.1$–0.35 and $AR = 2$) shows a distinct arch structure to the LEV as early as 26° [27]. In addition, the authors note that similar structures are seen at later times in the pitching motion as the reduced pitch rate is increased. Specifically, similarities in vortex structure are seen at $\alpha_{\text{geo}} = 25°$, $\alpha_{\text{geo}} = 40°$, and $\alpha_{\text{geo}} = 25°$ when $k = 0.1$, 0.2 and 0.5, respectively. A crucial difference between this dissertation and the present dissertation is prescribed wing kinematics. Yilmaz et al. [27] imposed a pitch-up motion from $\alpha_{\text{geo}} = 0°$ to 40°, a brief pause, and a pitch-down motion from $\alpha_{\text{geo}} = 40°$ to 0°. Thus, the similar vortex structure for the $k = 0.5$ case was actually at $\alpha_{\text{geo}} = 25°$ while pitching down. This dissertation does not employ a pitch down motion. Additionally, Yilmaz et al. [27] move the location of the center of rotation and found a similar shift to the vortical structures, although this was not explored in this dissertation. It was proposed that changing these parameters simply induces a time shift to the structures, specifically, increasing the reduced pitch rate by a factor of 3.5; corresponding to advancing a structure in time by a factor of about 2 convective times [27]. In a similar manner, Granlund et al. [17] describe a collapse of maximum lift coefficient when plotted against time normalized by convective time. Their experiments were performed using a force balance and rhodamine dye visualizations for various values of K ranging from 0.01–0.5 in a uniform freestream. Again, similarities are found across the range of K and center of rotation; qualitatively suggesting a time-shifting of the vortical structures, as similar to Yilmaz et al. [27].

2.1.2 Plunging Wings

Although the kinematics were not explicitly prescribed in this dissertation, the vortical structures formed by a plunging or purely translating plate show many similarities to both independent and simultaneous pitching and rolling maneuvers. Of the many studies on periodically plunging air foils [39–41], the work of Akkala and Buchholz [42] proves useful for comparison as the plunging plate was immersed in a freestream and stereo PIV was used

to reconstruct a phase-averaged 3D flow field. While Akkala and Buchholz [42] focused on the vorticity transport mechanisms associated with the flow, vortex topology is also presented, detailing a strong tip vortex (TiV) and LEV. Throughout the downstroke, the LEV stays pinned at the tip, where it is interacting with the TiV. Inboard of the tip, the LEV lifts away from the wing surface, forming an arch-like structure which has been observed by other studies [27, 43, 44]. Notable for the present dissertation, the isocontours marking the TiV no longer connect to the isocontours marking the pinned LEV, at the later stages in the motion, although the LEV does not appear to be dramatically affected.

A study by Baik et al. [45] immersed a 2D flat plate in a freestream and articulated the plate in both plunge and pitch, simultaneously. This scenario is interesting for comparison because it has effectively removed the spanwise variation caused by rolling motion. From stereoscopic PIV measurements at a single plane, it was concluded that the vortex topology and evolution is far more sensitive to changes in the reduced pitch rate k than the plunging rate, where the plunging rate corresponds to the Strouhal number $St = fL/U$. For a fixed k, it was found that increasing St increases the maximum circulation of the LEV, attributed to the increased motion speed. Specifically related to the vortex evolution of the flow, it was observed that throughout the parameter space, the LEV would continue to grow, resulting in the downstream motion of the reattachment point of the separated flow. When the reattachment point reaches the TE, the recirculation region opens and the LEV separates from the LE. However, due to the 2D nature of these experiments, comparisons will be limited, not only by the single plane of measurements, but also the absence of finite wing effects.

2.1.3 Rolling Wings

A purely rolling wing produces flow regimes primarily dependent on advance ratio, aspect ratio of the wing, and the radius of the gyration. The advance ratio is defined as the ratio of the freestream velocity and the angular velocity at the radius of gyration,

mathematically given as: $J = U_\infty/\dot{\Omega}R_g$, where R_g is the radius of gyration, defined as the distance from the roll axis to the midspan. While the pitching maneuver establishes a uniform angular velocity across the leading edge, a purely rolling wing creates a linear variation of angular velocity along the span, which induces an angle of attack, α_{ind}. Thus, an effective angle of attack is defined as $\alpha_{\text{eff}} = \alpha_{\text{geo}} + \alpha_{\text{ind}}$, where $\alpha_{\text{ind}} = \text{atan}(J)$. The effective angle of attack is formally defined at the radius of gyration, however, it is essentially a function of the angular velocity, and varies linearly along the span of the wing. A detailed analysis by Lentink and Dickinson [46], worked on identifying and simplifying the parameter space of rotating wings, ultimately verifying that the Rossby number ($Ro = (J^2 + 1)AR$), which can be thought of as a measure of the Coriolis acceleration, is a useful metric to predict flow morphology. Since the aspect ratio is held constant in the present dissertation, the advance ratio is sufficient for comparison.

Lentink and Dickinson [47] followed up their theoretical analysis with a detailed experimental analysis using bubble visualization and force balance measurements on the planform of a fruit fly in a hovering scenario, concluded that the LEV is stabilized by a spanwise flow, seemingly independent of the rotational Reynolds number ($100 \leq Re \leq 1400$). It is suggested that the spanwise flow is driven by a pressure gradient force within the LEV and centrifugal pumping outside the vortex, from root to tip, which also convects the LEV into the tip vortex. Through the simultaneous force balance measurements and visualization, is that the LEV continues to augment lift, even after the vortex has burst. The authors summarize the findings of the two papers in stating that "the single condition for LEV stability and maximal force augmentation appears to be a sufficiently low Rossby number" suggesting that many flying and swimming animals should be able to generate a stable LEV. This implies that a lift augmentation through the stably attached LEV is a convergent solution in nature.

Of the work on rolling wings, the majority investigate a wing immersed in quiescent fluid ($J = 0$), many of which describe the development and attachment of the LEV to be

relatively insensitive to *Re* or *AR*. Multiple factors have been suggested to stabilize the LEV and prevent it from convecting away from the LE during the rolling motion, such as spanwise flow through the LEV [35] and through vorticity annihilation [48]. More specifically, Wojcik and Buchholz [48] utilized a vorticity transport analysis on stereoscopic PIV results made on a rotating $AR = 4$ wing at a $Re_{\text{rot}} = 4000$ for $\phi = 75^\circ$ to 320° at $\alpha_{\text{geo}} = 35^\circ$. However, it has been suggested by the authors that vorticity annihilation could be a suitable mechanism for maintaining the stability of the LEV in the kinematics prescribed in the present dissertation. Thus, the vorticity transport equation is given below in equation 2.1, which will be considered in the results presented herein. Most relevant to this dissertation are the in-plane convective flux term (closely related to the shear layer flux), the Coriolis term (described by Lentink and Dickinson [46] to be an important factor), and the diffusive flux from the wing surface (closely related to the secondary vorticity).

$$\underset{\text{vortex tilting}}{\int_A \left(\omega_x \frac{\partial u_z}{\partial x}\right)} + \underset{\text{spanwise convection}}{\int_A \left(\omega_y \frac{\partial u_z}{\partial y} - u_z \frac{\partial \omega_z}{\partial z}\right) \mathrm{d}A} - \underset{\text{in-plane convective flux}}{\oint (\vec{u} \cdot \vec{n}_{\partial A}) \omega_z \mathrm{d}s} + \underset{\text{Coriolis}}{2 \int_A \Omega_x \frac{\partial u_x}{\partial x} \mathrm{d}A} + \underset{\text{diffusive flux from surface}}{\frac{1}{\rho} \int_{\text{W.S.}} \frac{\partial p}{\partial x} \mathrm{d}x} = \frac{\mathrm{d}\Gamma_z}{\mathrm{d}t} \tag{2.1}$$

It is further hypothesized that the impediment of these control mechanisms can result in convection of the LEV from the LE and eventual degradation of the structure [35, 48]. It should be noted that this degradation of the LEV is fundamentally different than the phenomena of vortex "bursting", which has been found to occur at roll angles on the order of 100° [49, 50], well beyond the maximum angle of this dissertation.

Two similar computational studies, Garmann et al. [34] and Garmann and Visbal [51] used a high fidelity, implicit large eddy simulation technique to numerically estimate the fluid motion of a revolving plate in quiescent with a fixed geometric angle of attack at various rotational Reynolds numbers. The results were compared to similar simulations of a plunging plate and experimental PIV results [52] for validation. It was found that for the range of *Re* explored ($200 \leq Re \leq 60000$), that the development and attachment of

the LEV was relatively insensitive to Re. It was also observed that the LEV would detach near the tip and reconnect with the tip vortex. LEV breakdown was observed at $Re \geq 2000$ and often associated with the reversal of spanwise flow through the vortex core. This flow is often referred to as a "stabilizing jet" through the vortex core from root to tip and the observation that the reversal of this jet is associated with the vortex breakdown aids to the hypothesis [53–55]. In the comparison to the purely translating plate, it was noted that both the root and tip corners of the vortex unpinned; causing the entire LEV to detach sooner than the purely rolling case, which stayed anchored by the root corner of the LEV. Another important finding from the numerical study is that the pressure forces were an order of magnitude larger than the Coriolis and centrifugal forces. Additionally, the Coriolis force was resolved to be away from the surface of the wing, indicating that is not a factor in keeping the LEV attached. Similar behavior was seen when the Re was held constant and the aspect ratio was varied (AR = 1,2,4) [51]. Furthermore, these findings are in agreement with the stereo PIV experiments of Carr et al. [56] who used a nearly identical set up and Harbig et al. [57] who simulated the planform of a fruit fly wing at a fixed geometric angle of attack in a similar rotational motion through quiescent air with direct numerical simulation (DNS). The experimental study of Carr et al. [56] used a rotating various flat plates in a quiescent tank used stereo PIV to define the vortex structure of the entire plate. Through phase-locking and phase-averaging, the 3D vortex structure, defined by Q-criterion, was described to show outboard lift-off and inboard stability of the LEV. As the outboard portion of the LEV lifts off, another forms and connects to the tip vortex. This description was found to be independent of aspect ratio. These results have good agreement with the computational work of Garmann & Visbal [51] and the experiments of Ozen and Rockwell [52].

The 3D vortex topology of a rolling wing in a quiescent fluid is characterized by Wolfinger and Rockwell [35] using stereoscopic PIV. The same wing was rotated at 2 different radius of gyrations such that the angular velocity at each radius of gyration was identical, resulting in roll rates $\dot{\phi} = 3.06$ and 0.53 for the shorter and longer R_g/c, respectively. The roll rate of the

longer radius of gyration ($R_g/c = 4.7$) is within the range of roll rates used in this dissertation ($\dot{\phi}$ =0.42–1.05). Throughout the motion, Wolfinger and Rockwell [35] characterize the LEV structure as evenly distributed along the LE, conical in shape from root to tip along the LE, and an arch vortex. Early in the motion, the LEV of smaller R_g/c is characterized as conical while the LEV of the larger is characterized as evenly distributed. Focusing on the evolution of the LEV of the larger, at about 23° of roll, the LEV begins to lift up from wing surface in the middle third of the span, but remains "pinned", or close to the wing, at the ends of the LE. As the motion continues to 31°, a distinct arch vortex has formed, remaining pinned. Throughout the rest of the motion, up to 85°, the arch vortex moves down the chord of the wing, with the legs slowly pinching, or moving closer together, leading to the eventual convection of the structure off of the wing.

When a freestream is introduced, Bross et al. [30] note that the vorticity concentration is relatively independent of advance ratio (J =0–0.537) in the early to intermediate stages of rotation ($\phi < 45°$), although, this observation is made only at the midspan plane. Representations of the 3D vortex structure are created by stitching 38 stereoscopic PIV imaging planes together, specifically for the $J = 0.537$ case at $\phi = 36°$, useful for comparison to this dissertation. Bross et al. [30] describe a dual-vortex system at the LE, that extends from about 40 percent of the span to the tip. In board of this point, the LEV deflect up and away from the wing root. Additionally, the TiV is well defined and shown to have a helical instability about its periphery. It is hypothesized that adding a freestream velocity may shift the timing of formation of a loop vortex connecting the TiV to the root. While this idea of a time-shift is fundamentally different than that proposed by Yilmaz and Rockwell [4] regarding the LEV of a pitching wing, it is an intriguing outcome to changing various parameters governing both pitching and rolling wings. Furthermore, Bross et al. [30] note that the streamline topology of the flow over the wing shows generic features over $J = 0$–0.537, but the roll angle ϕ at which the features occurred did depend on the value of J. While

not explicitly defined as a time shift in the sense of Yilmaz et al. [27], this shifting of flow features over ϕ is similar in nature.

2.1.4 Combined Pitching and Rolling

A simultaneously pitching and rolling wing produce flow regimes that are a function of all of the previously mentioned factors: reduced pitch frequency, advance ratio, aspect ratio, radius of gyration, and center of rotation. Additionally, the effective angle of attack can be defined as $\alpha_{\text{eff}} = \alpha_{\text{geo}}(t) + \alpha_{\text{ind}}$, where the geometric angle of attack is changing as a result of the pitching maneuver. It follows that $\dot{\alpha_{\text{eff}}} = \dot{\alpha_{\text{geo}}}$, when the roll rate is held constant. Combining the pitching motion with a rolling motion has primarily been studied with the motivation of understanding biological flight, almost exclusively in the hovering scenario. Using the planform of a fruit fly, Birch and Dickinson [31] compared the precise flow structure of the stable LEV to that of the hawkmoth, studied by Van den Berg and Ellington [58]. Contrary to other findings, it was found that for the lower Reynolds numbers and simultaneous rolling and pitching of the fruit fly wing that the LEV was stable without separation, a stark contrast to previous findings of the higher Reynolds number, purely rolling, hawkmoth wing. A computational study mimicking the study of Birch & Dickinson used an in-house CFD solver capable of 'flying' an insect model with morphologically dynamic wings that exhibit a simultaneously rolling and pitching stroke pattern [32]. This study confirmed the findings of Birch & Dickinson. A previous computational study was conducted with a 2D rolling and pitching fruit fly wing and found similar results as well [59]. Again, all of these studies have focused on hovering flight, making a comparison of advance ratio and reduced pitch frequency unsuitable to the proposed study.

Most relevant to this dissertation, Phillips et al. [60] utilized high-speed, stereoscopic PIV to study the 3D vortex structure from an insect-like flapping machine, aptly named the "flapperatus," finding that across a range of *AR*, the flow fields developed nearly identically, qualitatively characterized by a conical LEV that arches at the outboard end of the wing.

As the stroke progressed, the LEV would eventually detach at about 70 percent of the span, moving progressively inboard as the stroke continues. The remainder of the body of work is focused on low *Re* flow of insects or animals [32, 54, 55, 58, 59, 61], including rotating actual animal wings [62, 63], each with substantial variation from the work presented herein.

2.2 Light-Field Imaging

This section provides a brief overview on light-field imaging and the construction of a plenoptic camera, however, extensive documentation and procedures are included in Appendix B.

The plenoptic camera has become an appealing solution for optical flow diagnostics since it enables the rapid acquisition of light-field data with a single camera. As described by Levoy, a light field constitutes both the spatial and angular information about the light rays in a scene [2]. A plenoptic camera was first suggested as a tool to capture the light field by Adelson and Bergen [64], and later realized in a compact form factor by Ng [65]. While a conventional camera focuses light directly onto the image sensor (figure 2.2a), a plenoptic camera records the light field by focusing the light entering the aperture of the main lens onto an array of microlenses (figure 2.2b). The microlens then focus the light onto pixels on the image sensor, based on the angle that the light entered the main lens. Thus, 3D information of a scene is encoded into a plenoptic image.

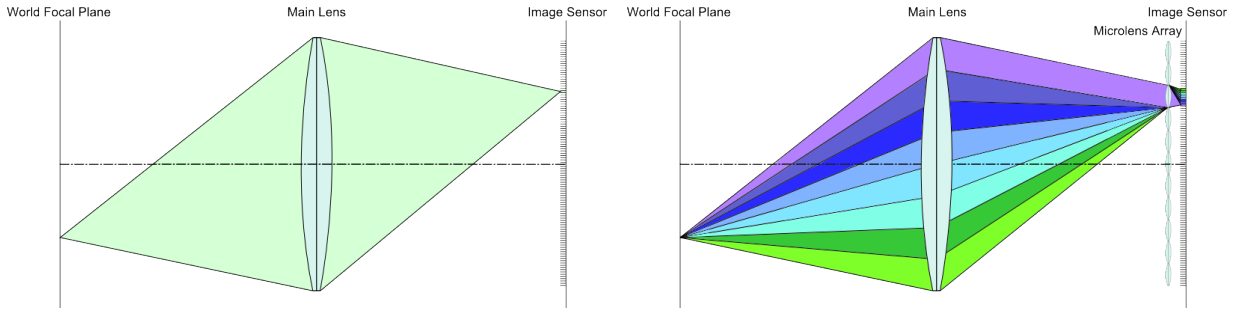

(a) (b)

Figure 2.2: A schematic comparing how a conventional camera (a) and a plenoptic camera (b) record a point source of light on the world focal plane

The plenoptic camera used in this study was constructed from a 29 megapixel (MP) Imperx Bobcat ICL-B6640 conventional camera with square pixels 5:5 microns in size. A microlens array was manufactured by Jenoptik to have a focal length of 308 microns and a microlens pitch of 77 microns, seen in the exploded view of figure 2.3.

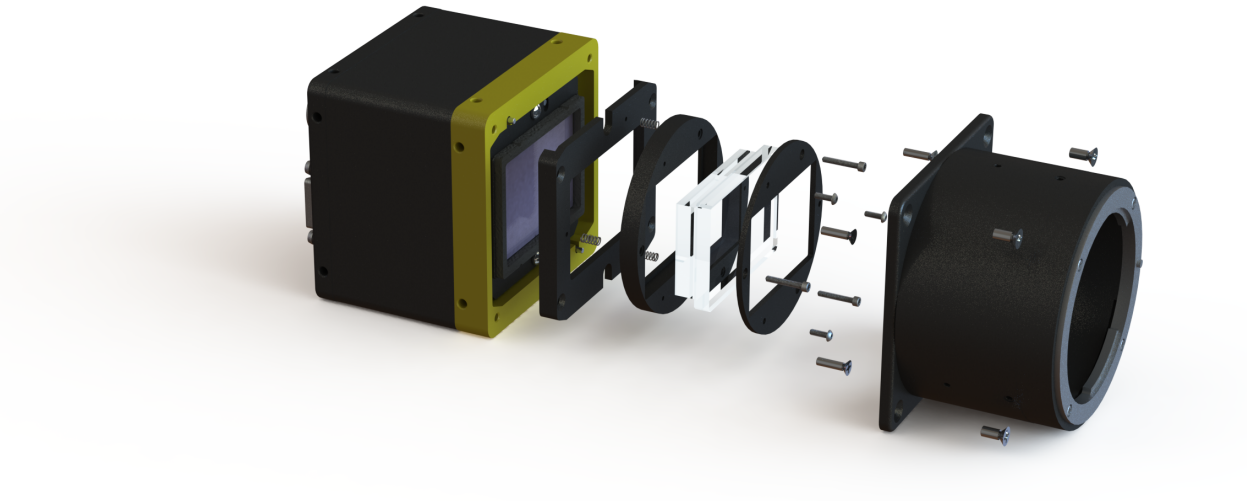

Figure 2.3: Rendering of an exploded view of the plenoptic camera built at Auburn University

A sample image taken with plenoptic camera is shown in figure 2.4. The plenoptic camera was set up in the laboratory and three standard playing cards were placed such that the 6 of hearts (left) and the king of clubs (right) were located at the same depth separated by a small gap. Further from the camera, the queen of spades was visible through the gap between the two other cards. The plenoptic image resembles a normal image but lacks the sharpness, due to the microlens array spreading out the light. By examining the enlarged region of the spade symbol shows many "microimages", or the image formed behind each microlens. The hexagonal arrangement of the microlenses is clear. Notably, the edge of the spade is quite blurry, despite being nominally in focus. This is a result of multiple microlenses having a line of sight to the edge of the spade, thus spreading the information out on the image sensor, making the image apparently blurry. However, by close examination of a micro-image, a hard edge can be seen, depicting the edge of the spade symbol.

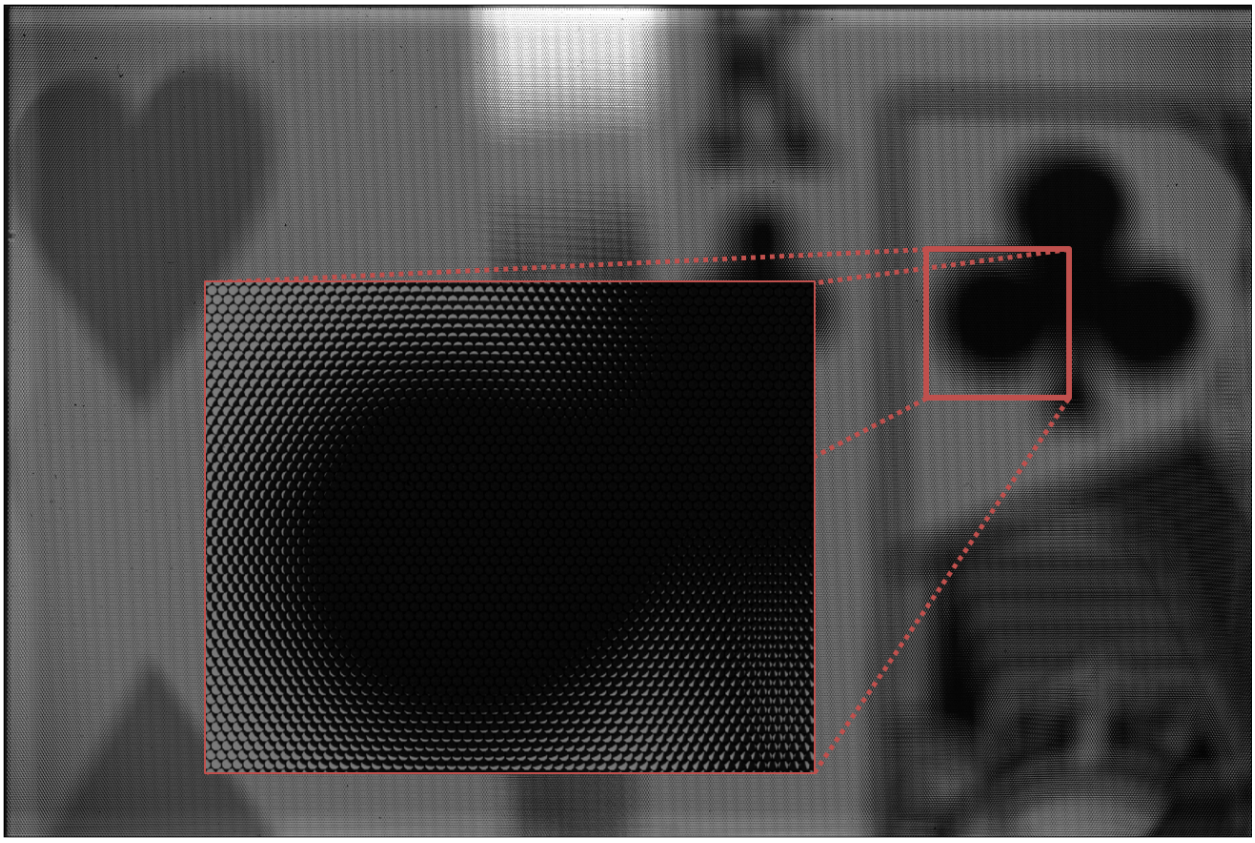

Figure 2.4: A raw plenoptic image from the 29 MP camera with a rectangular array displaying a scene of objects in the laboratory; the inset shows the micro-images formed by the each of the microlenses

The information embedded in this image can be extracted computationally to create new images, shown in figure 2.5. Each image was created from the single snapshot shown in figure 2.4. The first two images show the leftmost and rightmost perspectives of the scene, as captured through the aperture of the main lens. The parallax is elegantly demonstrated by the amount of the queen's face that is visible. In the leftmost perspective, only the right half of the queen's face is visible, as the right half is obscured by the 6 of hearts. In the rightmost perspective, the entire left half of the queen's face and more is visible. Additionally, the entire scene is in focus in theses perspective images, as the images are assembled by combining one pixel from behind each microlens to make a new image. The location of the pixel relative to the center of microlens determines the angle of the perspective image. The entire field of view (FOV) is in focus, because the use of one pixel has limited the effective aperture to essentially

a pinhole. The two remaining images show a shift of the nominal focal plane, such that the front two cards are in focus (figure 2.5c) and the queen is in focus (figure 2.5d). This process is an integrated one, which uses a shifted image sensor plane and for each pixel on this plane, sums the intensities recorded by the pixels on the nominal sensor plane which the light ray passed through the pixel on the shifted sensor plane. This clearly illustrates that depth information is encoded into each plenoptic image, which can be extracted computationally.

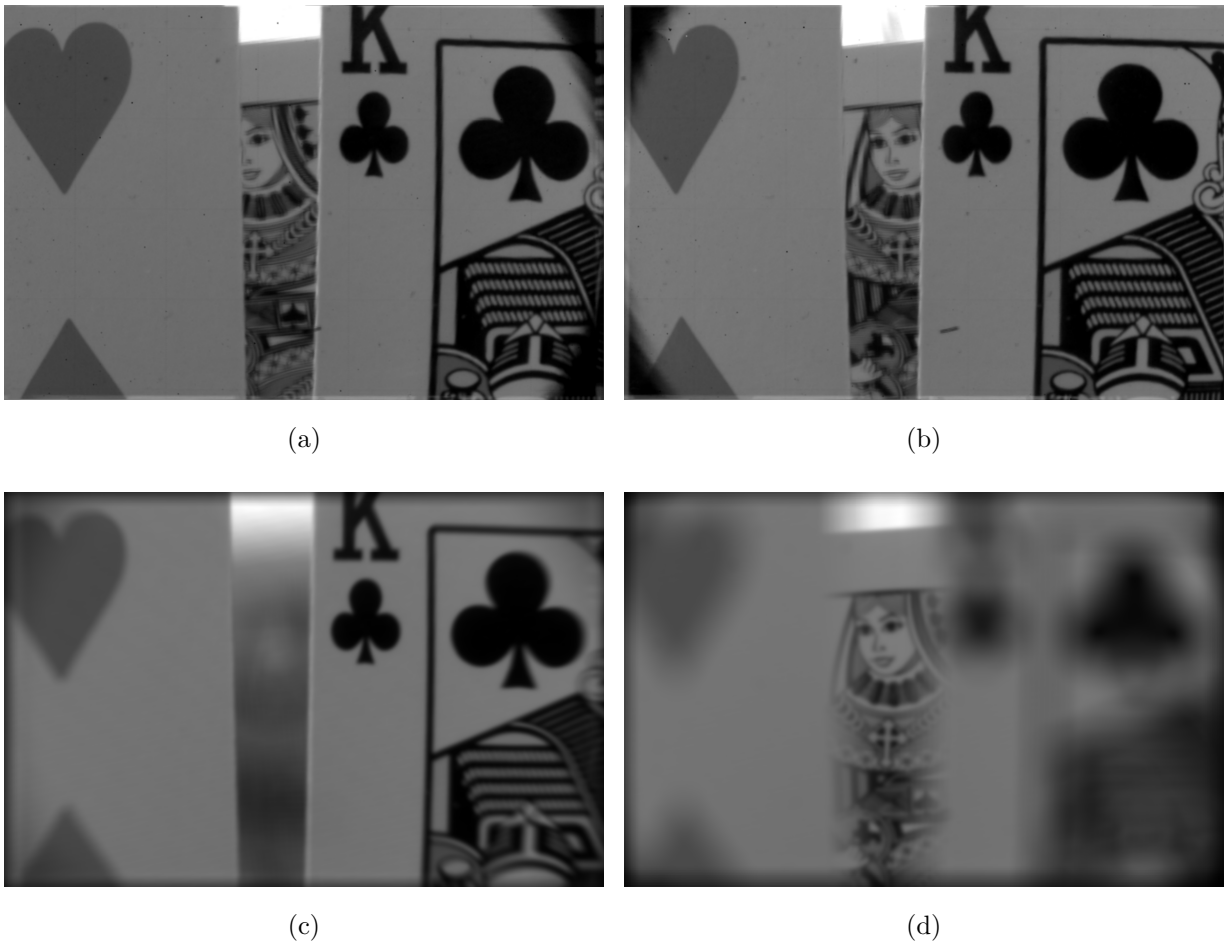

(a) (b)

(c) (d)

Figure 2.5: (a) A left perspective of the scene (b) a right perspective of the scene (c) focused on the King in the front of the scene (d) focused on the Queen in the back of the scene

The Advanced Flow Diagnostics Laboratory (AFDL) of Auburn University has constructed several plenoptic cameras for a wide variety of applications, including plenoptic PIV. The next subsection, §2.3, serves as a brief summary of the plenoptic PIV and the

reconstruction technique, which is more completely described by Fahringer et al. [66]. To assist with many of the other applications of the plenoptic camera, including the images generated in figure 2.5, the AFDL has created the Light Field Imaging Toolbox (LFIT), an open source MATLAB package designed to handle light field images [67].

2.3 Plenoptic PIV

The plenoptic camera functions similarly to standard PIV cameras, recording image pairs of an illuminated volume. The images are a two-dimensional (2D) representation of the illuminated 3D volume. Thus, when compared to traditional PIV, there is an additional step of reconstructing the 2D plenoptic images into 3D volumes. Tomographic reconstructions are created using an implementation of the multiplicative algebraic reconstruction technique (MART), similar to the algorithm used for tomographic PIV. The process is detailed by Fahringer et al. [66]. This reconstruction technique iteratively solves a system of linear equations that model the imaging system, shown in equation 2.2. This equation can be thought of as the projection of the volume intensity distribution $E(x, y, z)$ onto a 2D image $I(x, y)$. However, the reverse of this operation is required to obtain a volume $E(x, y, z)$ from the image $I(x, y)$. Thus, $E(x, y, z)$ is initially defined as a volume discretized into cubic voxels (vx, volume equivalent of a pixel), each with an intensity of 1. Each voxel j can then be projected onto a pixel located at (x_i, y_i), mathematically expressed by

$$\sum_{j \in N_i} w_{i,j} E(x_j, y_j, z_j) = I(x_i, y_i) \tag{2.2}$$

where N_i is the number of voxels in the line-of-sight of the ith pixel and $w_{i,j}$ is the weighting function, which describes what portion of light emitted from a voxel strikes each pixel. The weighting function of a plenoptic camera is different from cameras used in tomographic PIV because the entire volume is not in focus during plenoptic PIV. Thus, a novel approach to create the weighting function was developed by Fahringer et al. [66].

Equation 2.3 describes the iterative procedure used to determine a solution for $E(x_i, y_i, z_i)$, known as the MART Equation. Each $k^{\text{th}} + 1$ iteration is defined as

$$E(x_i, y_i, z_i)^{k+1} = E(x_i, y_i, z_i)^k \left(\frac{I(x_i, y_i)}{\sum_{j \in N_j} w_{i,j} E(x_i, y_i, z_i)^k))^{\mu w_{i,j}}} \right) \tag{2.3}$$

where μ is the relaxation parameter which can range between 0 and 1. Convergence is determined by manual inspection of the particle volumes. Fahringer et al. [66] present results from this process for both simulated and experimental data. Once the plenoptic data has been reconstructed into a 3D intensity distribution, cross-correlation techniques are applied in an identical fashion to tomographic PIV.

A recently developed volumetric calibration for the plenoptic camera was performed by imaging a dot card placed at various depths throughout the measurement volume [68], shown in figure 2.6. This procedure, the so-called "direct light field calibration" (DLFC) is not a traditional volumetric de-warping. Instead, the dot card images are used to create a least-squares polynomial fit to define a mapping function from a point in object space to a point on the image sensor. The dot cord is traversed through the measurement volume, as shown in figure 2.6, equating the physical space to image space. The errors in this method are estimated to be less than .1% of the reconstructed volume size in the lateral directions x, y and 1% in the depth direction z [68]. In more recent advancements, it has been shown that this mapping function can be substituted for the weighting function for MART reconstructions to improve computational efficiency. Another group [69] has recently published a similar method of using a plenoptic camera to make 3D-3C PIV measurements, which they call 'light-field imaging based PIV' (LF-PIV), which is essentially the same as plenoptic PIV presented here. Additionally, Rice et al. [70] and Shi et al. [71] have both recently performed a comparison study using a traditional tomographic PIV set-up and a plenoptic and LF-PIV', respectively.

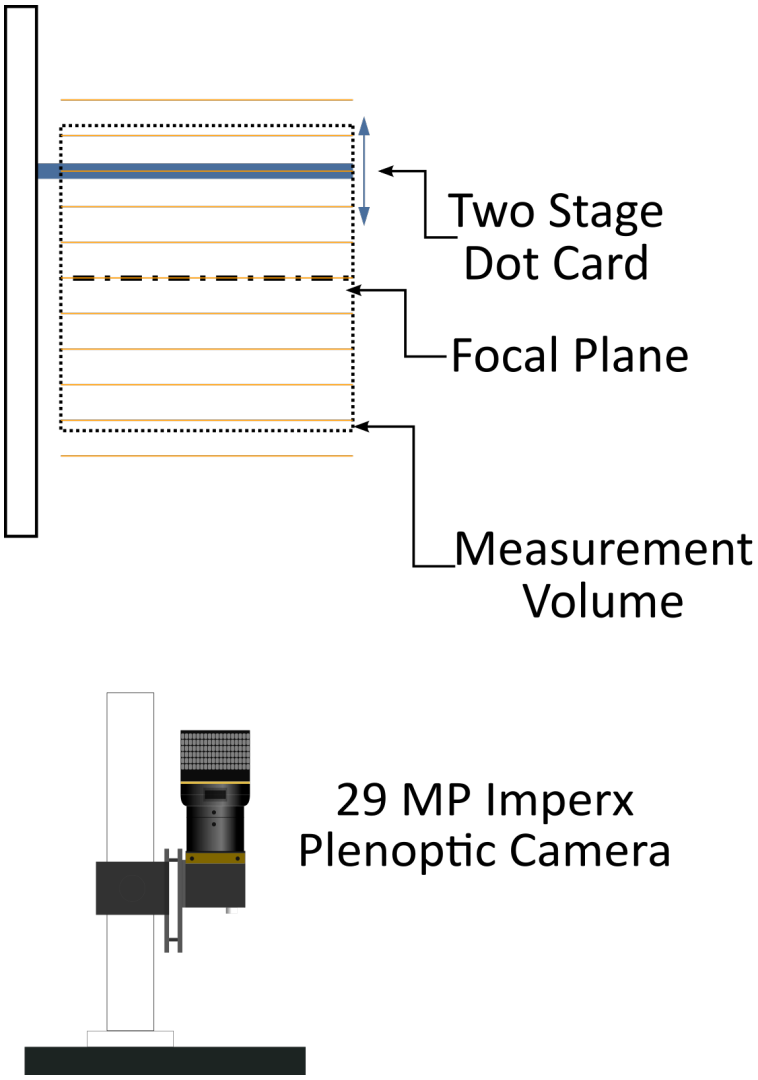

Figure 2.6: Schematic depicting the translation of the two-stage calibration target through multiple planes of the measurement volume in order to compute the direct light field calibration

To date, the most extensive application of plenoptic PIV is the work of Johnson et al. [72], who presented volumetric measurements in the wake of a hemisphere. This study was the first known publication in the field of plenoptic PIV that was not focused on the development of the measurement system.

2.4 The Proper Orthogonal Decomposition

This dissertation revolves around the findings from a relatively large data set, comprised of hundreds of images for each different combination of wing kinematics, about 60,000 images in total. While the motion of the wing has been deemed repeatable to allow phase averaging, the combination of the moving wing and highly 3D fluid motion causes difficulty when subtracting a background image. The slightest offset in the wing position in the image causes some particles to be removed or diminished in some frames, thereby reducing the fidelity of the final results. Examples of this process are shown in Section 3.2.1 Thus, the proper orthogonal decomposition (POD) was used to identify an optimized background to subtract for each image in this dataset. The POD is commonly used as an analysis tool for fluid measurements, known primarily for providing a method for extracting reduced information from large sets of data. The extracted information is synthetic in the sense that it exists only as a representation of the data set as a whole, but does not exist as an individual data sample. The POD is a robust procedure that proves useful in analyzing large data sets from assorted fields. An extensive summary of the POD is provided in Appendix C, that explains the intricate math behind POD.

Fortunately, the application of the POD is much simpler than the math behind it. A detailed explanation of how the POD has been applied for background subtraction during the data reduction process is provided in the following sections.

2.5 Preliminary Research

In the preliminary study, an earlier version of the 29 MP plenoptic camera was used. A two week long experiment allowed for the collection of preliminary data and the identification of potential improvements to the experiment for the final experiment presented in this dissertation. Smaller volumes were captured in this experiment, briefly presented in the following subsections. The images gathered in this experiment were used in the development of POD based background subtraction and the entire data reduction process presented in chapter 3.2.

2.5.1 Pure Pitch

Measurements were made at two different reduced pitch rates, K = 0.1 and 0.5, at the half-span of the wing. The volume included about 5 percent of the chord length upstream of the leading edges and extended to about 65 percent of the chord. For each value of K, 100 3D vector fields were calculated for each angle of attack $\alpha = 5, 10, 15, 20, 25$, and 30. Two ensemble averaged flow fields are displayed using a three-view format, in figures 2.7 and 2.8 at $\alpha_{\text{geo}} = 5$ and 20, respectively, for K = 0.1. The flow is visualized with isosurface contours of positive and negative z vorticity $\pm\omega_z$ (red and blue) and swirling strength criterion λ_{ci} (yellow contours).

Specifically, in figure 2.8 a large LEV is identified in a strong recirculation region. Unfortunately, it has been drawn to the attention of the researchers that the calibration of the pitching motor was performed incorrectly, and the pitching data is suspect to large errors in the angle of attack of the wing. Thus, physical implications of this data set will not be discussed and these figures will only serve as proof that the imaging system is capable of making such measurements.

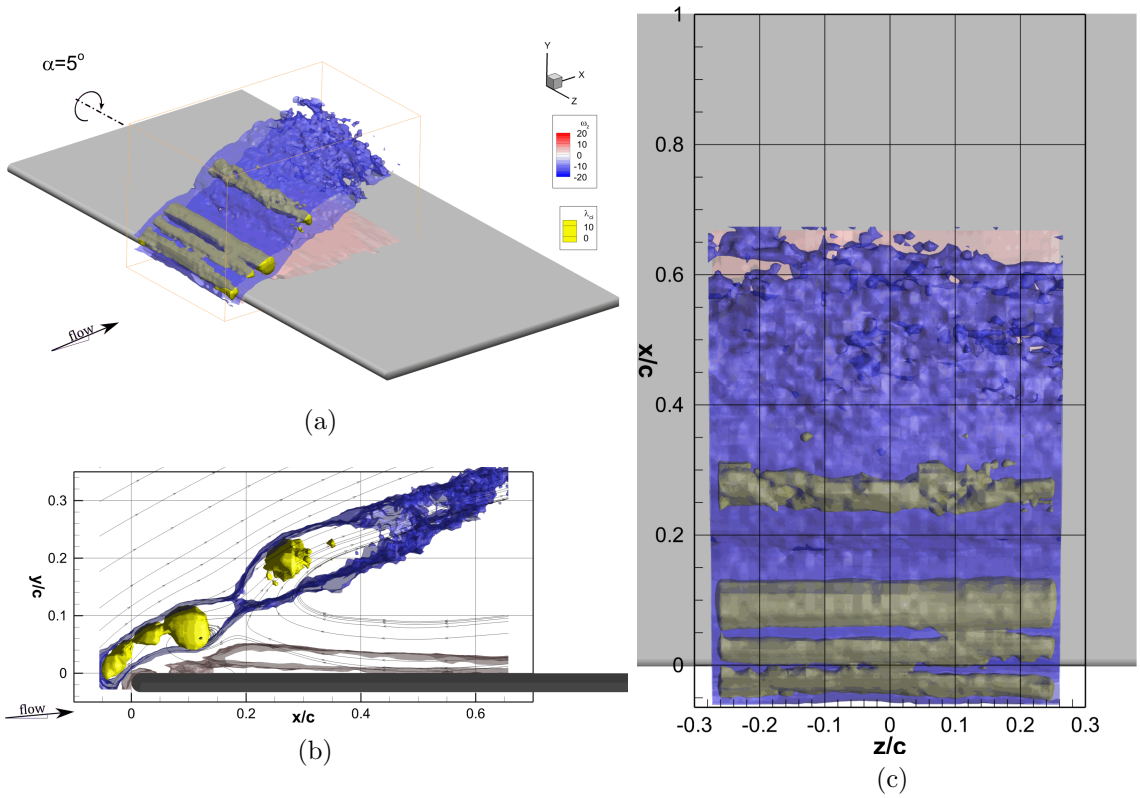

Figure 2.7: Isosurfaces of swirling strength at $\alpha_{\text{geo}} = 5$

2.5.2 Pure Roll

The results of the purely rolling wing demonstrate the development of the three dimensionality of the flow, which can be seen in the comparison of figure 2.9, 2.10, and 2.11. Isosurfaces of ω_z and swirling strength λ_{ci} are shown for ensemble averages of $\phi = 3°$, $12°$, and $25°$, respectively. Figure 2.9 shows that a prominent LEV is present at $\phi = 3°$, connected to a downstream region of $-\omega_z$ (the attached boundary layer) which trails to the end of the measurement volume. Underneath these features, a thin region of secondary vorticity blankets the plate, approximately 0.02c thick. At the inboard and outboard spanwise regions of the measurement volume, the λ_{ci} contours reveal a smaller vortex beginning to develop upstream of the prominent vortex. The relative two dimensionality of the flow structure is seen in figure 2.9c, as the LEV is nearly has nearly constant size and location across the measurement volume. Figure 2.10 shows the same views and isosurfaces for $\phi = 12°$. A third vortex is present at x/c = 0.3, which begins to lift off the surface of the plate towards

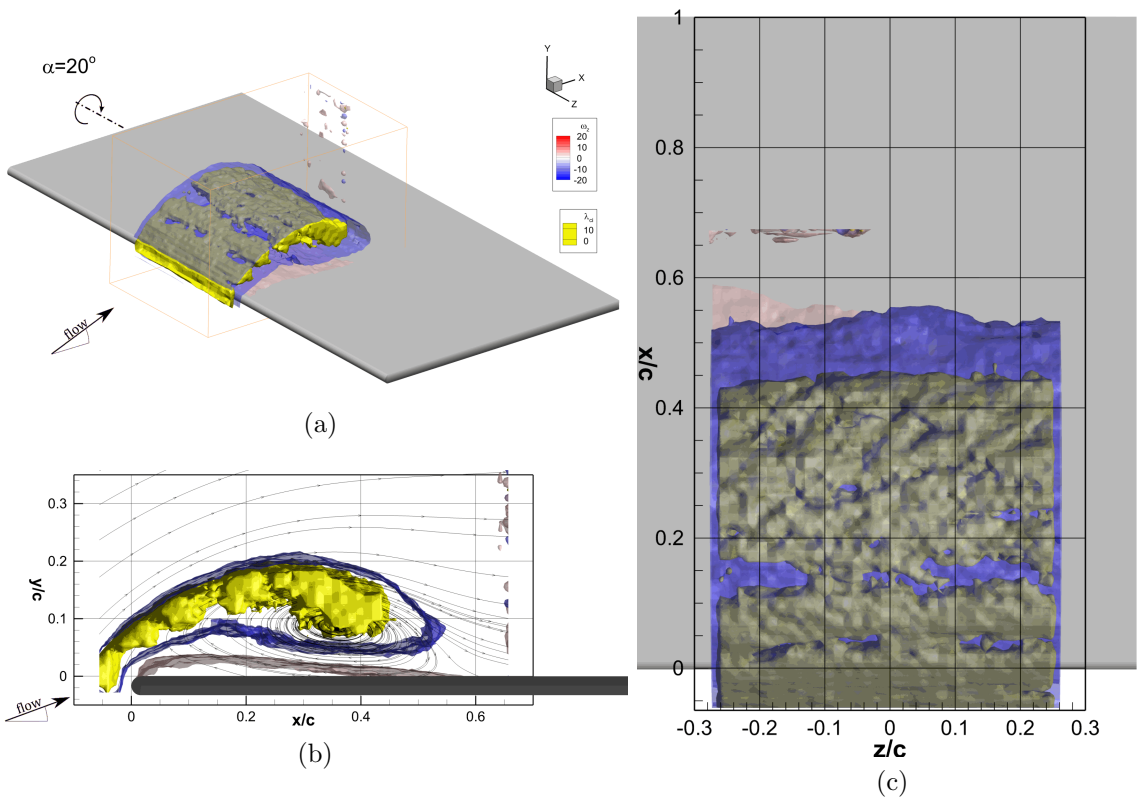

Figure 2.8: Isosurfaces of swirling strength at $\alpha_{\text{geo}} = 20$

the tip of the plate (–z). The two vortices closer to the leading edge stay relatively level across z. As the roll cycle progresses to $\phi = 20°$, figure 2.11 the two vortices nearest to the leading edge remain relatively the same in size and strength. The third vortex however, sees a decrease in strength and an even greater inclination towards the tip of the plate.

The arching structure seen in the development of the LEV is similar to what has been observed in the literature, as the LEV begins to lift off and combine with the tip vortex. The core of the LEV is not dominated by any one direction of spanwise flow. However, it does not appear that the LEV stabilizes over the range of ϕ for the given advanced coefficient and aspect ratio that the preliminary experiments have explored.

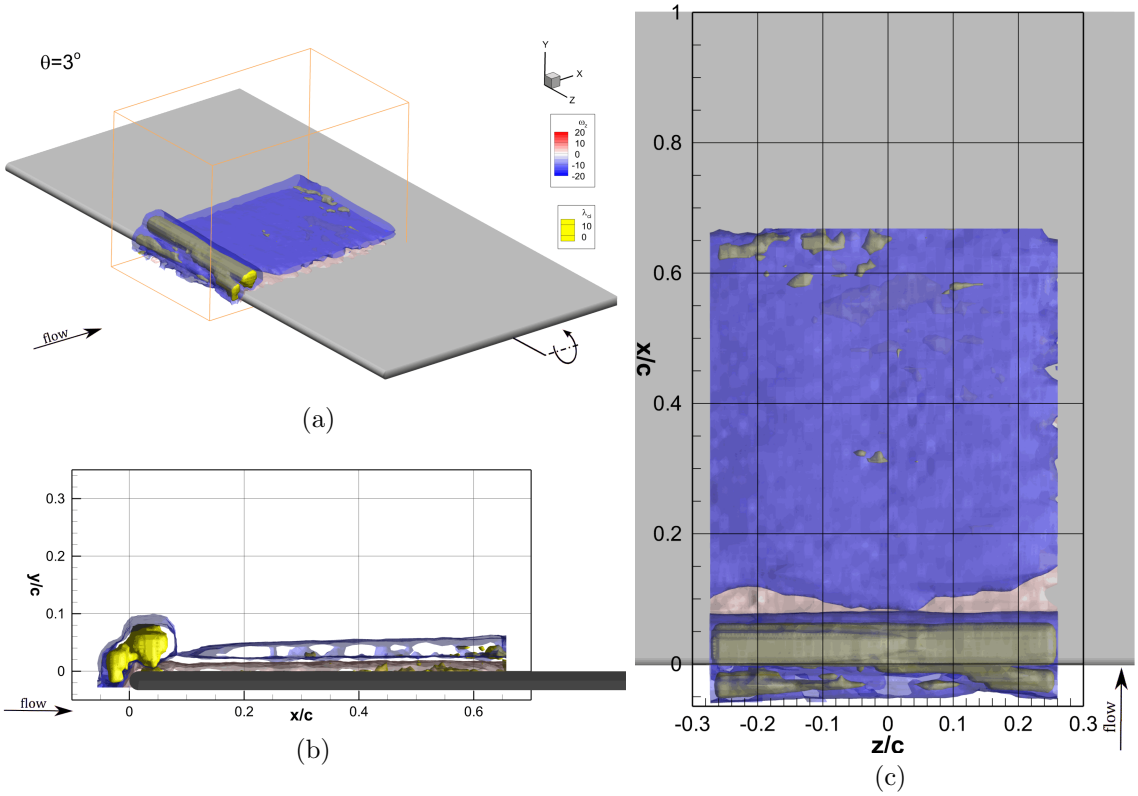

Figure 2.9: Isosurfaces of swirling strength at $\phi = 3$

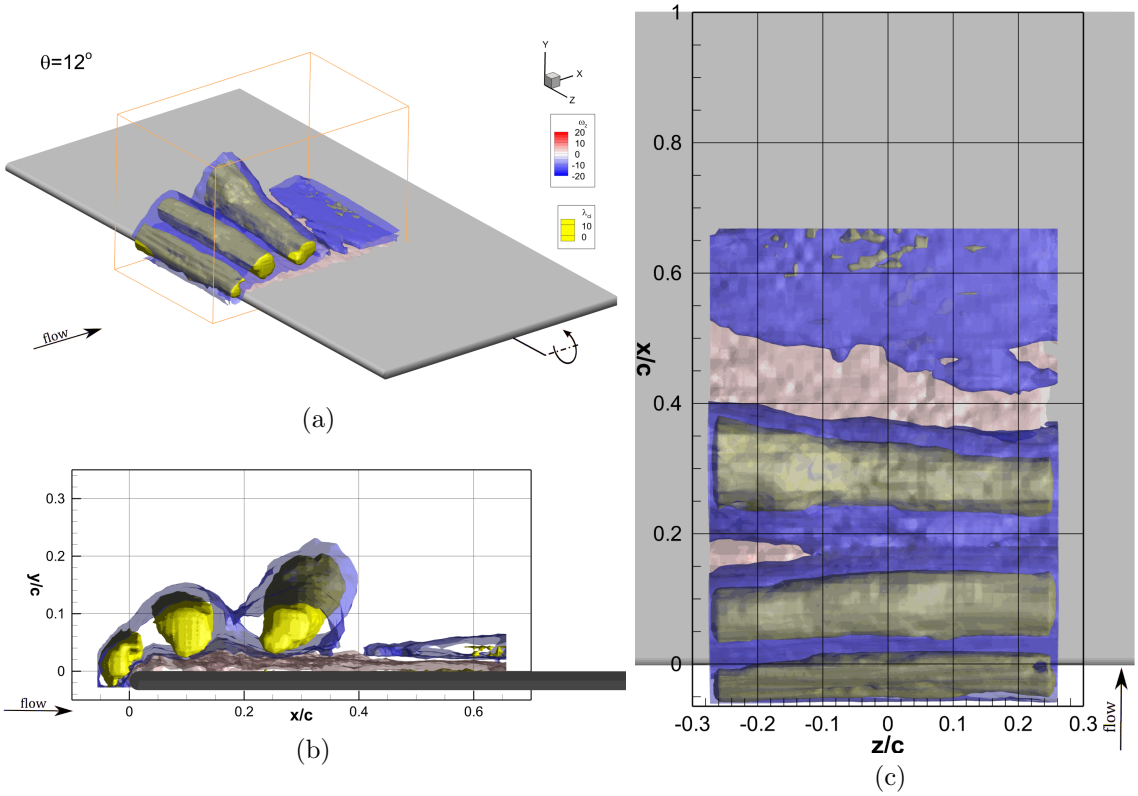

Figure 2.10: Isosurfaces of swirling strength at $\phi = 12$

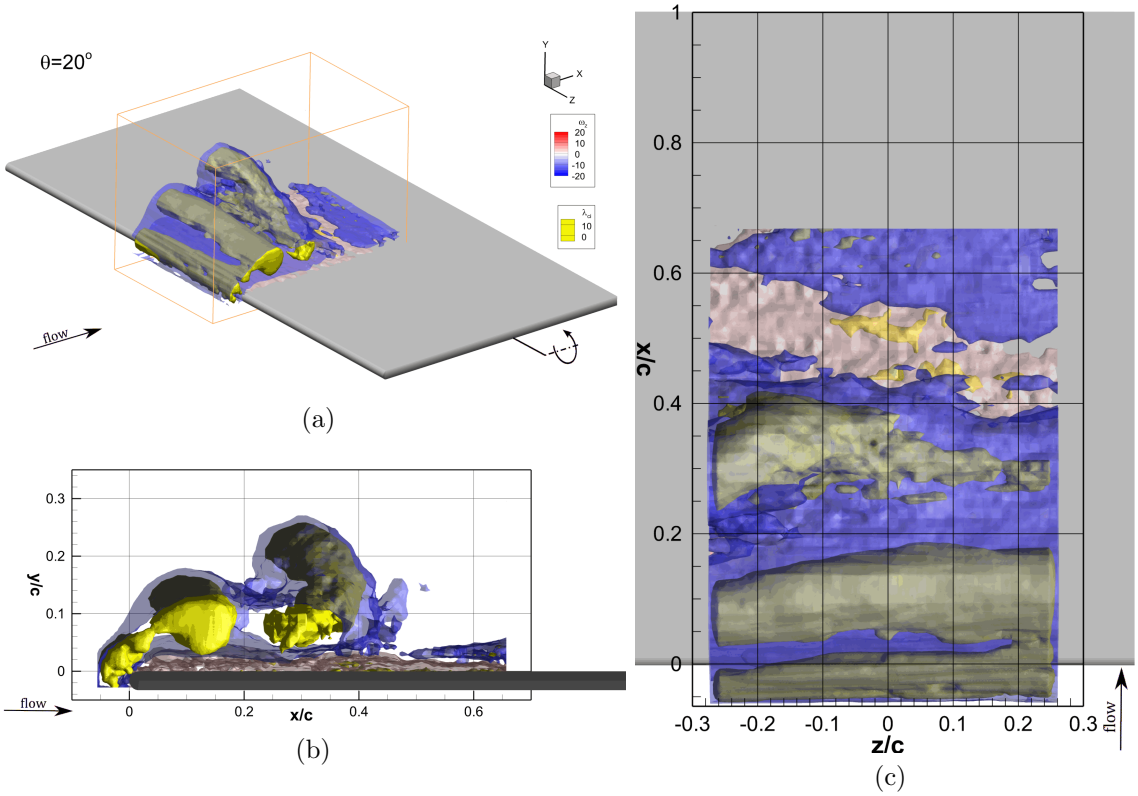

Figure 2.11: Isosurfaces of swirling strength at $\phi = 20$

Chapter 3

Methods

3.1 Experimental Procedure

A flat, acrylic plate was articulated in the presence of a freestream velocity of 124 mm s^{-1}. The flow was created in the University of Iowa's free-surface water channel with test section width of 0.61 m and water depth of 0.33 m. The water channel has flow conditioning consisting of an 8:1 contraction ratio, honeycomb, and five screens to maintain freestream turbulence intensity below 0.3 percent. The AR 2 plate had a chord length, c =76.3 mm and thickness of 3.3 percent of the chord, with both the leading and trailing edges rounded with a constant radius of half the plate thickness. The maximum blockage ratio was 3.1 percent. These parameters produced a chord-based Reynolds number of $Re_c = 10000$. The pitching motion was always about the LE of the wing and the roll axis was situated such that the radius of gyration was 3.25 times the chord length. The roll and pitch maneuvers were articulated by an Emerson XVM-8020-TONS-000 DC servo motor for roll and an Emerson XVM-8040-TONS-000 for pitch, both using a Galil DMC-4040 motion controller and Emerson EP-204B servo drive. Figure 3.1 shows an illustration of the arrangement and coupling of the pitch and roll motors. The motors were fixed to a skim plate such that the roll axis was co-planer to the skim plate. To accommodate the physical size of the motor, a cavity protruded below the lower surface of the skim plate, allowing the rotational axis of the motor to lie co-planar with the skim plate. This cavity was located 5 chord lengths downstream of the plate.

The wing motion was prescribed as a linear ramp, smoothed using the Eldredge function [73] with a smoothing parameter of 1.2. Sample wing kinematics are shown in figure 3.2. During the pure pitch maneuver, the wing is initially set to $\alpha_{geo} = 0^\circ$ and pitches to $\alpha_{geo} =$

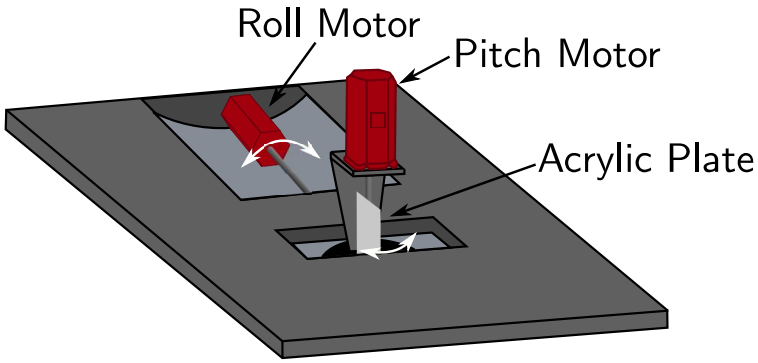

Figure 3.1: Illustration of motor layout on the skim plate

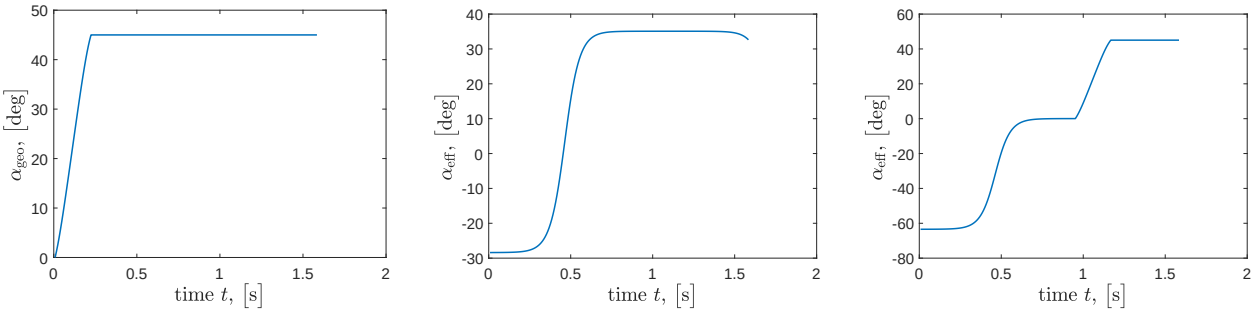

(a) (b) (c)

Figure 3.2: Wing kinematics for (a) pure pitch, (b) pure roll, and (c) simultaneous pitch & roll maneuvers

45° in about 0.5 s. At the end of the motion, the wing is static, followed by the reverse maneuver to return to $\alpha_{geo} = 0°$, where the wing remains static for about 5 s to allow the any flow perturbations caused by the wing motion to diminish. Then the motion is repeated. For the roll kinematics, the wing was initially set to a geometric angle of attack (in figure 3.2b $\alpha_{geo} = -28.4°$) and began rolling until it reached a constant roll rate, in which the induced angle of attack α_{ind} becomes constant, resulting in $\alpha_{eff} = \alpha_{geo} + \alpha_{ind} = 35°$. When the wing is pitched and rolled, shown in figure 3.2c, the pitching motion does not begin until $\alpha_{eff} = 0°$ and $\frac{d\alpha_{eff}}{dt} \approx 0°$. Thus, the wing is set to an initial $\alpha_{geo} = -\alpha_{ind}$ such that once the rolling motion is reaches a constant rate, $\alpha_{eff} = 0°$. The roll motion continues, keeping $\alpha_{eff} = 0$, for about 0.4 s, at which point the pitching motion begins. The epoch for the simultaneous pitching and rolling maneuver is defined when the pitching motion begins, here at $t = 0.88$ s. The parameter space of this study was selected particularly to examine

a dimensionless parameter, k_{Rg}, which is defined below in equation 3.1. This parameter is similar to the reduced pitch rate k, yet also accounts for the wing maneuvering in a rotating reference frame.

$$k_{Rg} = \frac{\dot{\alpha}_{\text{eff}} c}{2U_{R_g}} \tag{3.1}$$

$$U_{R_g} = \sqrt{(\dot{\phi} R_g)^2 + U_\infty^2} \tag{3.2}$$

Given the definitions of the reduced pitch rate ($k = \dot{\alpha}c/2U_\infty$) and the advance coefficient ($J = U_\infty/\dot{\Omega}R_g$), equation 3.1 simplifies to

$$k_{Rg} = \frac{k}{\sqrt{J^{-2} + 1}}. \tag{3.3}$$

Thus, it is hypothesized that the effect of adding a rolling reference frame to the vortex system created by a pitch-up maneuver can be discerned by matching k and k_{Rg}, in a comparison between pure pitch and combined pitch/roll kinematics. It is noted that for a purely pitching wing, $k = k_{Rg}$. From table 3.1 below, it is clear that the kinematics have been specifically selected to match k and k_{Rg} values. Moreover, the J values have been matched between the pure rolling and simultaneously pitching and rolling cases, to isolate the effect of adding pitch to the rolling motion.

The complete parameter space of wing kinematics is shown in table 3.1, along with a case name by which each case will be referred to hereafter. The naming convention uses a letter to refer to pitching, rolling, or simultaneously pitching and rolling, and subscripts and superscripts correspondence to the prudent rate or angle. For example, case $P_{.5}$ is a purely pitching case with a reduced pitch rate of 0.5. Similarly, $R_{.54,33}$ is a purely rolling case with an advance coefficient of 0.54, and the additional subscript is the effective angle of attack of the case $\alpha_{\text{eff}} = 33°$. The simultaneously pitching and rolling case $S_{.46,.54}^{.22}$, has subscripts indicating the values of k and J, respectively, and the superscript is the k_{Rg} value.

Case Name	$R_g/\mathbf{c}$	**Location**	J	k	k_{Rg}	α_{eff}	ϕ
$R_{.54,23}$	3.25	c	0.54			23°	12°–49°
$R_{.54,33}$	3.25	r-c-t	0.54			33°	6°–49°
$R_{.54,43}$	3.25	c-t	0.54			43°	12°–49°
$R_{1.36,33}$	3.25	c-t	1.36			33°	3°–49°
$R_{1.36,43}$	3.25	c	1.36			43°	3°–49°
$P_{.5}$	3.25	r-c-t		0.50		15°–45°	0°
$P_{.2}$	3.25	c-t		0.19		15°–45°	0°
$S^{.22}_{.46,.54}$	3.25	r-c-t	0.54	0.48	0.22	15°–45°	30°–49°
$S^{.20}_{.42,.54}$	3.25	c-t	0.54	0.45	0.20	15°–40°	31°–49°
$S^{.50}_{1.05,.54}$	3.25	c-t	0.54	1.12	0.50	15°–45°	25°–40°
$S^{.37}_{.46,1.36}$	3.25	c-t	1.36	0.50	0.37	15°–45°	24°–38°
$r_{.54,33}$	2.50	c	0.54			33°	6°–49°
$r_{1.36,33}$	2.50	c	1.36			33°	3°–50°
$s^{.37}_{.46,1.36}$	2.50	c	1.36	0.50	0.37	15°–45°	24°–38°

Table 3.1: Detailed parameter space of wing kinematics

For the cases with the smaller radii of gyration, the nomenclature uses a lowercase letter, *e.g.* $s^{.37}_{.46,1.36}$. The name for each case and the radius of gyration for that case are found in the first two columns of table 3.1, respectively. The third column uses the letters *r, c,* and *t*, to describe which measurement volumes were captured for each case, corresponding to the root, center, and tip regions, respectively. The values of k and J are given in the fourth and fifth columns, respectively. Additionally, the study defines the parameter k_{Rg} as a variation of the reduced pitch frequency that accounts for the rolling motion of the wing as well, shown in the sixth column. Here, k_{Rg} is calculated as $k_{Rg} = \dot{\alpha_{\text{eff}}}/2V_{R_g}$ where, $V_{R_g} = \sqrt{U_\infty^2 + (\dot{\phi}R_g)^2}$. The ranges of the effective angle of attack ($\alpha_{\text{eff}} = \alpha_{\text{geo}} + \alpha_{\text{ind}}$) and the roll angle ϕ are given in the seventh and eight columns, respectively.

This study employs the unique measurement capabilities of plenoptic particle image velocimetry (PIV), described in the previous chapter. In this experiment a 200 mJ dual-cavity, pulsed Nd:YAG laser illuminated a $102 \times 68 \times 68$ mm volume, which included the entire chord of the wing. The plenoptic camera was fixed on a rotational stage below the water tunnel, viewing the wing along the span from tip to root. A schematic of the arrangement is shown in figure 3.3.

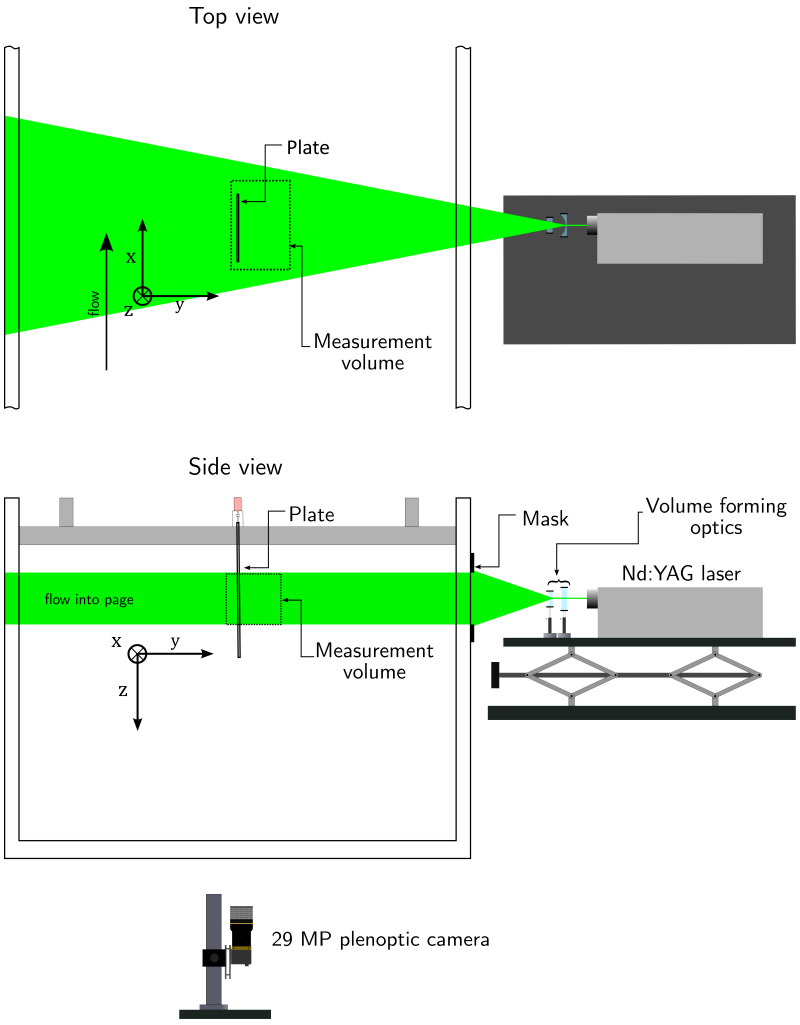

Figure 3.3: Experimental schematics: a top and side view of the experimental arrangement

Plenoptic images were recorded when the wing was vertically aligned with the plenoptic camera, which required that the initial position of the wing was preset to the negative roll angle of a given phase. For example, when images were taken at $\phi = 12°$, the initial position of the wing was set to $\phi = -12°$, so when the wing crossed the vertical plane aligned with the camera, it had rolled 12°. Additionally, the camera was rotated on the rotational stage to match the geometric angle of attack of the wing at each phase for each kinematic case, such that the wing position in each recorded image was consistent from phase to phase. Thus, the data is presented in a coordinate system fixed to the wing. This coordinate system originates on the LE of the wing, on the surface of the suction side, and at the root, shown in figure 3.4a. When $\alpha_{\text{geo}} = 0°$ and $\phi = 0°$ the wing fixed coordinate system is equal to the lab coordinate system. The lab coordinate system is shown by xyz in the orange box in 3.4b, where u, v, and w are the corresponding velocities in each direction. The freestream velocity u_∞ is in the x direction. When the wing is pitched, the wing fixed coordinate system, given bt $x'y'z'$, is equal to xyz rotated by α_{geo}, shown by the superposition of the wing in figure 3.4b. In the wing fixed coordinate system velocity is given by u', v', and w', where u' is not in the same direction as the freestream velocity u_∞.

The entire span of the wing was imaged in 3 overlapping regions, illustrated in figure 3.5. Each colored region represents a different measurement volume and the dashed line marks the focal plane of each volume, which was also the center of each volume. The imaging parameters are identical for each measurement volume, as the plenoptic camera and laser was only shifted along the z' axis. Thus, each volume has the same dimensions, extending 68 mm in the z' direction. The measurement volumes were centered at 20, 55, and 89 percent of the total span which allowed for an overlap of 14.7 mm and 16.2 mm for the root-center and center-tip interfaces, respectively.

For every kinematic case, 100 image pairs were recorded except for each $P_{.5}$, $R_{.54,33}$, and $S_{.46,.54}^{22}$ (referred herein as baseline cases) at the center volume, where 500 image pairs were recorded for determining averaging convergence and subsequent investigations. The

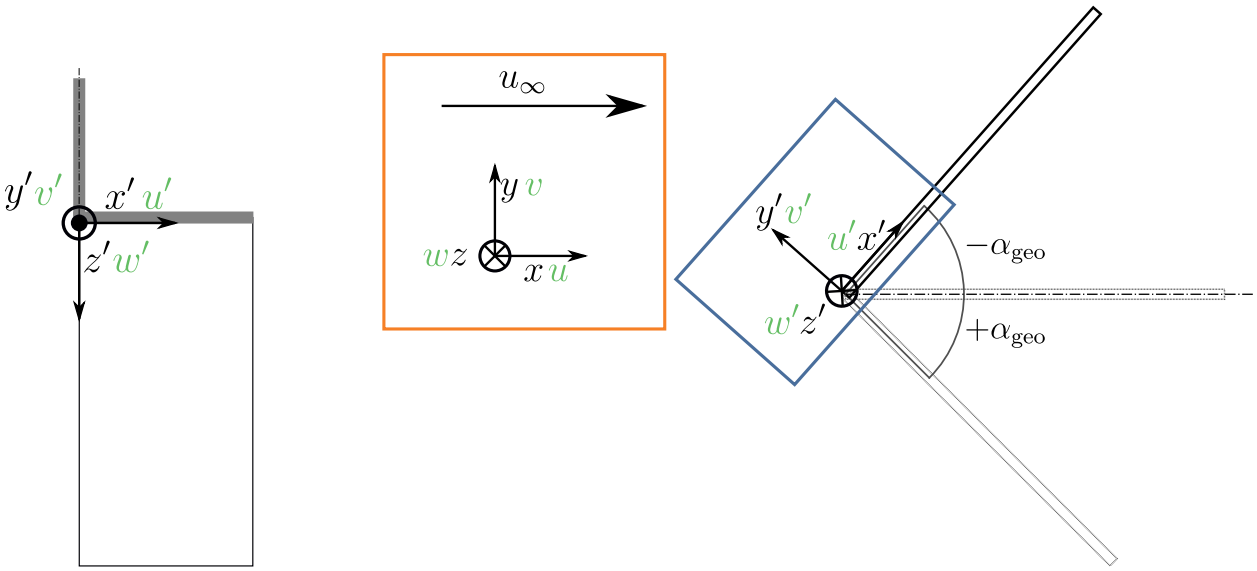

Figure 3.4: The wing fixed reference frame illustrated, (a) plan view and (b) top view, where the velocity labels are shown in green and the physical space labels in black

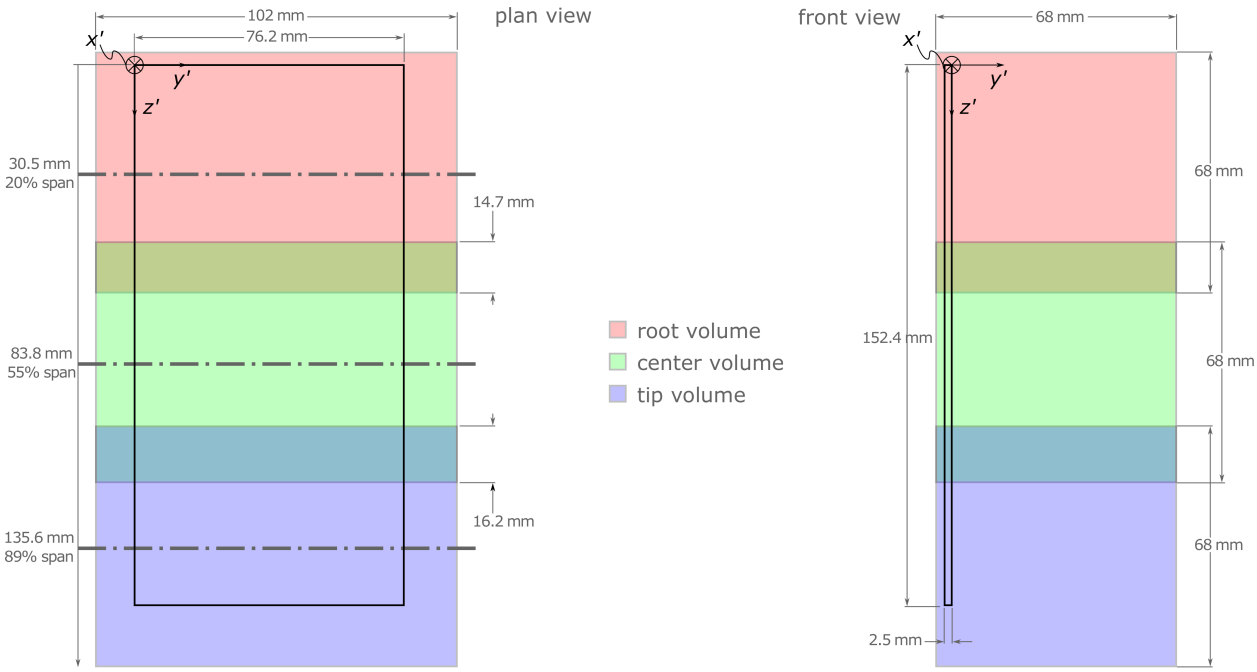

Figure 3.5: Plan and front view of the 3 different measurement volumes used during this dissertation

Parameter	Value
resolution	$4400 \times 6600\,\mathrm{px}^2$
bit depth	$14\,\mathrm{bit}$
focal length f_M	$85\,\mathrm{mm}$
f-number $f_\#$	$f_{2.96}$
extension tubes	$10\,\mathrm{mm}$
magnification M	-0.344
time between frames δt	$1.75\,\mathrm{ms}$
mean particle size	$10\,\mu\mathrm{m}$
freestream velocity	$0.124\,\mathrm{m\,s}^{-1}$
Reynolds number (chord)	$10,000$

Table 3.2: Experimental arrangement parameters

convergence of the chordwise velocity u' is calculated for a $5 \times 5 \times 5\,\mathrm{vec}^3$ region, far away from the wing surface. Using 100 image pairs, the converged value is within $1 \cdot 10^{-3}\,\mathrm{m\,s}^{-1}$ of the converged value using 500 pairs.

A summary of all of the relevant parameters regarding the experimental arrangement is provided in table 3.2.

3.2 Data Reduction

In total, 31,550 image pairs were gathered totaling 3.456 TB, which requires significant computational resources/time to process. Thus, the high performance compute cluster at Auburn University, named HOPPER, was utilized for the computational intensive steps involved in the processing routine, diagrammed in figure 3.6. After the data collection step, the next 3 operations utilized up to 20 nodes of HOPPER, with each node having 20 cores, each kinematic case taking about 4 days to process through the 3D cross correlation using 20 nodes. After the 3D Cross correlation, the ensuing processes where done on a single 12 core machine. A sample raw plenoptic image is shown in figure 3.7 illustrating the starting point of the many operations required to get to the desire results. The following sections will detail each step of the processing routine.

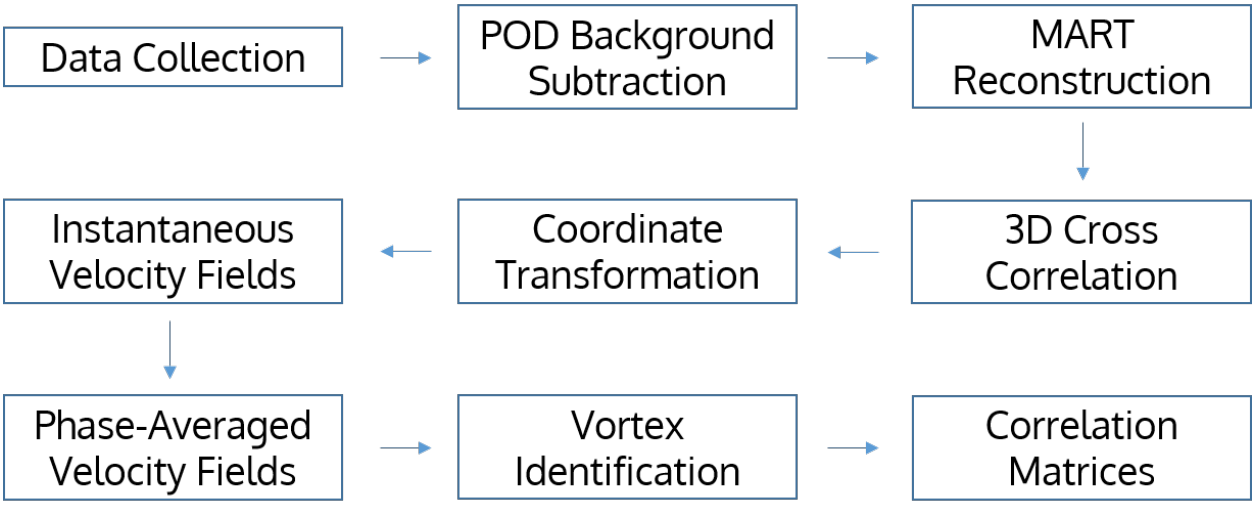

Figure 3.6: Flow Diagram of data processing routine

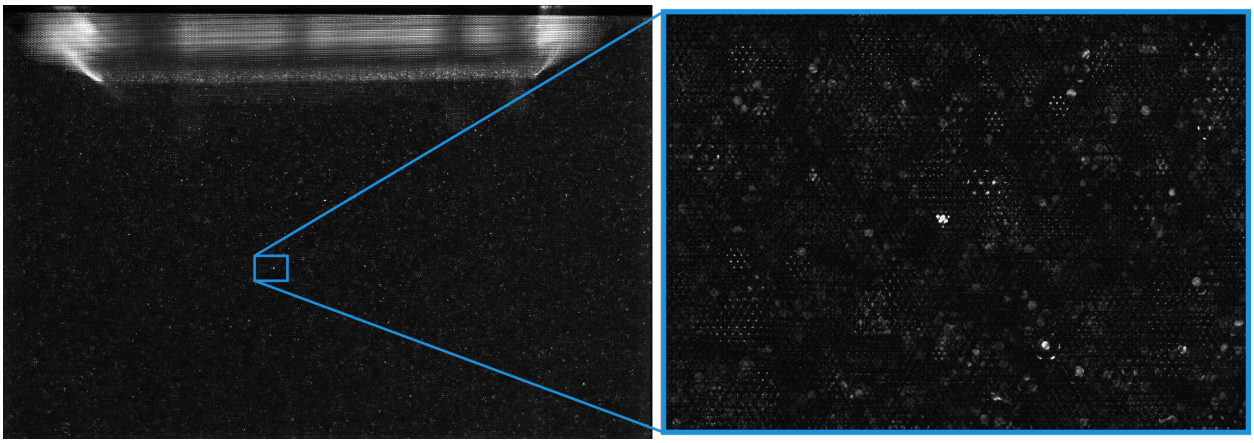

Figure 3.7: A raw plenoptic image of particle laden flow over the acrylic wing, (inset) a magnified region showing the images formed by each individual microlens

3.2.1 The POD Base Background Subtraction

While historically POD has been used as a post processing technique for particle image velocimetry results, it has only recently been applied to raw particle image, Mendez et al. [74] being the first to publish on the technique. Independently of that study, the technique has been applied to plenoptic particle images taken by the author, the process of which converged to similar criterion outlined by Mendez *et al.*. Due to the nature of the PIV algorithm, time dependent light reflections and strongly-non-uniform backgrounds can corrupt the cross-correlation results from the particle image pairs. Before discussing how the POD can be used to remove background intensities, a brief discussion of the noise of particle images is appropriate. The optimal particle images only include light that have been scattered by particles and for the remainder of this section all other light recorded on the image sensor will be referred to as noise. This includes the previously mentioned time dependent light reflections and non-uniform backgrounds. In addition to this noise, each pixels on the image sensor of the camera will randomly errors in intensity that are not present in the image, referred to as image noise. Throughout an experiment where many image pairs are gathered, the particle location in each image pair can be approximated as random. The modes from the snapshots method of POD are ranked by respective eigenvalue, which correspond to the energy in each mode. Modes with higher energy can be thought of as representing recorded light intensities that occur more frequently than modes with less energy throughout the data set of recorded image pairs. It follows that any intensities produced by a random or approximately random process would be captured in modes with very low energy and that intensities caused by any intensities caused by any process that repeats, even once, will be captured in modes with more energy. Thus, by projecting each image onto a basis of only the least energetic modes, the only intensities in each of the projected images would be from light scattered by particles.

For example, figure 3.8a shows a raw plenoptic image from $R_{54,33}$ $\phi = 26°$, where the wing is notably visible and there is a haze about the entire image. In figure 3.8b, the image

has been processed with the POD background subtraction algorithm (appendix E.1). Here, the wing has been elegantly removed and the overall haziness of the image has been removed. Additionally, several large blur spots have been removed hear the trailing edge of the wing (right side of image), which were likely reflections. This image was achieved by removing the first 23 most energetic modes. This number of modes was picked by a criterion inspired by Mendez et al. [74], where the last mode to be removed is the last mode where the difference between the consecutive, corresponding eigenvalues is less than the inverse of the number of images and the next consecutive pair also meets this criterion. See appendix E.1 line 222. This criterion is mathematically given as

$$\lambda_C - \lambda_{C+1} < N^{-1} \;\&\; \lambda_{C+1} - \lambda_{C+2} < N^{-1} \tag{3.4}$$

where N is the number of samples, and C is the index of the first eigenvalue-eigenvector pair that will not be used for the subtraction. Thus, for the previously mentioned case, $C = 24$. In figure 3.9, the normalized energy distribution for this case is shown. The x axis shows the number of eigenvalues used, reaching the first 100 eigenvalues (for this case there 1000, as there were 500 image pairs). Each eigenvalue is normalized by the sum of all of the eigenvalues, thus the sum of the normalized modal energy is 1 for all 1000 eigenvalues. At the cut-off value of 23, the relative change between the modal energies has met the criterion, with each of the corresponding modes for all modes greater than 23 have less than 0.001% of the total modal energy, which corresponds to the more random intensities throughout all 500 image pairs.

In order to prepare the data for reconstruction, this POD algorithm was implemented on every kinematic case and every phase independently, on HOPPER. The algorithm was written in C++ and utilized on 1 node but parallelized across all 20 cores, requiring about 1 hour per phase. Once all of the images have been optimized through this algorithm, particle volumes could be reconstructed from them.

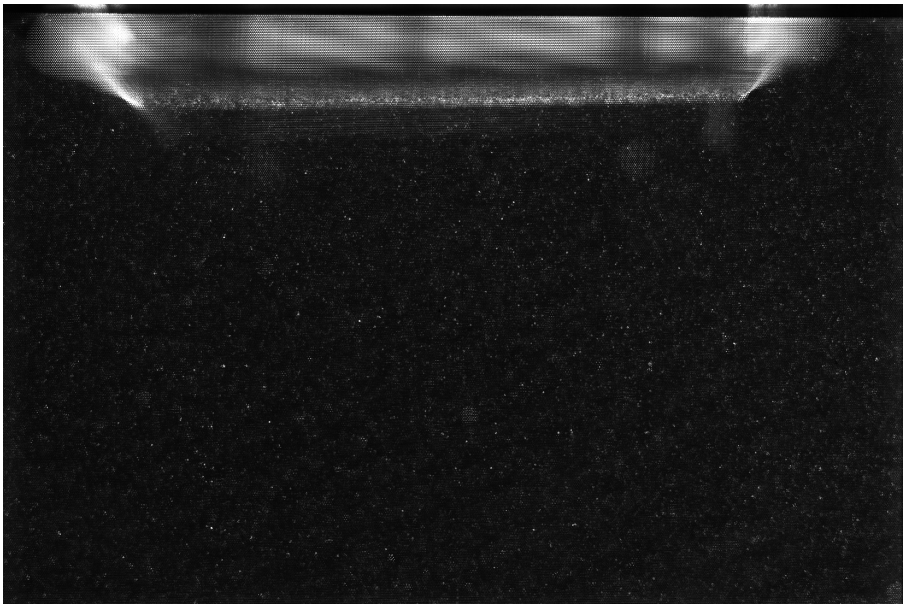

(a)

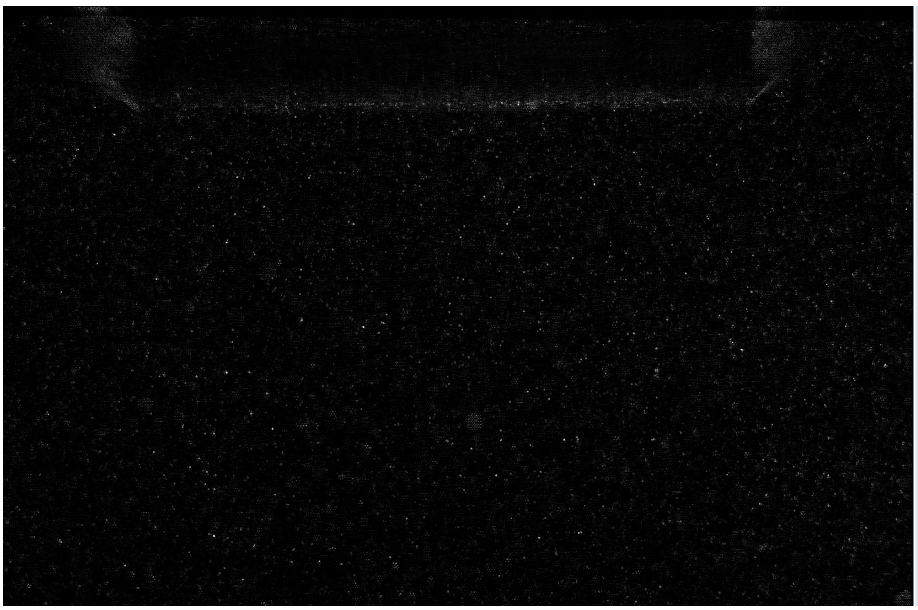

(b)

Figure 3.8: The first plenoptic particle image of $R_{.54,33}$ $\phi = 26°$ before (a) and after (b) POD background subtraction

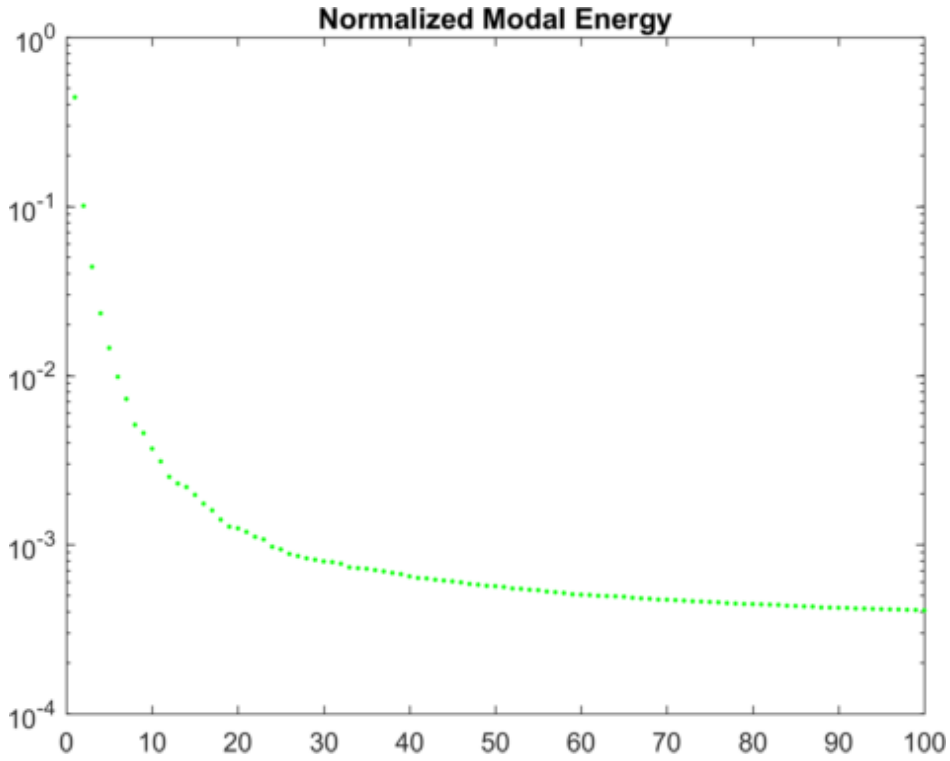

Figure 3.9: Normalized modal energy distribution for $R_{.54,33}$ $\phi = 26°$

3.2.2 MART Reconstruction

Using the previously described MART algorithm, the plenoptic images were reconstructed into volumes. This was done using an in-house software suite aptly named Dragon, originally developed by Fahringer et al. [66]. There are two control parameters, or knobs, to tune for using the MART algorithm: the relation parameter and number of iterations. To properly select the parameters, a sweep of each was conducted, while trying to satisfy continuity for the field and maximize the normalized intensity variance σ_E^* as defined by Lynch [75], given as

$$\sigma_E^* = \frac{\sqrt{\frac{1}{N}\sum_{j=1}^{N}(E_j - \bar{E})^2}}{\bar{E}} \tag{3.5}$$

where $\bar{E}$ is a scalar representing the average intensity of all voxels, N is the number of samples, and E is the 3D intensity field. A high value of the normalized intensity variance

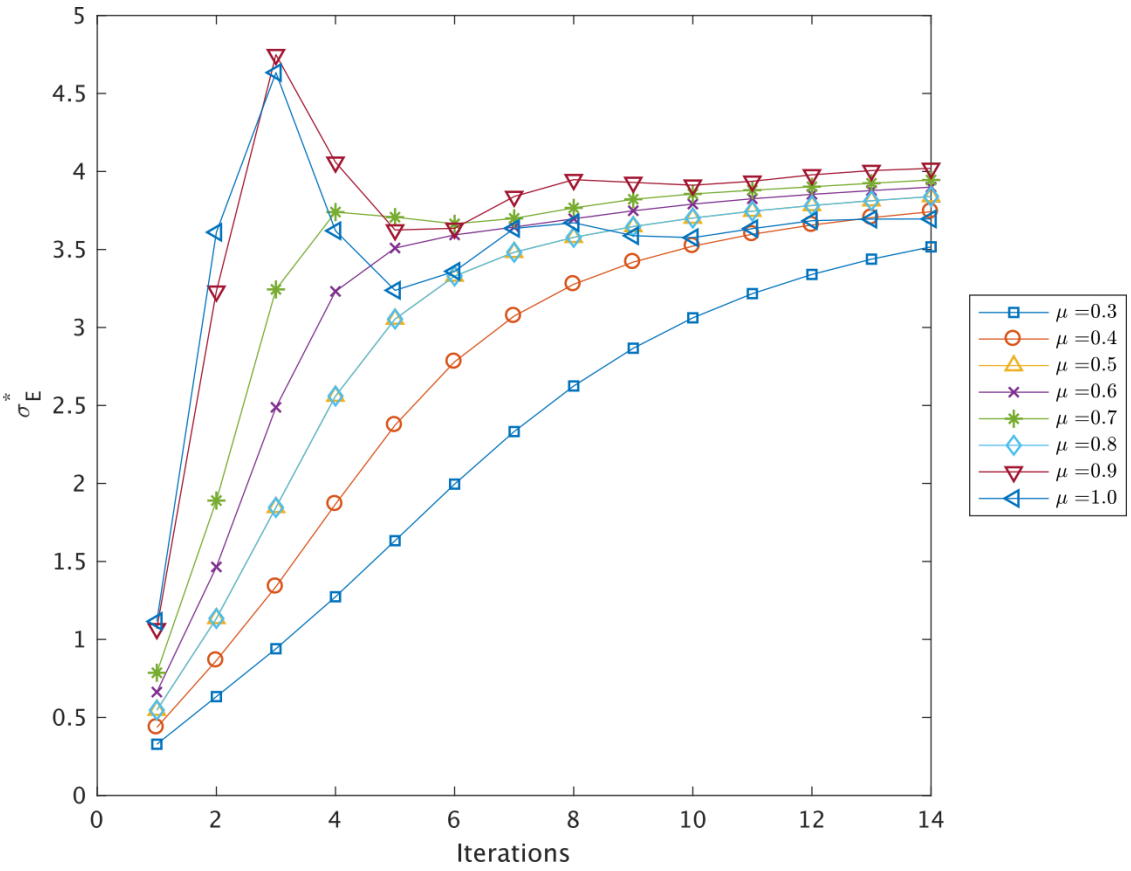

Figure 3.10: Normalized intensity variance for parameter sweep of iterations (x axis) and μ (legend)

indicates a sparse reconstructed field with high amplitude peaks, which is desirable for particle volumes suitable for PIV. Values of σ_E^* are shown below in figure 3.10, from which the 3 iterations and a relaxation parameter $\mu = 0.9$ having the greatest value. However, for the same number of iterations, $\mu = 1.0$ had a slightly lower mean value for ∇u, and a negligible decrease in σ_E^*, thus the final selection was $\mu = 1.0$ and 3 iterations. Fortunately, the resulting 3 iterations save ample computational time, however, this step is by far the most computational expensive, requiring significant use of HOPPER's resources. The resulting volumes were $527 \times 357 \times 357\,\mathrm{vx}^3$, where each voxel is a cube of 0.19 mm side length.

3.2.3 Volumetric Cross Correlation

The volume pairs were then correlated using an in-house 3D cross-correlation algorithm which consisted of 5 passes utilizing cubic windows of 64, 48, 32, 16, and 16 voxel sides for each pass, respectively. The algorithm is based on the VODIM [76], further detailed by Fahringer et al. [66]. Each pass had a window overlap of 50%, resulting in a final vector field of $63 \times 42 \times 42\,\mathrm{vec}^3$ physically spaced by 1.5 mm. This was also compute on HOPPER.

3.2.4 LE Alignment and Coordinate Transformation

From earlier testing, it was found that the physical location of the LE during the roll cycle that was captured by the camera could fluctuate by as much at 0.5° within a single phase. The design of the flapping mechanism was improved, and this variance is now estimated to be within ±0.15°. As a result, the same coordinate transformation was applied to each vector field in a given phase of a single kinematic case. The leading edge and trailing edge were visually selected from a raw plenoptic image in each sample, which were then related to corresponding points in the reconstructed volumes. This visual selection process is shown in figure 3.11. Each vector volume was then interpolated onto an identical coordinate system $x', y'z'$, which also requires that the induced velocity of the wing be subtracted from the data. The MATLAB scripts to preform all of the operations are included in appendix E.2. During this operation, the voxels and voxel displacements are converted to m and $\mathrm{m\,s^{-1}}$, respectively. Now that the entirety of each phase is sampled onto the same axes, with (0,0,0) uniformly corresponding to the LE, suction side, and root of the wing, the phase-averaged velocity fields can be simply calculated.

3.2.5 Vortex Identification

Vortices have been a primary interest of fluid dynamicists studying turbulence since the early days of flow visualization. Turbulence and vortex dynamics are deeply intertwined, to the extent that turbulence is often viewed as a tangle of vortex filaments. Thus, a better

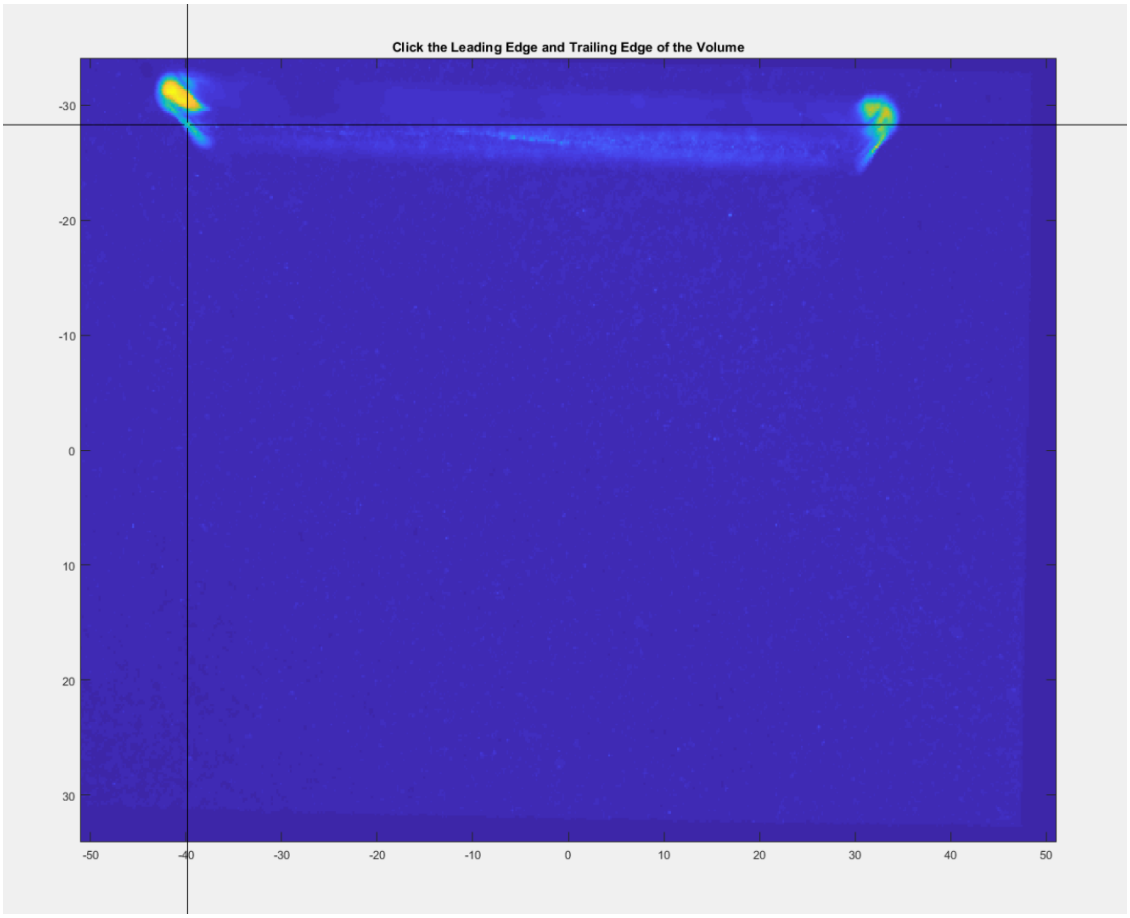

Figure 3.11: MATLAB figure window for visually selecting the LE and TE

understanding of vortex dynamics promises not only to better define turbulent phenomena such as entrainment and mixing, heat and mass transfer, chemical reaction and combustion, drag, and aerodynamic noise generation, but also improvements in turbulence modeling. Scientists and researchers continue to study both vortex dynamics and turbulence using experimental and computational methods, but are hindered by the difficulty in identifying a vortex in a flow, largely because of the vague definition of a vortex. However, there exist a variety of identification methods, most of which depend on the velocity gradient tensor,

$$\nabla \mathsf{u} = \begin{bmatrix} \frac{\partial u}{\partial x} & \frac{\partial u}{\partial y} & \frac{\partial u}{\partial z} \\ \frac{\partial v}{\partial x} & \frac{\partial v}{\partial y} & \frac{\partial v}{\partial z} \\ \frac{\partial w}{\partial x} & \frac{\partial w}{\partial y} & \frac{\partial w}{\partial z} \end{bmatrix} = \mathsf{S} + \Omega \tag{3.6}$$

This equation can be recast as an eigenvalue-eigenvector problem as

$$\nabla \mathsf{u} = \mathsf{e}\lambda\mathsf{e}^{-1} \tag{3.7}$$

where,

$$\mathsf{e} = [\mathsf{v}_{\mathrm{r}}\mathsf{v}_{\mathrm{cr}}\mathsf{v}_{\mathrm{ci}}] \tag{3.8}$$

and

$$\lambda = \begin{bmatrix} \lambda_{\mathrm{r}} & 0 & 0 \\ 0 & \lambda_{\mathrm{cr}} & \lambda_{\mathrm{ci}} \\ 0 & -\lambda_{\mathrm{ci}} & \lambda_{\mathrm{cr}} \end{bmatrix}. \tag{3.9}$$

In a study of the physical mechanisms of generating hairpin vortices, Zhou et al. [1] developed a new technique for identifying and visualizing vortices, similar to the Δ-Criterion. The study uses the imaginary part of the complex eigenvalue of $\nabla \mathsf{u}$. Combining equations 3.7 and 3.9

yields

$$\nabla \mathsf{u} = [\mathsf{v}_\mathrm{r}\mathsf{v}_\mathrm{cr}\mathsf{v}_\mathrm{ci}] \begin{bmatrix} \lambda_\mathrm{r} & 0 & 0 \\ 0 & \lambda_\mathrm{cr} & \lambda_\mathrm{ci} \\ 0 & -\lambda_\mathrm{ci} & \lambda_\mathrm{cr} \end{bmatrix} [\mathsf{v}_\mathrm{r}\mathsf{v}_\mathrm{cr}\mathsf{v}_\mathrm{ci}]^{-1} \tag{3.10}$$

where the subscript r represents the real components, and subscripts cr and ci represent the complex real and complex imaginary components, respectively. The instantaneous streamlines can be locally defined by a curvilinear coordinate (y_1, y_2, y_3) system. The axes of the coordinate system are defined by the eigenvectors $\mathsf{v}_\mathsf{r}\mathsf{v}_\mathsf{cr}\mathsf{v}_\mathsf{ci}$, described by Equations (3.11a–3.11c). This coordinate system is shown in Figure (3.12).

$$y_1(t) = C_r \exp\Big(\lambda_r t\Big) \tag{3.11a}$$

$$y_2(t) = \exp\Big(\lambda_{cr} t\big[C_c^{(1)} \cos(\lambda_{ci} t) + C_c^{(2)} \sin(\lambda_{ci} t)\big]\Big) \tag{3.11b}$$

$$y_2(t) = \exp\Big(\lambda_{cr} t\big[C_c^{(1)} \cos(\lambda_{ci} t) - C_c^{(2)} \sin(\lambda_{ci} t)\big]\Big) \tag{3.11c}$$

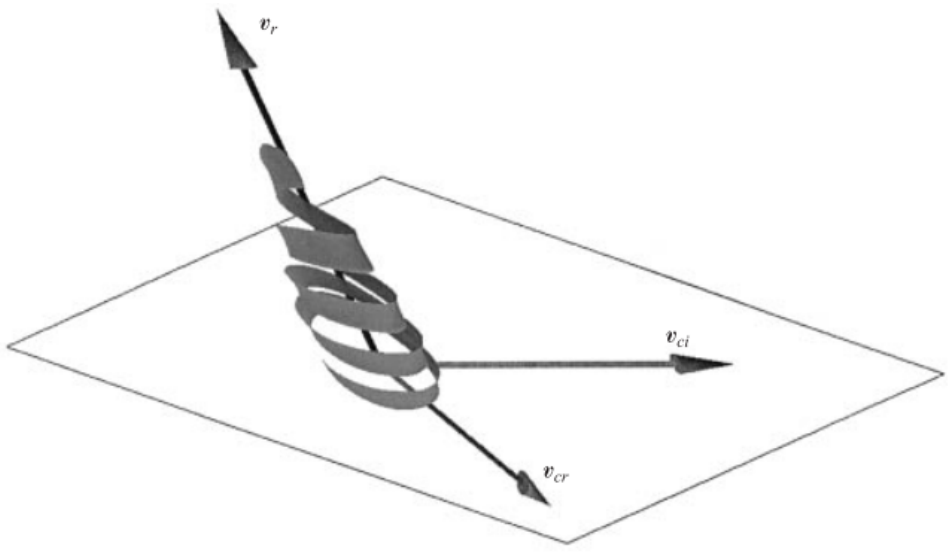

Figure 3.12: The local streamline pattern with the eigenvectors of the velocity gradient tensor in the neighborhood of a vortex core [1]

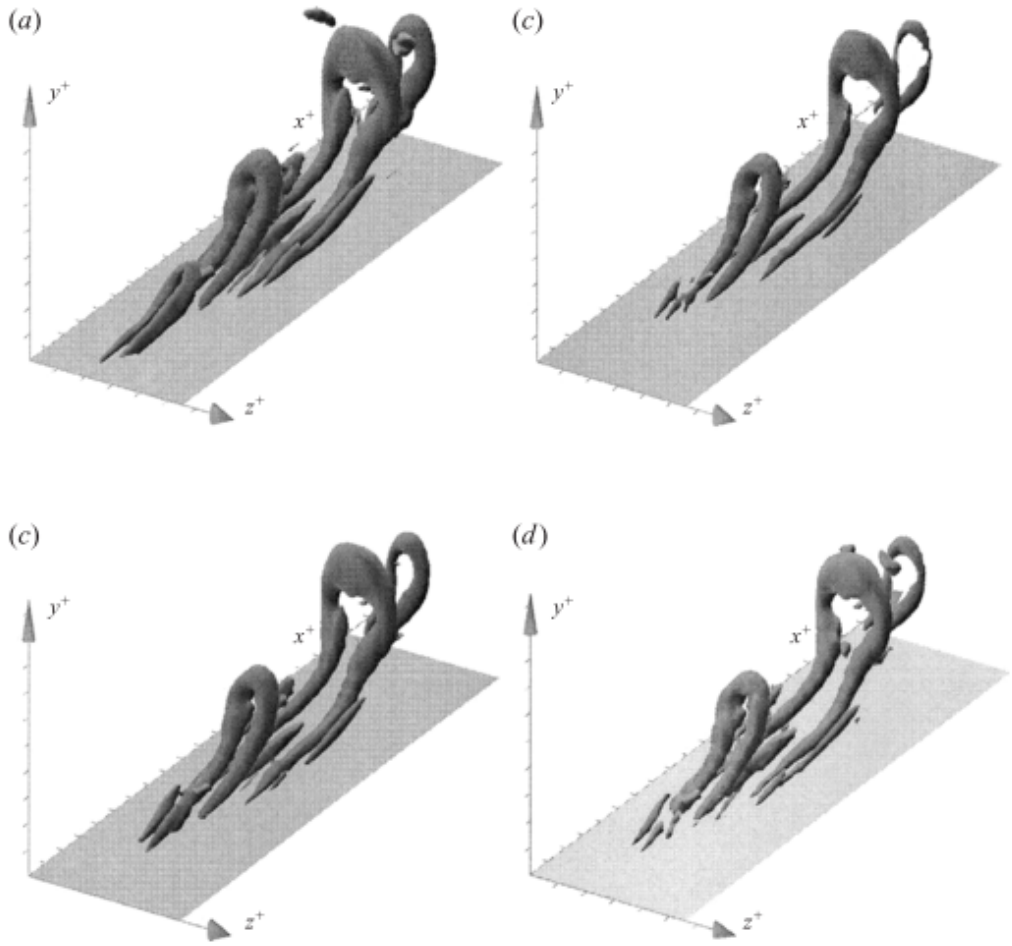

Figure 3.13: Vortical structures identified by an iso-surface of (a) λ_{ci}^2 with 1.4% maximum; (b) λ_{ci}^2 with 2.8% of maximum; (c) λ_{ci}^2 with 4.2% of maximum; (d) $\lambda_2 = -10$ (from Zhou et al. [1])

From an inspection of both Figure (3.12) and Equations (3.11a–3.11c) it follows that the flow is stretched along the $\mathsf{v_r}$, while the flow swirls in the plan spanned by $\mathsf{v_{cr}}$ and $\mathsf{v_{ci}}$. Furthermore, λ_{ci} quantifies the strength of the local swirling motion. Thus, λ_{ci} or "Swirling Strength" Criterion is theoretically satisfied when $\lambda_{ci} > 0$, indicating that the streamlines have a swirling component. In practice, better results are achieved when the criteria for a vortex is defined to be $\lambda_{ci} \geqslant \epsilon > 0$, where ϵ is a small number [77]. Zhou *et al.* prefer to use $\lambda_{ci}^2 \geqslant \epsilon > 0$ and set ϵ anywhere between 1% to 10% of the maximum λ_{ci} value. A comparison from Zhou *et al.* of the λ_{ci} at different thresholds of ϵ and similar D of simulated hairpin vortices is shown in Figure (3.13).

3.2.6 Time Constant

Because of the variation between cases involving multiple parameters, a universal normalization method is used. As such, a time constant, τ is defined as

$$\tau = \frac{c}{V_{\text{rel}}} \tag{3.12}$$

where V_{rel} is the relative motion of the fluid, defined as the magnitude of the freestream velocity and whatever rotational velocities are present (from rolling or pitching). This can be thought of as the convective time, or the time it takes for fluid to be convected across the entire chord. The elapsed time is then nondimensionalized by τ resulting in a dimensionless time value, defined as $t' = t/\tau$, where t is the elapsed time since epoch for each phase. For both the pure roll and pure pitch kinematic cases, epoch is defined as the start of wing motion and for the simultaneously pitching and rolling case, epoch is defined as the start of the pitch motion, as described in chapter 3.1.

3.3 Visualization of Results

Throughout the remainder of the dissertation, both the embedded figures and online supplementary Movies (Appendix A) utilize the same visualization of the 3D-3C data, which is described here. For each case, phase-averaged results are visualized using isocontours of normalized swirling strength ($\frac{\lambda_{ci}^2}{\max\lambda_{ci}^2}$) and stream ribbons of chordwise velocity normalized by the freestream velocity ($U'/U\infty$). The isocontours are set by two levels: 10% and 15% of the maximum value in each volume, following the guidelines given by Zhou et al. [1]. Stream ribbons were calculated using a two-step Runge-Kutta method with a step size of 0.25 times the vector spacing. The stream ribbons are seeded in 3 rakes of 20 streamlines spanning from root to tip of the wing, all within the range of 6–10 mm from the leading edge and 6–12 mm off of the wing surface, and propagated in both directions. These rakes were designed to best seed the vortices produced at the leading edge. While the movies show a

single phase-averaged result per frame, the included figures show the entire phase for each case in a vertical stack. A "timeline" runs vertically down the left side of the figure, with a point labeled by the non-dimensional time (t') and the most relevant angle (α_{geo}, α_{eff}, ϕ). Both the time and the angle are increasing from top to bottom. Note that the spacing between phases on the timeline is not explicitly representative of the spacing between phases in non-dimensional time.

Both the topology and evolution of the LEVs for each case are documented in this section. To do so, it is useful to define some general terminology. The evolution of the LEV will be broken down into the following stages:

Formation and growth: a nascent vortex forms and grows into a defined, attached LEV

Transitional: the LEV is neither *clearly* attached to the leading edge, nor *clearly* detached from the leading edge, but at some intermediate stage

Detached: the LEV has *clearly* detached from the leading edge

The identification is conducted visually not only with the provided images and movies, but also from thorough examination of each volume in a 3D volume plotting software.

While visual inspection of the vortex topology has provided significant conclusions, the methodology is subjective and biased on who is examining the structures. Thus, a objective, quantitative method of comparing the vortex topology between various kinematics was desired. The result is a correlation based approach, where scalar volumes of the swirling strength criterion are correlated together. A correlation matrix, C, of the entire parameter space was created, such that each element is the scalar product of two phase-averaged swirling strength criterion fields. In other words, if $\lambda_a(x', y', z')$ represents the 3D scalar field of swirling strength for a generalized phase of a kinematic case and $\lambda_b(x', y'z')$ represents a phase of a second kinematic case, the entry in the correlation matrix defined as $\mathsf{C}_{a,b} = \vec{\lambda}_a \cdot \vec{\lambda}_b$, where $\vec{\lambda}_a$ is the vectorized form of λ_a. However, to address the varying sizes of the volumes (*e.g.* $R_{.54,33}$ measured with 3 volumes and $R_{.54,23}$ with only 1), only the overlapping measurement

domain was correlated between each case. Each value of the correlation matrix is then normalized such that

$$\mathsf{C}_{a,b} = \frac{\mathsf{C}_{a,b}}{\sqrt{\mathsf{C}_{a,a}\mathsf{C}_{b,b}}}. \tag{3.13}$$

When $a = b$, the result is 1. Thus, each value is a metric of the similarity of the vortex structure between any two phases in the parameter space, where the similarity is a measure of the rotational energy that overlaps in physical space. Herein, this metric will be denoted r, the correlation strength.

3.4 Helical Density

Another avenue for examining and predicting vortex behavior is the helical density of the LEVs. Moffatt and Tsinober [78] describe the importance of helical density at a fundamental level in relation to flow kinematics because it admits topological interpretation in relation to the linkage or linkages of vortex lines of the flow, specifically citing the leading-edge vortex as a prime example of a helical structure, in this case a vortex having a non-zero axial component of velocity. Wolfinger and Rockwell [35] are among the few to have quantified the helical density value, calculated as $H = \mathbf{v} \cdot \omega$, for the LEV of a rolling wing. The authors found that structures that exhibited alternating signs of helical density rapidly degenerated. A vortex exhibiting a singular sign of helical density is helical in nature, thus, the findings of Wolfinger and Rockwell [35] suggest that a more helical LEV exists longer than an LEV without a helical component.

3.5 Uncertainty Analysis

The estimation of the error begins with a comparison of the error reported by Fahringer et al. [66] and Hall et al. [68]. Fahringer *et al.*used a older, prototype version of the plenoptic camera which was 16 MP and used a rectangularly packed microlens array. Using these parameters, it is reported that MART has the potential to resolve synthetic particle locations

better than 1 vx in the two lateral directions and 3 vx in the depth direction. Particle displacements were then calculated to be accurate to within 0.2 vx and 1.0 vx for the lateral and depth directions, respectively. This dissertation used a similar reconstruction process and the identical correlation algorithm, however, the imaging parameters and the calibration procedure was identical to the work of Hall *et al.*. Using a 3D light-field calibration, Hall *et al.*report that particles can be located accurate to within 0.1% of the volume size for the lateral directions and 1% for the depth direction. The caveat here is that Hall *et al.*did not use MART and instead used a particle locating algorithm more suitable for sparse fields. Thus, neither of these studies provide a viable means for estimating the error in this experiment.

To aid in quantification of measurement uncertainty of this particular application of plenoptic PIV, 1000 image pairs of freestream flow were gathered with the identical experimental arrangement and imaging parameters, with the wing removed. Using the same processing techniques, the vector fields were created and averaged. The standard deviation of each velocity component was calculated at every point in the volume, allowing for the uncertainty to be quantified spatially. The velocity components in the greater extent of the volume have uncertainty of $\sigma_{u'} = 0.004$, $\sigma_{v'} = 0.003$, and $\sigma_{w'} = 0.01$ m s^{-1}. The most notable variation in along the z' axis, where the standard deviation increases for each velocity component near the edges of the volume to $\sigma_{u'} = 0.007$, $\sigma_{v'} = 0.006$, and $\sigma_{w'} = 0.015$ m s^{-1}. This is the region where phase-averaged results at each measurement volume on the wing have been stitched together, which can lead to slight misalignment and non-continuous structures. The primary method of presenting results in the next section is through use of isocontours of λ_{ci}, in which the stitched together regions are clearly visible. The use of isocontours draws attention to these minor differences, however, the analysis investigated the results using many different variables and plotting techniques, yet isocontours of swirling strength remain the most convenient and useful to describe the vortex topology.

This uncertainty can then be propagated as the systematic uncertainty into the ensuing measurements. Thus, when investigating the phase averages of 100 instantaneous images,

the error in velocity will decrease with the inverse of the square root of number of samples,

$$\bar{\sigma} = \frac{\sigma}{\sqrt{N}}. \tag{3.14}$$

In the phase-averaged field, the error is $\bar{\sigma_u} = 0.0004$, $\bar{\sigma_v} = 0.0003$, and $\bar{\sigma_w} = 0.001\ \mathrm{m\,s^{-1}}$. To estimate the velocity gradient tensor, the basis of which vorticity and swirling strength are calculated, a central differencing scheme was employed. Adrian and Westerweel [79], provide a thorough discussion the error of various methods of calculating the derivatives of velocity, indicating that the two sources of error, the noise error ϵ and truncation error τ, are given by equation 3.15 and 3.16, respectively.

$$\epsilon = 0.71\frac{\sigma_u}{\delta x} \tag{3.15}$$

$$\tau = \frac{\delta x^2}{3!}\frac{\partial^3 u}{\partial x^3} \tag{3.16}$$

However, the velocity data is first smoothed by a low-pass filter, which reported by Adrian & Westerweel, reduced the noise error by $\frac{1}{3}$, resulting in $\epsilon_x = 0.032$, $\epsilon_y = 0.024$, and $\epsilon_z = 0.079\ \mathrm{s^{-1}}$. The truncation error is given in table 3.3, which summarizes all of the relative parameters to the accuracy of this work, but is not carried through the rest of the present uncertainty analysis.

Continuing this error propagation through the eigen-decomposition of the velocity gradient tensor that is used to determine the swirling strength is not straight forward, as the algorithm that MATLAB uses for eigen-decomposition is proprietary. Thus, the error is estimated by using a Monte Carlo approach for a sensitivity analysis. The approach is simple and the short script is included in appendix E.4. Essentially, a synthetic velocity gradient tensor is created, where each value is randomly selected between ± 4, which are the greater bounds of values in the velocity gradient tensor, by visual inspection. The eigenvalue decomposition of this value is treated as a the truth measurement. A second matrix is created by adding the a random percentage of $\pm\epsilon$ to the synthetic velocity gradient tensor.

Parameter	**Value**
physical dimensions	$102 \times 68 \times 68\,\mathrm{mm}^3$
voxel discretization	$527 \times 527 \times 527\,\mathrm{vx}^3$
error in particle location	$0.102 \times 0.068 \times 0.68\,\mathrm{mm}^3$ [68]
PIV window size	64, 48, 32, 16, 16 vx
PIV window overlap	34, 24, 16, 8, 8 vx
vector discretization	$64 \times 42 \times 42\,\mathrm{vec}^3$
final correlation volume	$3 \times 3 \times 3\,\mathrm{mm}^3$
vector spacing $\delta x, \delta y, \delta z$	$1.5 \times 1.5 \times 1.5\,\mathrm{mm}^3$
number of samples, N	100
vector error, synthetic, $\hat{\sigma_u}, \hat{\sigma_v}, \hat{\sigma_w}$	0.2, 0.2, 1.0 vx [66]
vector error, experimental, $\sigma_u, \sigma_v, \sigma_w$	0.004, 0.003, $0.01\,\mathrm{m\,s^{-1}}$
vector error, phase-averaged $\bar{\sigma_u}, \bar{\sigma_v}, \bar{\sigma_w}$	0.004, 0.003, $0.01\,\mathrm{m\,s^{-1}}$
central difference, truncation error, τ	$0.375\frac{\partial^3 u}{\partial x^3}$
central difference, noise error, $\epsilon_x, \epsilon_y, \epsilon_z$	0.032, 0.024, $0.079\,\mathrm{s^{-1}}$
phase-averaged λ_{ci}-Criterion error, ϵ_λ	$0.14\,\mathrm{s^{-1}}$

Table 3.3: Reference table with calculated errors

The eigenvalues are then calculated of each matrix, and the maximum, unique, imaginary eigenvalues, the swirling strength, are then compared. The difference between these values is averaged over one million instances. The average value is $0.089\,\mathrm{s^{-1}}$ with a standard deviation of $0.14\,\mathrm{s^{-1}}$. Thus, as a conservative estimate, the noise error in calculation of the swirling strength, denoted ϵ_λ is taken as $0.23\,\mathrm{s^{-1}}$. For reference, isocontours of swirling strength are formed at values $\lambda_{ci} \approx 15$, thus, there is approximately an error of 1.5 % in the calculation of λ_{ci}-Criterion.

In addition to estimating the error in this analysis, the convergence of the velocity measurements was also shown using up to 500 image pairs. The convergence of each velocity component is shown in figure 3.14 for a 5×5×5 region of vectors, at various locations in the measurement volume. At each location 2 plots are shown, one normalized by the freestream velocity (left column) and one normalized by the final converged value of each velocity component (right column). The first location is far from the wing surface, towards the downstream end of the volume, near the half span. In figure 3.14a, u' converges relatively quickly to $1.75u_\infty$, v' converges slightly slower to $1.2u_\infty$, and w' converges slowly to $1.55u_\infty$.

The plot in figure 3.14b, it is shown that u' converges to less than than 1 percent variance from the converged value after only 100 sample, where the same convergence for v' requires 300 samples, and 460 samples are required for less than 1 percent variance for w'. The reduced convergence of w' is expected due to the reduced accuracy of this measurement. At the second location, near the formation of a dual-vortex system, the velocities in figure 3.14c converge more slowly to values of $-2.4u_\infty$, $-u_\infty$, and $-0.4u_\infty$ for u', v', and w', respectively. In the plot shown in figure 3.14d, the u' and v' convergence is again quicker, requiring 200 and 290 samples, respectively. The w' velocity requires 440 samples to converge within 1 percent of the final value. The accuracy of the w' component will be considered when examining the results herein.

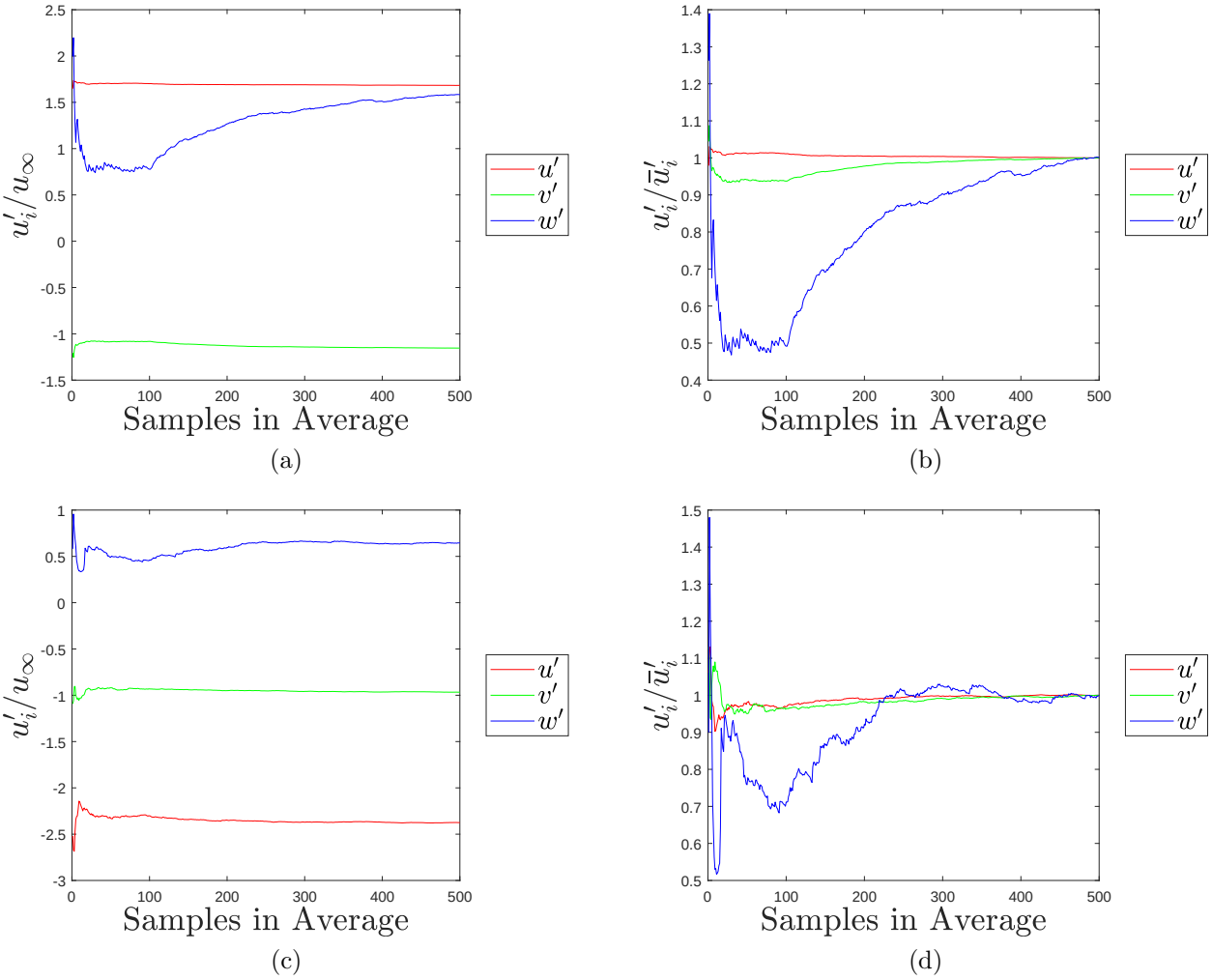

Figure 3.14: Velocity convergence of all three velocity components normalized by the freestream velocity (a,c) and normalized by the final converged value (b,d) at: (a,b) a location far from the wing near the x' maximum and the z' midpoint; (c,d) near the formation of the dual-vortex structure;

Chapter 4

Results

The following chapter contains a description of the cases outlined in table 3.1. The ensemble-averaged vortical structures and streamlines are shown providing an close up look of the vortex evolution for each kinematic case. Additionally, instantaneous volumetric velocity fields are presented, the first of their kind for a maneuvering wing.

4.1 Ensemble-Averaged Results

4.1.1 Purely Pitching

The purely pitching kinematics serve to establish a baseline characterization, which the results of the simultaneously pitching and rolling kinematics will be compared against. Two kinematic cases were prescribed for the purely pitching maneuver, $P_{.5}$ and $P_{.2}$, having a reduced pitch rate of 0.50 and 0.19, respectively. The evolution of vortex structures created by kinematic case $P_{.5}$ (figure 4.1a and Movie 1) is characterized by the presence of a cylindrical and attached LEV in the formation and growth stage, which ends at $t' \leq 0.52$. In this stage, there is little change to the topology of the LEV. During the transitional stage, the span of $0.52 < t' < 0.61$, the center region of the LEV begins to slightly lift up from the surface. By $t' = 0.61$, the LEV is clearly detached from the leading edge; forming an arch vortex that spans from root to tip, where the legs of the vortex are pinned to the surface. In the next and final phase, $t' = 0.79$, the center span of the LEV travels further away from the leading edge in both the chordwise and wing normal directions, while the legs remain pinned near the surface. This description agrees well with the results of Yilmaz and Rockwell [4] and Jantzen et al. [20]. It is noted that the LEV has *slightly* left the surface at the root, and

this is hypothesized to be an effect of the rod that the wing is attached to or the mounting bracket that extends along the chord, seen in the solid body in each of the figures.

A similar development of the LEV is seen at the slower pitch rate, $P_{.2}$ (figure 4.1b and Movie 2), where the LEV is cylindrical and stable during the formation and growth stage, $t' \leq 0.92$. During the transitional stage, the LEV forms into a shallow arch vortex, over the range $0.92 < t' < 1.31$. A major difference from $P_{.5}$ occurs during the detached stage, $t' \geq 1.31$, where the LEV lifts up from the surface to a y' value nearly twice that of the arch vortex in $P_{.5}$; leaving a large void near the leading edge. In this region, two additional LEVs form, also pinned at tip, to create a triple-vortex system by the end of the motion. It is suggested that the vortex system continues to remain pinned throughout the motion, although the region of data at the root was not gathered to support this hypothesis.

It is interesting to consider these results in a similar manner to the "time-shift" described by Yilmaz et al. [27], who used an $AR = 2$ wing at a $Re = 10,000$ articulated in a pitch-up motion to $\alpha_{\text{geo}} = 45°$ immediately followed by a pitch-down motion. The two previous cases also follow the trend described by Yilmaz et al. [27], who found that vortical structures were advanced in time as k was increased. Through comparison of the first measured time of the detached regime, it is seen that increasing k has advanced this nondimensionalized time ($t' = 1.38 \rightarrow 0.92$ for $k = 0.2 \rightarrow 0.5$). Conversely, by comparing vortex topology of the two cases, it is found that the LEV of $k = 0.2, t' = 0.70$ most closely resembles the LEV in $k = 0.5, t' = 0.68$ at nearly the same nondimensionalized time. This conclusion agrees well with the observations of Granlund et al. [17], who saw a collapse of the maximum lift coefficient for various reduced pitch frequencies when scaled by the convective time, especially if one assumes that the evolution of the lift coefficient is closely related to the topology of the LEV.

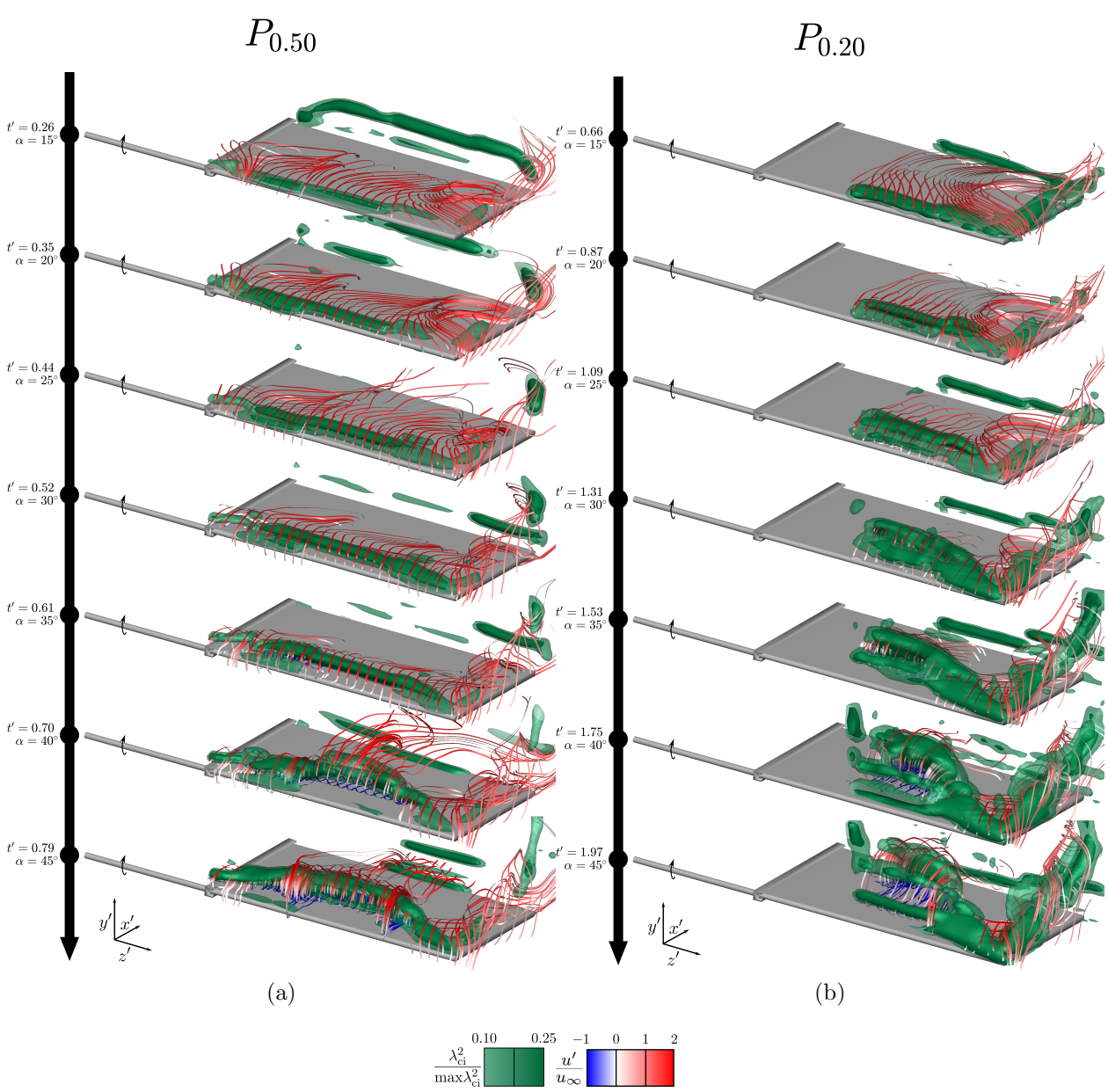

Figure 4.1: Phase-averaged results shown with isocontours colored by normalized swirling strength and stream ribbons colored by normalized chordwise-velocity u' for (a) $P_{.5}$ and (b) $P_{.2}$

4.1.2 Purely Rolling

The primary purpose of studying the purely rolling maneuver in the context of this dissertation is to establish the vortex structures that are formed as a result of the rolling *environment*. In the Section 5.1, the simultaneously pitching and rolling wing is cast as a pitching wing in a rolling environment for comparison to a purely pitching wing. Here, two advance ratios were prescribed at various effective angles of attack. The phase-averaged results of each advance ratio, $J = 0.54$ and 1.36, at $\alpha_{\text{eff}} = 33°$ are shown in figure 4.2, and Movies 3 and 4, again visualized using the previously described methodology.

The intricate evolution of the vortex structure formed by $R_{.54,33}$ begins with a cylindrical shape in the formation and growth stage at $t' \leq 0.77$. As the LEV enters the transitional stage, $0.77 < t' < 1.68$, a narrow arch vortex develops at about 80 percent of the span, which grows in the $+y'$ direction as it shifts down-chord. During this motion, a dual-vortex system forms where vortices are connected near the root and tip, becoming well-established by $t' = 1.10$. This closely resembles the dual-vortex system described by Bross et al. [30]. In the literature, the dual-vortex system has not been strictly defined for rolling wings, although similar descriptions exist in the case of delta wings [80]. Thus, this paper defines a dual-vortex system as a vortex system containing a localized bifurcation of a primary LEV into two distinct vortices. Later, in the detached regime at $t' \geq 1.68$, the two components of the dual-vortex system become entangled and convect downstream. A new LEV forms, which again bifurcates into a dual-vortex system.

For the slower roll rate, $R_{1.36,33}$, a cylindrical LEV is observed in the formation and growth stage at $t' \leq 0.29$. In the next phase, the LEV has remained cylindrical and left the surface slightly. By $t' = 1.15$, the LEV is clearly detached from the wing and a resemblance of a dual-vortex system is being convected away from the leading edge. Throughout the rest of the recorded motion, a new LEV is formed and multiple structures are shed into the freestream. Of principle interest in this case is the similarity to $R_{.54,33}$, explicitly, that a dual-vortex system is formed and shed in each case. For $R_{.54,33}$, the dual-vortex system is

formed and shed by $t' = 2.58$, whereas the similar process of $R_{1.36,33}$ only requires $t' = 2.01$ to complete. By describing this observation as a time-shift and/or time-scaling of the vortex structure, akin to the results from purely pitching cases, it can be stated that decreasing the advance ratio J delays the evolution of the vortex structures. The likeness in the evolution of these two roll cases agrees well with the observations made by Bross et al. [30], who concluded that similar streamline topology features appear at different ϕ when J is varied.

Additional purely rolling cases are presented here, where the α_{geo} was altered to explore the effect of α_{eff} on the vortical evolution. In $R_{.54,23}$ and $R_{.54,43}$, shown in figures 4.3a and 4.3b (Movies 5 and 6), respectively, the vortex structure developed similarly to $R_{.54,33}$. Emphasis is again placed on the development of the dual-vortex system, which is observed to move in physical space as a result of altering α_{eff}. In the development of $R_{.54,23}$, the dual-vortex system appears to split closer to the tip (almost out of the center measurement volume) when compared to $R_{.54,33}$. Following this trend, the bifurcation point of the dual vortex system is not visible in the phases of $R_{.54,43}$; suggesting that it is located in the root volume (not recorded for this case). It follows that increasing the α_{eff} shifts the bifurcation point of the LEV towards the root. Another way of framing this relationship is to use the observed or estimated spanwise location that the bifurcation occurs, and calculate the *local* effective angle of attack at that location. With the three cases presented here, this local effective angle of attack is found to be roughly the same. The same relationship can be observed for the slower roll rate through comparison of $R_{1.36,43}$ in figure 4.4a (Movie 7) and the previously shown $R_{1.36,33}$.

Lastly, two cases were measured using a different radius of gyration, $r_{.54,33}$ and $r_{1.36,33}$. Beginning with the smaller advance ratio, $r_{.54,33}$ is shown in figure 4.5a (Movie 8) a cylindrical LEV forms in the formation and growth stage. Through the transitional stage, it appears that narrow arch vortex is forming, however, without the tip region is impossible to know for sure. As a whole, it seems that the LEV is evolving slower with the shorter R_g/c. For the larger advance ratio $r_{1.36,33}$ in figure 4.5b (Movie 9), the evolution varies from the $R_{1.36,33}$

greatly by the transitional stage. For $r_{1.36,33}$ a multiple vortex system is formed and many of the vortex structures remain connected in the isocontours of swirling strength throughout the motion, a stark contrast to the distinct vortices of $R_{1.36,33}$.

In the context of describing the "rolling environment" that the pitching motion will be executed in, the following results are most critical: (1) at both advance ratios, a dual-vortex system is formed and shed from the leading edge; creating a similar environment earlier in the motion, and (2) the changing effective angle of attack is seen to shift structures physically along the span of the wing.

4.1.3 Simultaneously Pitching and Rolling

Four different combinations of pitch rate and roll rate were prescribed, each yielding a different k_{Rg} value (recall $k_{Rg} = \dot{\alpha}_{\text{eff}}/2V_{R_g}$). The first, $S_{.46,.54}^{.22}$ is presented in figures 4.6a (Movie 10). For this case, image pairs were gathered every 5° from $\alpha_{\text{eff}} = 15°$ to 45°, corresponding to roll angles between $\phi = 30°$ to 49°. During the formation and growth stage, the LEV is cylindrical across the leading edge, but slowly transforms into a more conical shape by $t' = 1.20$. As the LEV enters the transitional stage, an arch vortex forms that is not quite as expansive as the arch vortex formed in $P_{.5}$, yet is broader than the narrow arch vortex formed by $R_{.54,33}$. From this arch vortex, a dual-vortex system forms while still connected to the wing tip. At $t' = 1.60$, regions of the dual-vortex system have clearly left the leading edge; marking the beginning of the detached regime. By the end of the motion, the dual-vortex system has risen further from the leading edge and traveled down-chord, coupled with a broadening of the spanwise detachment region toward the root. Despite this evolution, the LEV has remained pinned at the wing tip throughout the entire motion. The next kinematic case, $S_{.42,.54}^{.20}$ in figure 4.6b and Movie 11, has nearly identical wing kinematics as $S_{.46,.54}^{.22}$, with only a slightly lesser reduced pitch rate. It follows that, with such similar wing kinematics, the vortex evolution and topology is analogous, although the progression of the LEV through the stages has been delayed in t'. This delay will be further detailed and

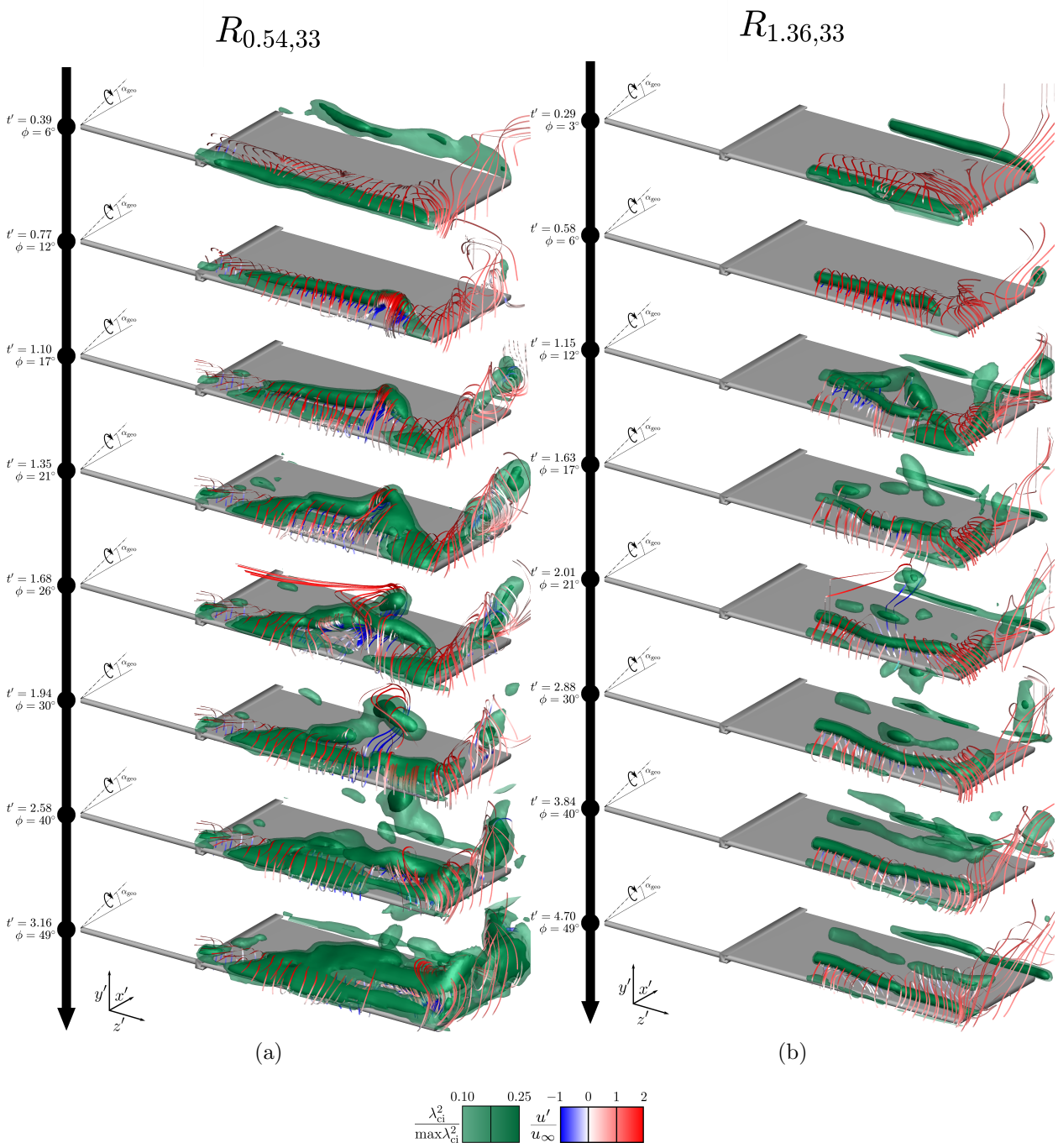

Figure 4.2: Phase-averaged results shown with isocontours colored by normalized swirling strength and stream ribbons colored by normalized chordwise-velocity u' for (a) $R_{.54,33}$ and (b) $R_{1.36,33}$

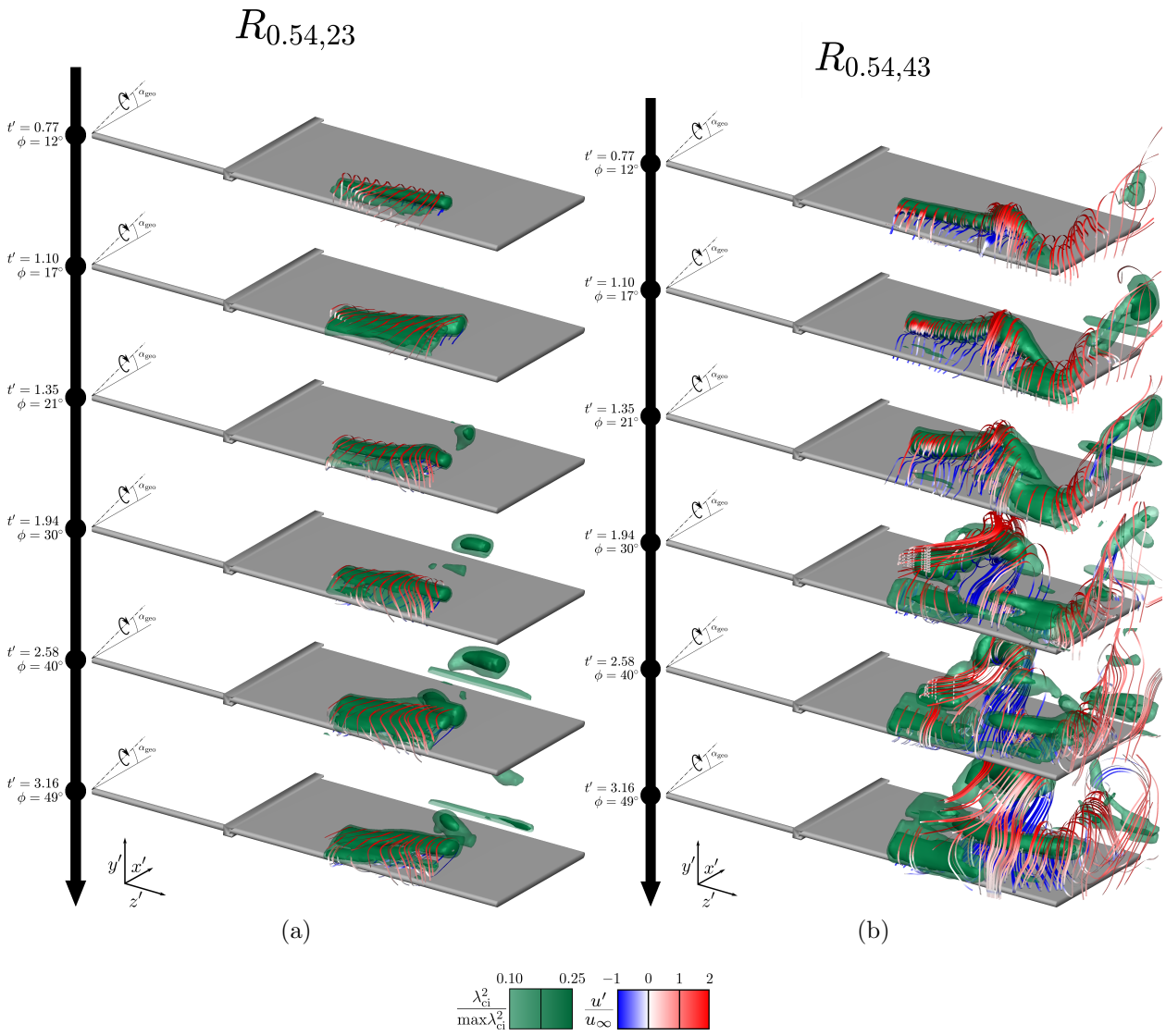

Figure 4.3: Phase-averaged results shown with isocontours colored by normalized swirling strength and stream ribbons colored by normalized chordwise-velocity u' for (a) $R_{.54,23}$ and (b) $R_{.54,43}$

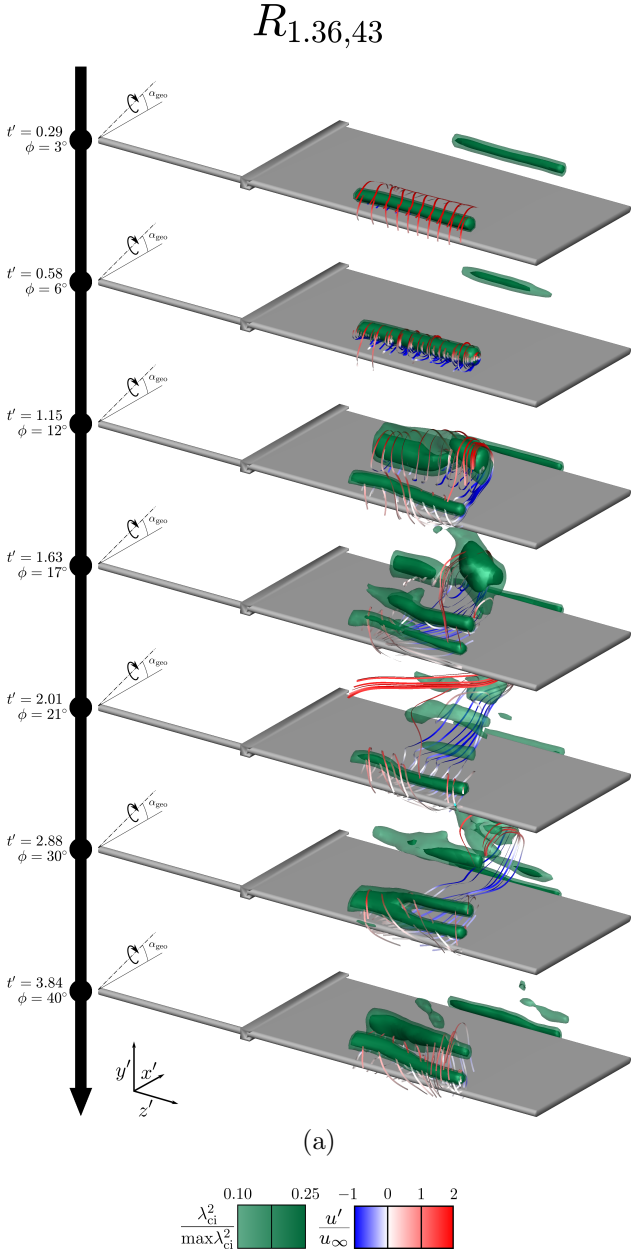

Figure 4.4: Phase-averaged results shown with isocontours colored by normalized swirling strength and stream ribbons colored by normalized chordwise-velocity u' for $R_{1.36,43}$

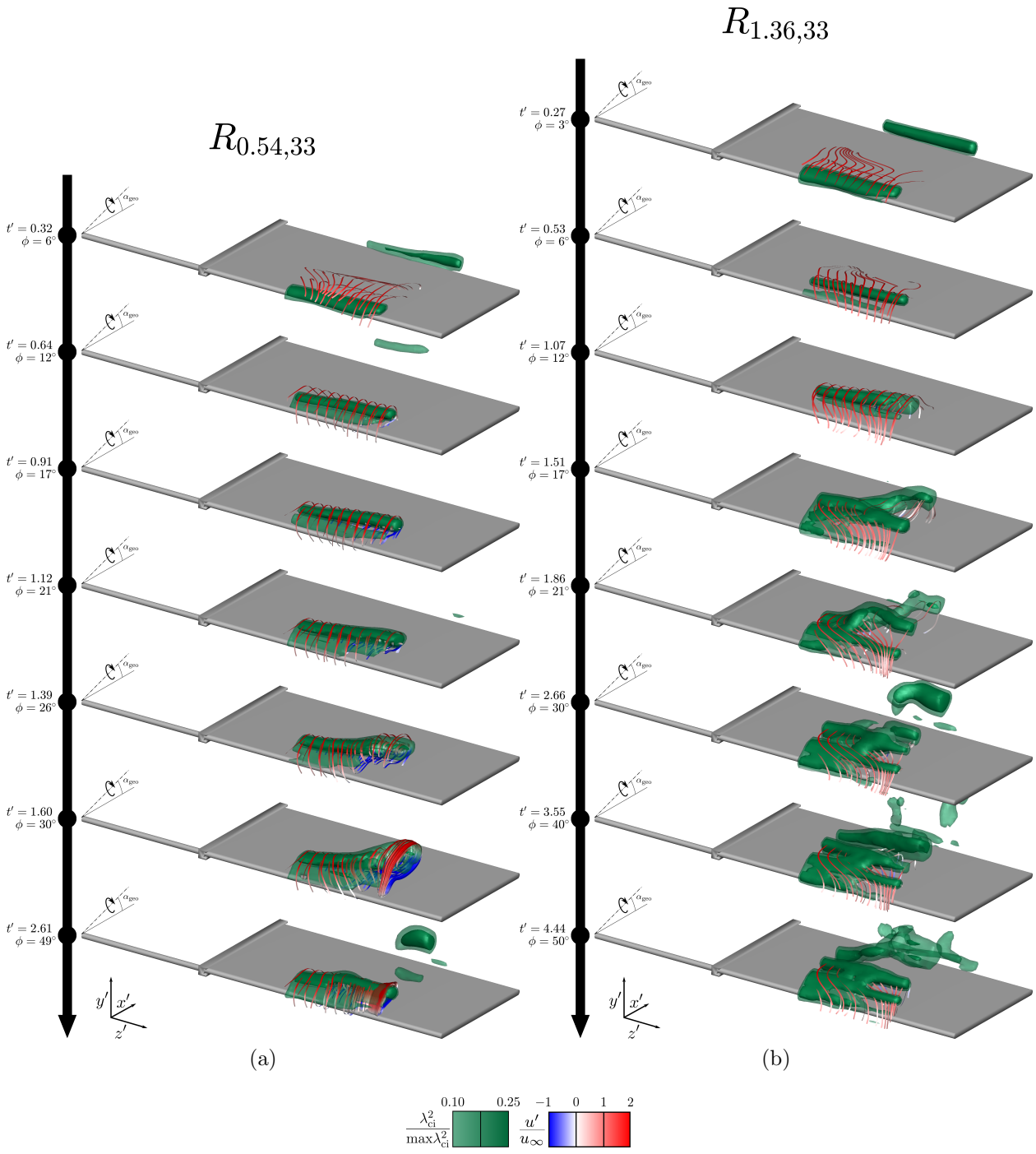

Figure 4.5: Phase-averaged results shown with isocontours colored by normalized swirling strength and stream ribbons colored by normalized chordwise-velocity u' for (a) $r_{.54,33}$ and (b) $r_{1.36,33}$

quantified in the next section. An additional result from the $S^{.20}_{.42,.54}$ case is that the vortex topology in the final measurement phase $t' = 1.75$ most closely matches the phase of $S^{.22}_{.46,.54}$ that is closest in dimensionless time ($t' = 1.80$) as opposed to identical α_{eff}. This similarity provides verification of the selecting the *relative* convective time, τ, to nondimensionalize time.

The next case, $S^{.50}_{1.05,.54}$ figure 4.7a (Movie 12), has an identical advance coefficient to the two previous cases, but a faster reduced pitch rate. The result is a relatively quick prescribed motion in which the LEV does not evolve as drastically as the previous cases. During the formation and growth stage $t' \leq 0.53$ a cylindrical LEV is formed across the leading edge. The transitional stage is brief, with a narrow arch vortex forming, closely resembling the narrow arch vortex in the early stages of $R_{.54,33}$. By the next phase, the narrow arch vortex has left the surface and progressed slightly down the chord, beginning the detached stage at $t' = 0.70$. Overall, it is found that the more than doubling of the reduced pitch rate compared to $S^{.22}_{.46,.54}$, has dramatically advanced the evolution of the LEV, specifically the time to a detached vortex. The final case, $S^{.37}_{.46,1.36}$ in figure 4.7b (Movie 13), utilizes the larger advance ratio (slower roll rate) and a reduced pitch rate identical to $S^{.22}_{.46,.54}$ and $P_{.5}$. In the formation and growth stage $t' \leq 0.59$, a cylindrical LEV forms and remains relatively unchanged until the transitional stage. A second LEV is formed in the transitional stage ($0.59 < t' < 0.94$), where both LEVs join and are pinned at the tip. It is likely that the 2 LEVs also join in the root region, although measurements were not taken for this case. Thus, it follows that the 2 LEVs are a dual-vortex system with elongated, cylindrical members. At $t' = 0.83$, the second LEV (closer to the leading edge) in the dual-vortex system has dramatically weakened and the first LEV becomes more coherent. At $t' = 0.94$, the first LEV is detached and has progressed down the chord, and continues to do so in the final phase. The second LEV strengthens as the first LEV moves away from the leading edge, both of which remain cylindrical. Interestingly, the time required for $S^{.37}_{.46,1.36}$ to progress through the stages of vortex evolution is significantly faster than $S^{.22}_{.46,.54}$. Since both of these cases

use the same reduced pitch rate, the difference can be attributed to the advance ratio. The observation between these two cases follows the conclusion from the purely rolling section: that decreasing the advance ratio J delays the evolution of the vortex structures.

One case is shown at the shorter R_g/c, $s_{.46,1.36}^{.37}$ in figure 4.8a (Movie 14). Here the development of the vortical structures as a whole are remarkably similar to $S_{.46,1.36}^{.37}$. This similarity will be discussed in Chapter 5.2, where the similarity will be quantified to deepen the understanding of the effect of R_g/c on the vortex topology and evolution.

For the two previous kinematic cases, $S_{1.05,.54}^{.50}$ and $S_{.46,1.36}^{.37}$, measurements were made after the pitching motion was complete and the rolling motion was allowed to continue, shown in figure 4.9. In each case, the LEV began to progress down the chord, each convecting about 10 percent of the chord after about half of convective time since the pitching motion had stopped. This suggests that the pitching motion plays a major role in stabilizing the LEV; keeping it present at the leading edge. This role may simply be increasing the energy that is entrained into the vortex. In which case, accelerating the roll rate when the pitching motion has ended may assist in keeping the LEV at the leading edge. Interestingly, in both cases, a new LEV has yet to form, despite the elapsed time and ample space to do so.

4.2 Instantaneous Results

A brief description of the instantaneous data is presented in this chapter, which aims to illustrate the differences in vortex topology in the instantaneous flow compared to the ensemble-averaged flow fields. Each of the baseline cases are shown here, with a single instantaneous volume shown at each spanwise measurement location. In the instantaneous results, the data is not stitched together at the seams as it was in the ensemble averaged, instead it is plotted simultaneously. The reader is reminded that instantaneous data was not taken for the entire wing at the same instant, instead the results shown here are a composite of 3 instances. The data was somewhat particularly selected for continuity of vortex structures across edges of the measurement volumes, but it is noted that alignment

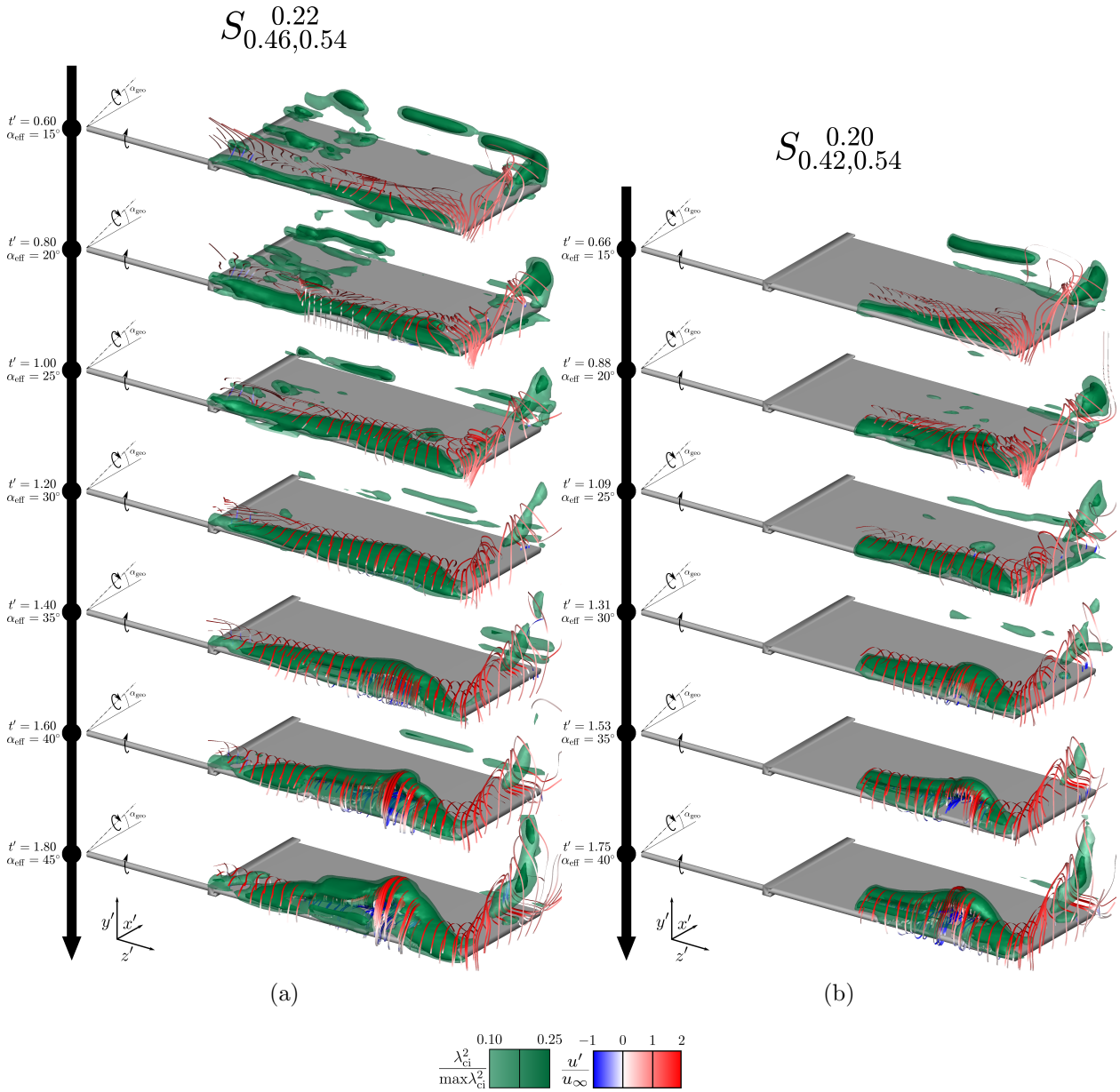

Figure 4.6: Phase-averaged results shown with isocontours colored by normalized swirling strength and stream ribbons colored by normalized chordwise-velocity u' for (a) $S^{22}_{.46,.54}$ and (b) $S^{20}_{.42,.54}$

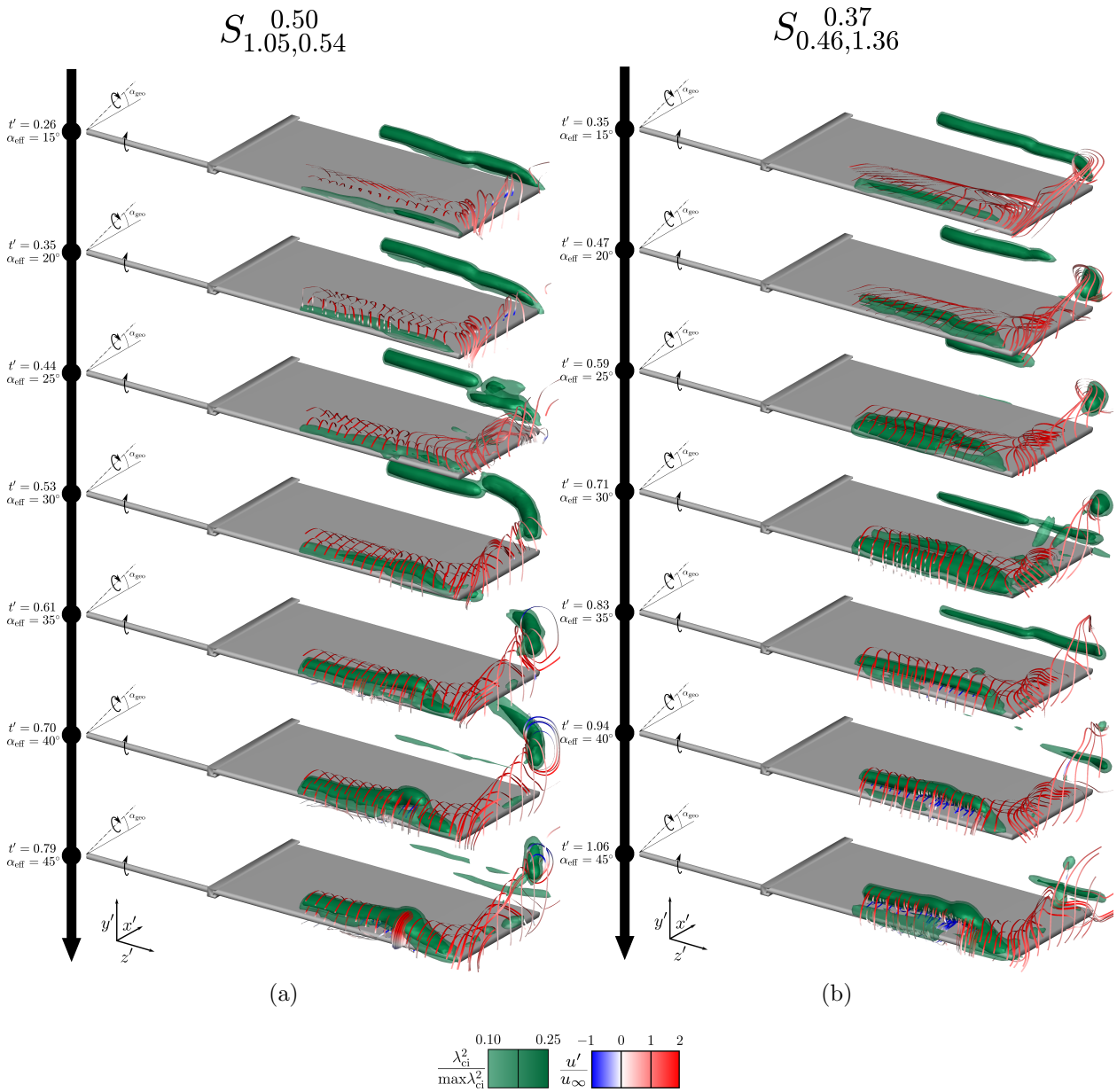

Figure 4.7: Phase-averaged results shown with isocontours colored by normalized swirling strength and stream ribbons colored by normalized chordwise-velocity u' for (a) $S^{.50}_{1.05,.54}$ and (b) $S^{.37}_{.46,1.36}$

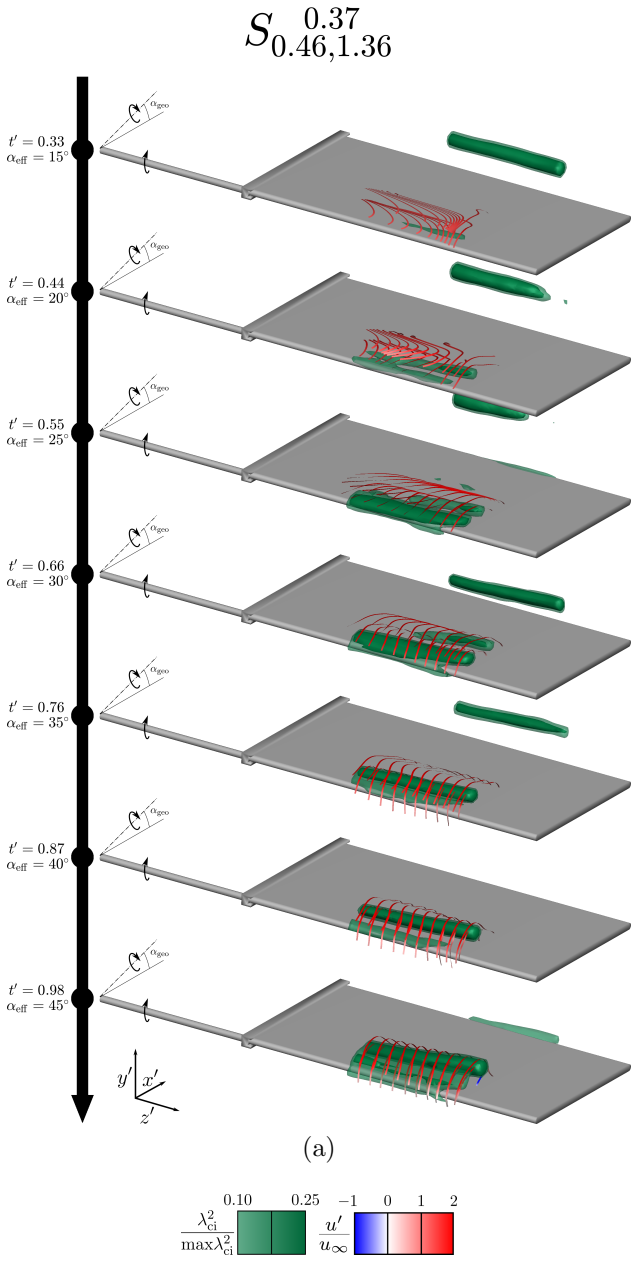

(a)

Figure 4.8: Phase-averaged results shown with isocontours colored by normalized swirling strength and stream ribbons colored by normalized chordwise-velocity u' for $s^{.37}_{.46,1.36}$

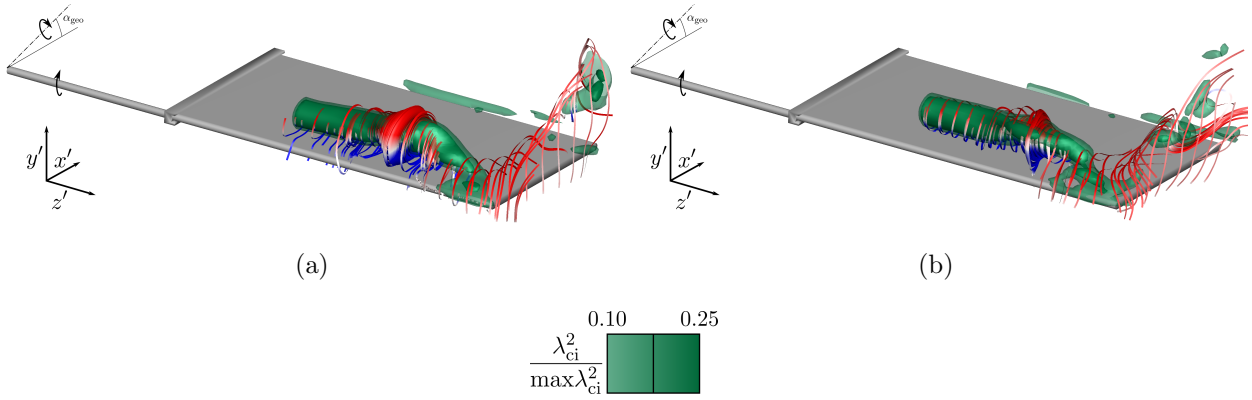

Figure 4.9: Comparison of vortex structure from post-pitch rolling motion: (a) $S_{1.05,.54}^{.50}$ $t' = 1.34$ and (b) $S_{.46,1.36}^{.37}$ $t' = 1.46$

of structures was observed throughout the data set, proving that the careful calibration was successful and the repeatability of the formation processes.

To begin, a comparison between the phase-averaged and the instantaneous vortex topology for case $P_{.5}$ is presented in figure 4.10. The isocontours of normalized swirling strength are shown for $P_{.5}$ at $t' = 0.78$. The instantaneous volume, figure 4.10b, appears 'noisier,' as the smaller structures have not been averaged out. The main structures are essentially the same as the ensemble averaged field, even down to the extent of the TiV. Throughout this phase, only minor differences are seen from phase-averaged results, primarily an estimated 25 percent variation in the size of the isocontour displaying the arch vortex, while keeping the same shape.

A comparison between the phase-averaged structure and the instantaneous vortex topology for case $R_{.54,33}$ is shown in figure 4.12. Again the overall trends between the vortex topology between the two cases is the are similar. However, the same level of isocontour does not illustrate as completed of a structure in the instantaneous case. Notably, one of the detached legs of the dual-vortex system does not extend as far towards the wing tip as it does in the phase-averaged results. This phase was selected because of the more complex vortex topology in the phase-averaged results and much of that complexity is seen in the

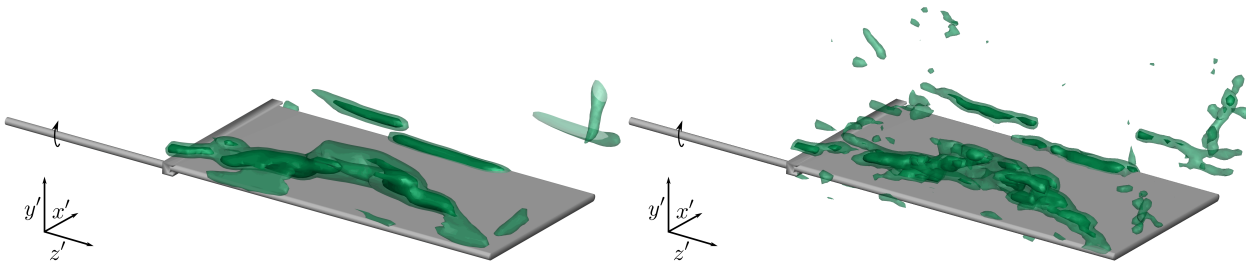

(a) (b)

Figure 4.10: A comparison between phase-averaged and instantaneous vortex topology, where the instantaneous data is presented with volume at each measurement volume, placed side by side (no stitching) for $P_{.5}$ at $t' = 0.78$

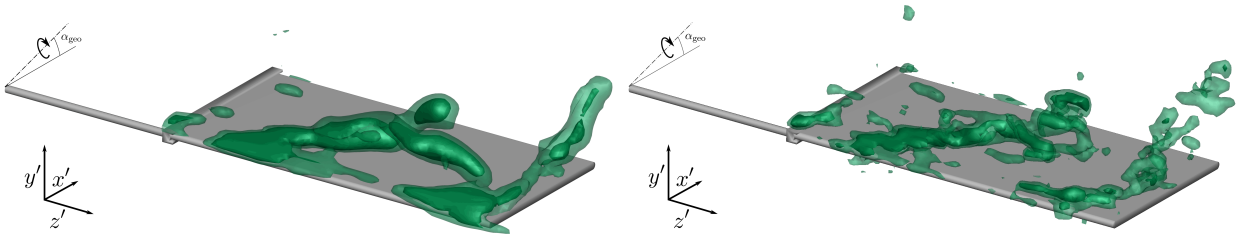

(a) (b)

Figure 4.11: A comparison between phase-averaged and instantaneous vortex topology, where the instantaneous data is presented with volume at each measurement volume, placed side by side (no stitching) for $R_{.54,33}$ at $t' = 1.68$

instantaneous. However, when compared to the previously presented purely pitching comparison, the instantaneous results from roll do not match the ensemble-average as well. Most notably, in an estimated 20 percent of the instantaneous volumes show an LEV across the entire span of the LE, which is partially shown in the phase-averaged field. Seeing that a new LEV has formed by the next phase, it follows that this phase is right on the cusp of formation, and there may exist a mechanism that is triggering premature development of this LEV in a limited number of samples.

Lastly, a comparison between the phase-averaged structure and the instantaneous vortex topology for $S^{.37}_{.46,1.36}$ is shown in figure 4.12. The data has been presented in an identical

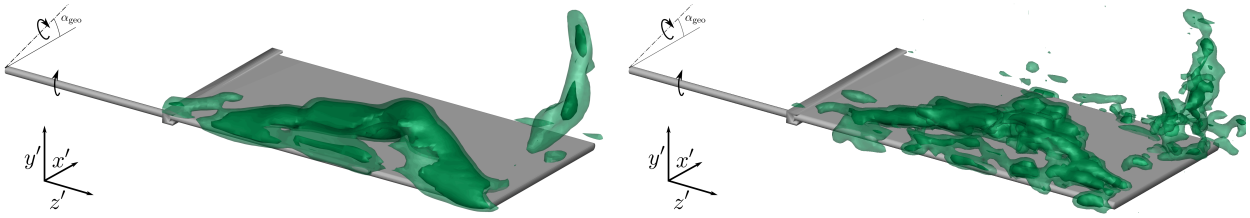

(a) (b)

Figure 4.12: A comparison between phase-averaged and instantaneous vortex topology, where the instantaneous data is presented with volume at each measurement volume, placed side by side (no stitching) for $S_{.46,.54}^{.22}$ at $t' = 2.674$

fashion to the previous cases and again the overall trends between the vortex topology between the two cases is the are essentially the same. Throughout the phase, the major differences from the phase-averaged results are the extent of the dual-vortex system and the tip vortex. Specifically, the LEV nearest to the LE in the dual vortex system is below the threshold of the swirling strength isocontour, a possible indication of the delayed formation of the this vortex. The isocontours marking the TiV occasionally connect to the dual-vortex system. From visual inspection, there is no apparent correlation between the presence of the dual-vortex system and the connection of the TiV to the LEV.

Chapter 5

Discussion

While the description of the results in the previous chapter is useful and informative, further analysis and comparisons of different kinematic cases in this chapter provides a deeper understanding of the effects of each prescribed motion on the vortex evolution and topology.

5.1 The k_{Rg} Parameter

Through selection of the parameter space, this study has driven towards an understanding of the k_{Rg} parameter. In the previous section, each case was detailed and broken down into 3 stages of vortex evolution, with topology assigned to each stage. For ease, the t' of each stage is tabulated in table 5.1 and the topology at each stage is described in table 5.2.

A natural comparison between purely pitching cases and simultaneously pitching and rolling cases is found by matching the k_{Rg} parameter for each case (recall that $k = k_{Rg}$ for purely pitching). There are two instances of matching to explore $k_{Rg} = 0.2$ and $k_{Rg} = 0.5$. The most apparent consequence from the addition of the rolling motion is the removal of symmetry in the flow over the leading edge, thus disrupting the symmetry of the vortex structure. This is reflected in table 5.2 where the asymmetric vortex topologies, such as

Vortex Evolution								
	$P_{.2}$	$P_{.5}$	$S^{.20}_{.42,.54}$	$S^{.22}_{.46,.54}$	$S^{.37}_{.46,1.36}$	$S^{.50}_{1.05,.54}$	$R_{1.36,33}$	$R_{.54,33}$
Form. & Growth	≤ 0.92	≤ 0.52	≤ 1.31	≤ 1.20	≤ 0.59	≤ 0.53	≤ 0.29	≤ 0.77
Transitional	⋮	⋮	⋮	⋮	⋮	⋮	⋮	⋮
Detached	≥ 1.38	≥ 0.61	≥ 1.75	≥ 1.60	≥ 0.94	≥ 0.70	≥ 1.15	≥ 1.68

Table 5.1: Tabulated dimensionless time t' ranges of the vortex evolution stages for each kinematic case

Vortex Topology								
	$P_{.2}$	$P_{.5}$	$S_{.42,.54}^{.20}$	$S_{.46,.54}^{.22}$	$S_{.46,1.36}^{.37}$	$S_{1.05,.54}^{.50}$	$R_{1.36,33}$	$R_{.54,33}$
Form. & Growth	CYL	CYL	CYL/CON	CYL/CON	CYL	CYL	CYL	CYL/CON
Transitional	ARV	CYL	NARV	NARV	CYL/DVS	NARV/DVS	DVS	NARV/DVS
Detached	DVS/MVS	ARV	DVS	DVS	CYL/DVS	NARV/DVS	CYL	DVS

Table 5.2: Descriptions of the vortex topology at vortex evolution stages for each kinematic case, where

CYL: cylindrical
CON: conical
ARV: arch vortex
NARV: narrow arch vortex
DVS: dual-vortex system
MVS: multiple-vortex system

conical and a narrow arch vortex, are only present in $S_{.42,.54}^{.20}$ and $S_{1.05,.54}^{.50}$. In regards to the vortex evolution, it is seen that the addition of the rolling motion delays the progression of the LEV through the defined stages. In table 5.1, the delay in the normalized time required for a detached vortex increases from 1.38 to 1.75 from $P_{.2}$ to $S_{.42,.54}^{.20}$. At $k_{Rg} = 0.5$ the delay is less substantial: from 0.61 to 0.70 ($P_{.5}$ and $S_{1.05,.54}^{.50}$). When considering both the LEV topology and evolution simultaneously, especially through a comparison of Movie 2 versus 11 and Movie 1 versus 12, the total effect of the rolling motion is more easily realized. Succinctly, the addition of a rolling motion to a pitching wing, while matching k_{Rg}, delays the evolution of the LEV and reduces the extent of evolution across the span to a localized region. While the impediment of the evolution in respect to t' is similar to the time-shifts described by Yilmaz and Rockwell [4] and Bross et al. [30], the localization of the evolution has not been previously documented in this manner. A direct quantification of the time-shift cannot be calculated in the same method as Yilmaz and Rockwell [4] (t'/k_{Rg}) because the k_{Rg} values are matched, thus there is no variation with k_{Rg}.

Beyond matching with purely pitching cases, the k_{Rg} parameter proves useful for comparing the four cases of simultaneously pitching and rolling motions. Specifically regarding the evolution of the LEV, a clear trend is seen when the tabulated non-dimensional time

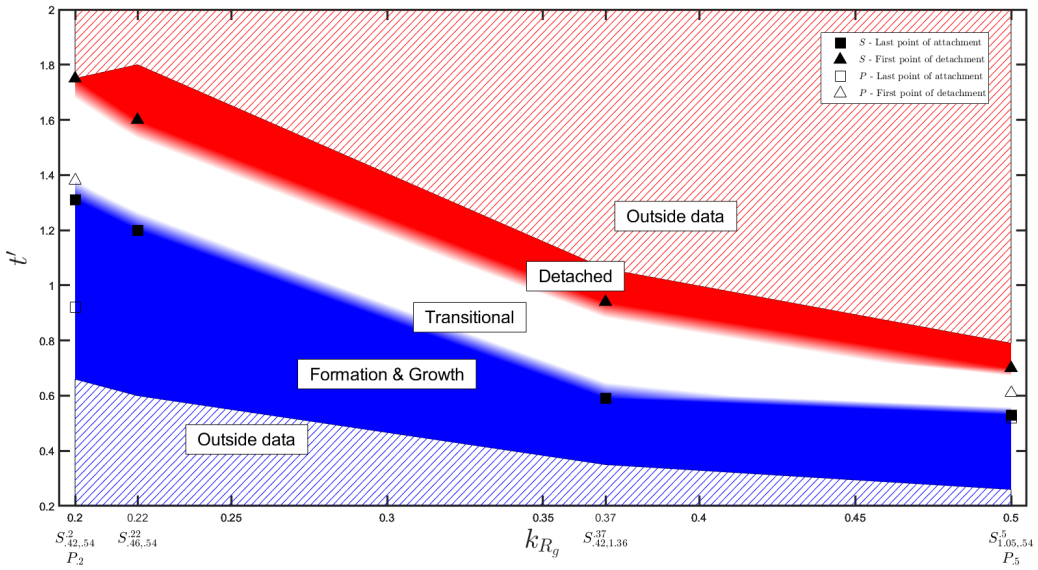

Figure 5.1: Map of vortex evolution stages as a function of k_{Rg} and t', where each of the cases are labeled below the x-axis, at the appropriate k_{Rg} value

values in table 5.1 are plotted against k_{Rg}. This plot is shown in figure 5.1, where purely pitching cases and simultaneously pitching and rolling cases are plotted in the $k_{Rg} - t'$ plane. For only the simultaneously pitching and rolling cases, each stage of vortex evolution is colored across the space to create a map to predict the vortex stage at a k_{Rg} and t' value. The points from table 5.1 are plotted as solid symbols for simultaneous cases and hollow for purely pitching. Overall, it is evident that increasing k_{Rg} accelerates the evolution of the LEV through the vortex stages and advances the evolution in nondimensionalized time. This is inherently different from the previously described time-shifts, as the total life cycle of the LEV is actually compressed in the t' space as k_{Rg} is increased, in addition to shifting forward in time. Although this effect can be seen in both the purely pitching cases and the simultaneously pitching and rolling cases, the points from the purely pitching case do not fit the map formed by the simultaneous cases. In fact, the misalignment of these trends illustrate a previous observation, that the additional rolling motion stabilizes the LEV; delaying it's development. A consequence of the misalignment is that the map in figure 5.1 is only valid for simultaneously pitching and rolling cases.

To further explore the effect of the rolling reference frame, a comparison between a simultaneously pitching and rolling case and a purely rolling case using the same roll rate is presented. Returning to figures 4.2a and 4.6a (movies 3 and 10), the phase-averaged results of $R_{.54,33}$ and $S^{.22}_{.46,.54}$ are compared. After a similar start up, the final 3 phases of each kinematic case are where the vortex evolution between the cases begins to diverge. After $t' = 1.35$ for $R_{.54,33}$, the dual-vortex system comes unpinned at the tip, and later sheds. Most closely resembling this structure, the flow at $t' = 1.80$ ($\alpha_{\text{eff}} = 45°$ and $\phi = 49°$) for $S^{.22}_{.46,.54}$ also contains a clearly defined dual-vortex system that is pinned at the wing tip. Thus, it can also be concluded, that the addition of a pitching motion to a rolling motion delays the vortex evolution in both t' and roll angle ϕ. A similar comparison can be made between $R_{1.36,33}$ and $S^{.37}_{.46,1.36}$, but the final phase of $S^{.37}_{.46,1.36}$ is only at $t' = 1.06$, which is closest to the third phase of $R_{1.36,33}$ at $t' = 1.15$. At this time in $R_{1.36,33}$, a dual-vortex system has formed that does not resemble the dual vortex system that was formed in $S^{.37}_{.46,1.36}$. Although, using the previous conclusion that the addition of the pitching motion delays the vortex evolution, it may be that the dual-vortex system in $S^{.37}_{.46,1.36}$ later develops into a state the resembles the dual-vortex system of $R_{1.36,33}$. A future study may wish to explore a parameter similar to k_{Rg}, but instead cast in terms of roll, to better understand the relation between a rolling wing and a simultaneously pitching and rolling wing.

5.2 Correlation Approach

Using the correlation approach described in section 3.3, a complete correlation map was formed, shown in figure 5.2a as an image, where each pixel corresponds to the correlation between two ensemble-averaged phases. The bright diagonal represents the auto-correlations of each phase, where $r = 1$. The plaid like structure is a result of the grouping of phases of identical wing kinematics. As an example of how each value is determined, two phases have been highlighted in this image. The row equating to correlations versus $S^{.22}_{.46,.54}$ at $t' = 2.079$ is outlined in a green box and the column representing $R_{.54,33}$ at $t' = 0.745$ is outlined in a red

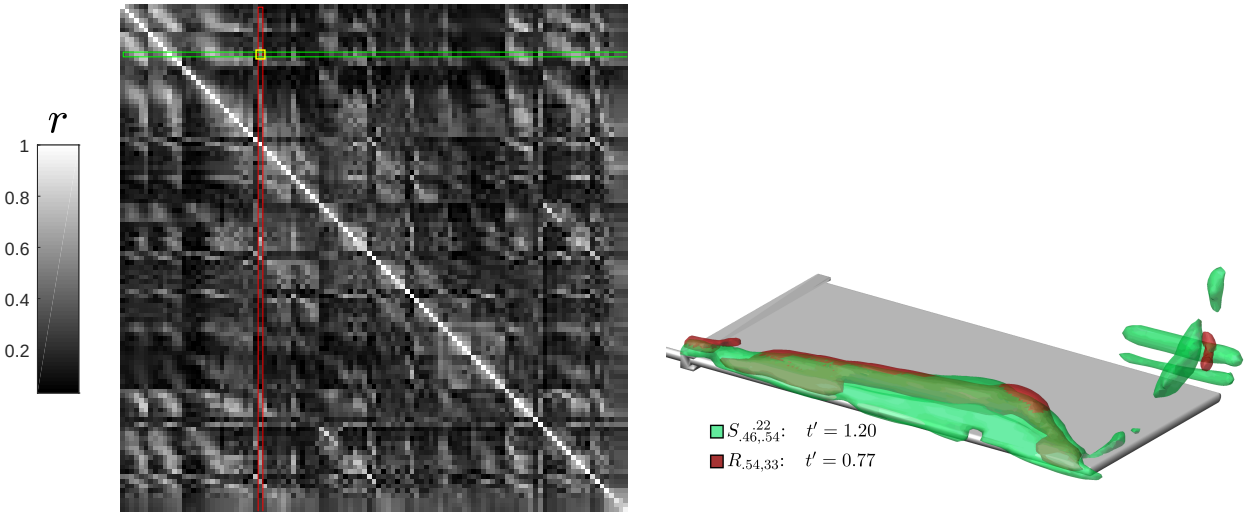

(a) (b)

Figure 5.2: (a) the complete correlation map, correlating every ensemble-averaged volume against every other volume; (b) isocontours of λ_{ci} from $S_{.46,.54}^{.22}$ and $R_{.54,33}$ overlaid, illustrating the working principle of this correlation approach

box. The intersection of this row and column is outlined as the yellow pixel, representing the correlation of between these two phases, shown visually in figure 5.2b. Here, the isocontour of λ_{ci} from $S_{.46,.54}^{.22}$ at $t' = 2.079$ is shown translucently in green and the isocontour from $R_{.54,33}$ at $t' = 0.745$ is shown translucently in red, such that the overlapping regions can be seen. Thus, the value in the yellow box can be thought of as the fraction of overlapping volume of these two isocontours over the total volume.

From this process, a correlation matrix is generated that compares every phase of every case. A visualization of this matrix is provided in figure 5.2a, which shows an image, where each pixel is colored by the by the r value of one phase of a specific case correlated with another phase of a specific case. There exists a bright diagonal of $r = 1$, representing auto-correlations. As an off diagonal example, 1 row and 1 column are boxed in green and red, respectively. The green row corresponds to the phase of $S_{.46,.54}^{.22}$ at $t' = 1.20$ and the red column to the phase of $R_{.54,33}$ at $t' = 0.77$. In figure 5.2b, two isosurfaces of normalized swirling strength are shown for each of these phases, in their respective colors, to illustrate how this correlation method works. Subsections of this correlation matrix will be investigated

and presented in the following subsections. The code used to compute these correlations and the plots is in appendix E.3.

5.2.1 Auto-correlations

To begin with the correlation based analysis, consider the auto-correlation of $P_{.5}$, shown in figure 5.3. The correlation value of each phase of $P_{.5}$ is shown using a contour plot. The t' values of each phase are shown on the axes. The reader is reminded that data points *only* exist at the intersections of the blue grid lines. The contour map fills in the area between the points through linear interpolation, which can aid in the understanding of what the correlation map is conveying. Markers are shown in black on each of the diagonals of the matrix, following conventional diagonal notation. The diagonal, d_0 is marked with circles, the superdiagonal d_1, or the set of elements above the diagonal, are marked with squares. The next 2 diagonals, d_2 and d_3 are marked with triangles and diamonds, respectively. Additionally, the subdiagonal family are marked with the same markers as the superdiagonal family. The figures in the remainder of this section will use the same visualization. From figure 5.3, an examination of the diagonal d_0 shows every value equal to one, as expected. More substantially, d_1 has some significantly high values or r, notably, the values located at (0.49,0.59) and (0.59,0.68), where $r = 0.702$ and 0.698, respectively. Thus, the phase at $t' = 0.59$ which corresponds to $\alpha_{\text{geo}} = 30°$ is a 70% match with each of its neighboring phases, indicating little change between these phases. Moreover, the correlation of the phase at $t' = 0.49$ ($\alpha_{\text{geo}} = 25°$) and $t' = 0.68$ ($\alpha_{\text{geo}} = 35°$) located on d_2 returns a less significant value of $r = 0.53$. Thus, when compared to the entire progression of phases, these 3 phases are exceptionally similar indicating that over this range of motion ($\alpha_{\text{geo}} = 25° \rightarrow \alpha_{\text{geo}} = 35°$) the vortex topology is relatively stable, resisting the convective forces of the flow. This quantitative analysis echoes the description from visual inspection of $P_{.5}$ in figure 4.1a.

In figure 5.4, the auto-correlation of $R_{.54,33}$ is shown. Here, the phase spacing is non-uniform and the dimensionless time is over 3 times greater than that of the $P_{.5}$. Despite the

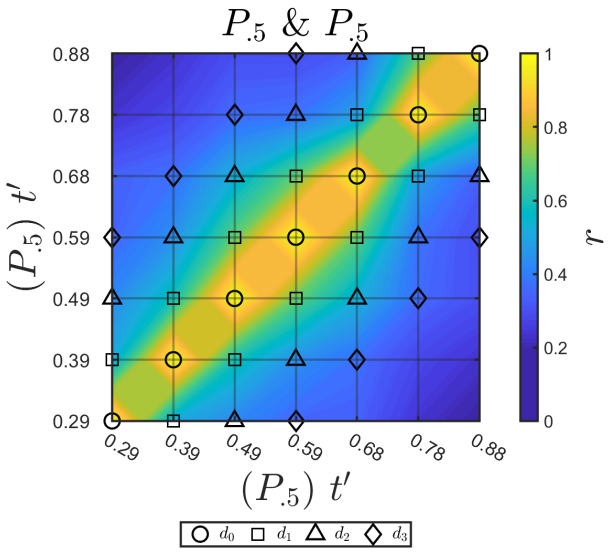

Figure 5.3: Visualization of correlation map showing the auto-correlation of $P_{.5}$, colored by r

larger phase spacing, 12 unique correlation strengths exist with greater than 0.5 correlation strength. The strongest of these correlation strengths exist in d_1 and were easily identified from the visual inspection. The first is correlation of $t' = 1.35$ and 1.68, or $\phi = 21°$ and 26°, respectively. Here $r = 0.75$. The next largest value of $r = 0.66$ is the correlation of $t' = 2.58$ and 3.16, or $\phi = 40°$ and 49°, respectively. Almost an entire convective time has passed between these two phases, yet the flow structures remains similar, possibly indicating some relative stability to the structure. A striking result is $r = 0.60$ on d_2 between $t' = 1.68$ and 2.58. However, from the visual inspection is was found that a vortex structure is being shed and another LEV forms, shown in figure 4.2a. This is an indication that there is exists some repeatability to the vortex evolution. This correlation map quantitatively adds to the a story developed from the visual inspection: the initial build up of the vortex structure followed by a shedding event with a similar process evolving in the later phases.

The auto-correlation of $S_{.46,.54}^{.22}$ is shown in figure 5.5. In this plot, d_1 contains a strong correlation strength for every element, each above $r = 0.70$, indicating that the vortex structure has little change between neighboring phases. Additionally, d_2 also contains a

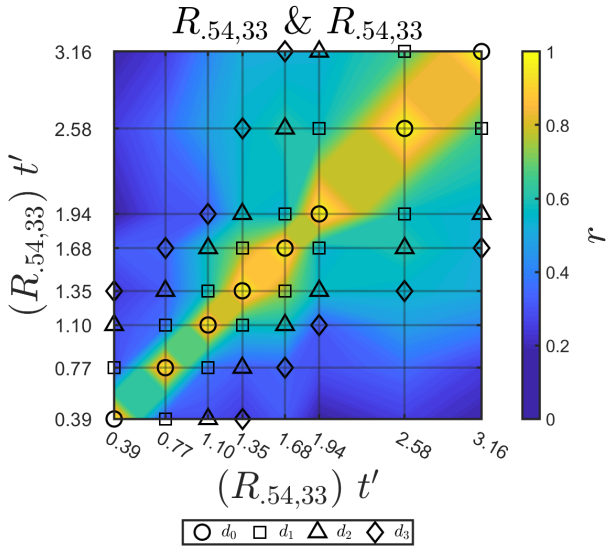

Figure 5.4: Visualization of correlation map showing the auto-correlation of $R_{.54,33}$, colored by r

strong correlation strength for every element, each above $r = 0.50$, indicating great similarity between second neighboring phases. Since d_3 has a uniform and substantial decrease correlation strength, this plot shows that overall, the vortex structure is changing on the order of $t' \sim 0.9$, which is the spacing between values correlated on d_3. Additionally, the vortex structure remains attached to the leading edge of the wing for this entire recorded motion, thus this correlation information pertains to the evolution of a single LEV, unlike the correlation plot of $R_{.54,33}$ (figure 5.4) which is correlating structures that are being shed and reformed. Again, this correlation approach has confirmed and elaborated on the visual inspection of $S_{.46,.54}^{.22}$ in figure 4.6a.

5.2.2 Cross-Correlations

Following the visual inspection, the first cross-correlation comparison is between $P_{.5}$ and $S_{.46,.54}^{.22}$, in figure 5.6. The correlation matrix appears unremarkable, with no value of correlation strength exceeding 0.5. The lack of correlation allows for the conclusion that for addition of a rolling motion completely redefines the vortex topology of the pitching motion.

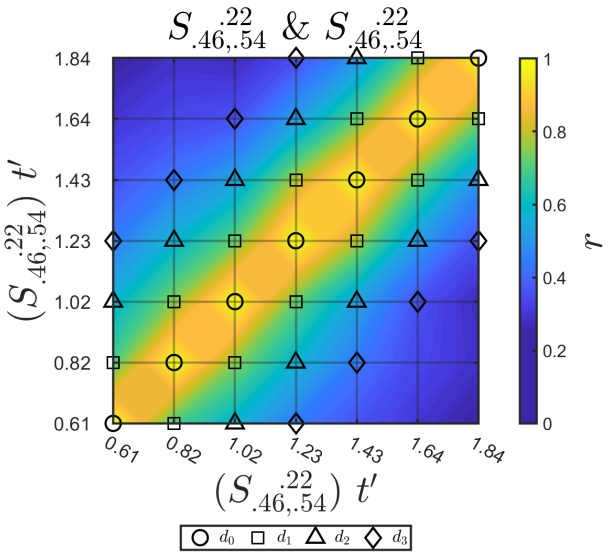

Figure 5.5: Visualization of correlation map showing the auto-correlation of $S^{22}_{.46,.54}$, colored by r

Likely, this is related to the asymmetric flow profile that the rotational forces from rolling the wing create, whereas the pitching maneuver creates a symmetric flow about that the leading edge. To aid in this comparison, plots of the wing position vs t' are shown in two plots, α_{eff} versus t' and ϕ versus t', shown in figure 5.6b and c, respectively. From both these plots it seen that the first data point of $S^{22}_{.46,.54}$ occurs at a larger normalized time than the last data point of $P_{.5}$. Additionally, the entire motion of $P_{.5}$ occurs in about 0.6 of a convective time, whereas, the $S^{22}_{.46,.54}$ takes about 2 convective times.

Returning to the quantitative analysis, the correlation matrix of $R_{.54,33}$ and $S^{22}_{.46,.54}$ is shown in figure 5.7. These cases have an intersection where both have are at $\alpha_{\text{eff}} = 33°$, which is slightly before $t' = 1.43$. Interestingly, the strongest correlation value is found right near this point, with a value of 0.75, located at (0.77,1.43). Additionally, there is a strong trend of low values of t' for $R_{.54,33}$ correlating quite well to significantly higher values of $S^{22}_{.46,.54}$. This observation translates to $R_{.54,33}$ correlating to greater values of α_{eff} and ϕ of $S^{22}_{.46,.54}$. It is noted that the range of roll angles in the data gathered for $S^{22}_{.46,.54}$ does not allow for a direct comparison of the lower roll angles of $R_{.54,33}$, yet it is unlikely that similarity

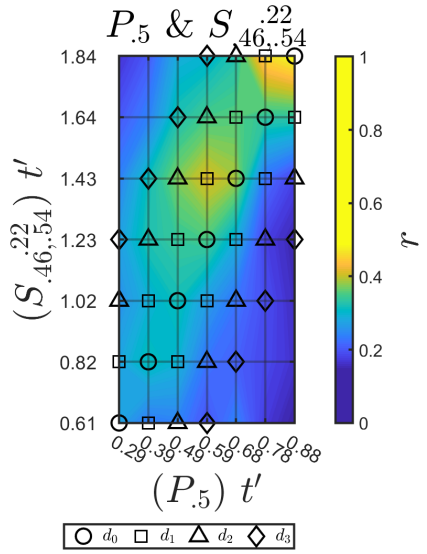

Figure 5.6: Visualization of correlation map showing the cross-correlation of $P_{.5}$ and $S^{.22}_{.46,.54}$, colored by r

would exist given the strong resemblance of the vortex structure at lower roll angles for $R_{.54,33}$ to the vortex structure at the higher end of the range of roll angles for $S^{.22}_{.46,.54}$. Again, vortex topology at similar roll angles between the two kinematic cases are unalike. Thus, the addition of the pitching motion delays the development of vortex structures in respect to three different parameters: t', α_{eff}, and ϕ.

A similar pattern is seen in the correlation matrix between $R_{.54,33}$ and $S^{.20}_{.42,.54}$, shown in figure 5.8. It was observe red in the visual inspection that the slightly slower pitch rate in $S^{.20}_{.42,.54}$ induced vortex structure that more closely resembled the topology resulting from $R_{.54,33}$. This is clearly, and quantitatively, seen here where the correlation strength is seen to be greater than the strengths in figure 5.7, where the maximums are $r = 0.68$ and 0.6, respectively.

The k_{Rg} parameter is defined such that comparison to purely pitching cases is natural. In figure 5.9, $P_{.5}$ is correlated with $S^{.20}_{.42,.54}$, such that $k = k_{Rg} = 0.2$. Despite identical parameters, there is a stark absences of similarity across all phases recorded here. There exists slightly more similarity between $P_{.5}$ and $S^{.50}_{1.05,.54}$, when $k = k_{Rg} = 0.5$, yet it is hardly

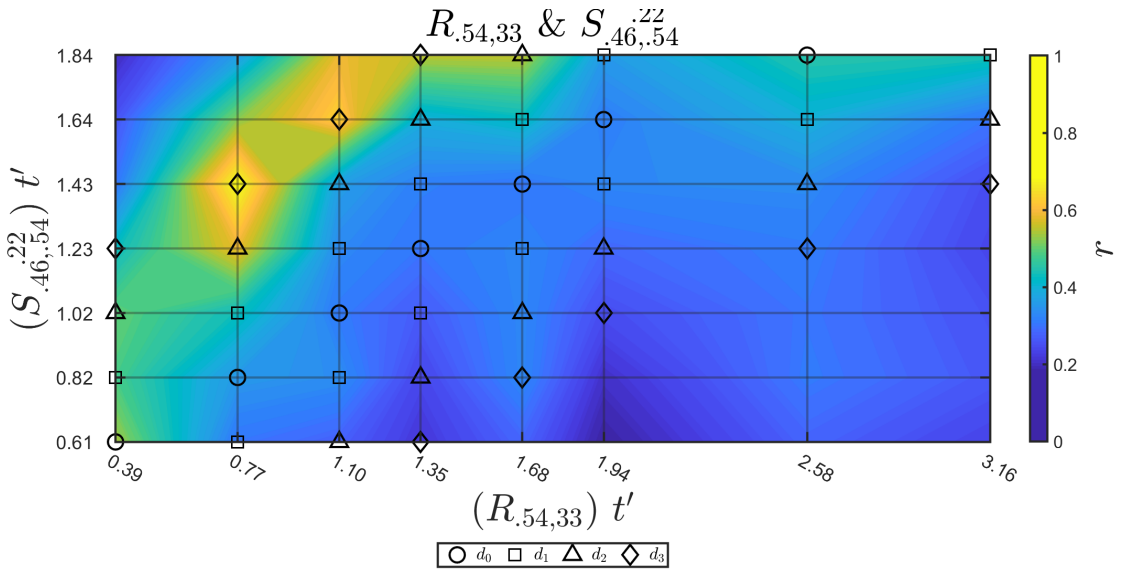

Figure 5.7: Visualization of correlation map showing the cross-correlation of $R_{.54,33}$ and $S_{.46,.54}^{.22}$, colored by r

notable. This comparison helps illustrate the that k_{Rg} parameter is more useful for comparing vortex evolution, as in the previous section. For this strict correlation based approach, the effect of the localization of the detached region from the rolling motion, significantly lowers the scores between these two cases.

To further explore the parameter space, the correlation matrix between $R_{.54,33}$ and $S_{1.05,.54}^{.50}$ is shown in figure 5.11. Here, a similar trend is seen to the correlation of $R_{.54,33}$ and $S_{.46,.54}^{.22}$, with the earlier phases of $R_{.54,33}$ correlating well for later phases of $S_{1.05,.54}^{.50}$. The irregular phase spacing of $S_{1.05,.54}^{.50}$ is due to the acquisition of two additional phases after the wing has completed the prescribed pitching motion but continues to roll at $t' = 0.98$ and 1.34. Interestingly, the two maxima of this map are at (0.77,0.98) and (0.77,1.34), the later being one of the points where the pitching motion has stopped. Despite having rolled significantly further than $R_{.54,33}$ and more t' having elapsed, the early phase of roll still matches the best with this case. This is further supporting the hypothesis that adding a pitching motion to a rolling motion delays and advances in t' the evolution of the LEV..

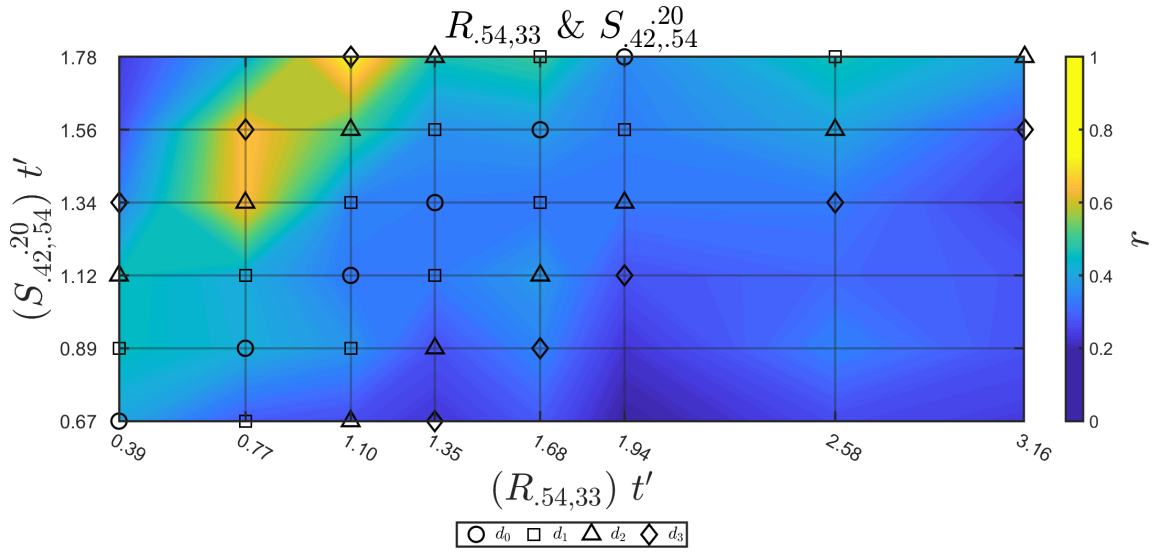

Figure 5.8: Visualization of correlation map showing the cross-correlation of $R_{.54,33}$ and $S_{.42,.54}^{.20}$, colored by r

To further investigate the effect of roll rate, $S_{.46,1.36}^{.37}$ uses the slower roll rate, matching that of $R_{1.36,33}$. The correlation matrix for these two cases are shown in figure 5.12. Here there exists only one strong correlation point at (0.29,0.75). This insipid result is the product of correlating a kinematic case that is characterized by a LEV that is consistently shed into the convecting flow, $R_{1.36,33}$, and a cylindrical, coherent LEV that stays attached until the wing stops pitching, $S_{.46,1.36}^{.37}$.

In figure 5.13, $P_{.5}$ and $S_{.46,1.36}^{.37}$ are correlated. Here, $P_{.5}$ correlates well at moderate values of t', before the LEV in the $P_{.5}$ starts arching too significantly later in the motion. Thus, while it is fair to say that the rolling motion dominates the flow structure during a simultaneous pitching and rolling maneuver, first and foremost, the pitching motion keeps the LEV attached to the LE and stable, throughout the parameter space of this dissertation.

While keeping the radius of gyration constant, it is useful to compare the various kinematic cases of simultaneous pitching and rolling to one another in order to better understand the role of pitch rate and role rate. Shown in figure 5.14, the correlation matrix of $S_{.46,.54}^{.22}$ and $S_{.42,.54}^{.20}$ shows a strong diagonal trend and, overall, closely resembles the auto-correlation of

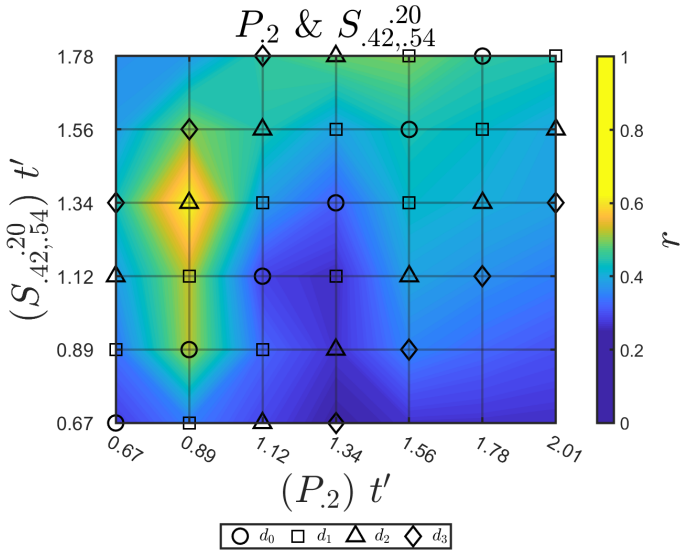

Figure 5.9: Visualization of correlation map showing the cross-correlation of $P_{.2}$ and $S^{.20}_{.42,.54}$, colored by r

$S^{.22}_{.46,.54}$. This is intuitive as the kinematics of $S^{.22}_{.46,.54}$ and $S^{.20}_{.42,.54}$ are nearly identical, with only a slight difference in pitch rate. Here the vortex structure is similar, however, the LEV of $S^{.20}_{.42,.54}$ has a defined narrow arch vortex similar to $R_{.54,33}$. Thus, the slightly slower pitch rate resulted in a more resemblance to the purely rolling counterpart. A more substantial change to the pitch rate has a more visible effect, shown in the correlation matrix between $S^{.22}_{.46,.54}$ and $S^{.50}_{1.05,.54}$, figure 5.15. Here there is still a diagonal trend, however, it is not as dominant as in figure 5.14. The later phases of each case correlate well suggesting some convergence in the developed vortex structure. The kinematic case $S^{.50}_{1.05,.54}$ has two additional phases where the wing has completed the pitching motion but has continued to roll to $\phi = 35°$ and $40°$. At $t' = 0.98$ and 1.34, respectively the overall shape of the LEV has not changed much, however, at the final phase the LEV has detached and began to convect downstream, only on the order of 10% of the chord length despite having rolled an additional 6.4°. At these phases the correlation strength has increased. A similar trend is seen for $S^{.37}_{.46,1.36}$ which continued to roll after the pitching motion was complete as well. However, $S^{.37}_{.46,1.36}$ is composed of a slower roll rate but an identical pitch rate to $S^{.22}_{.46,.54}$. Early in the phases of each, at similar

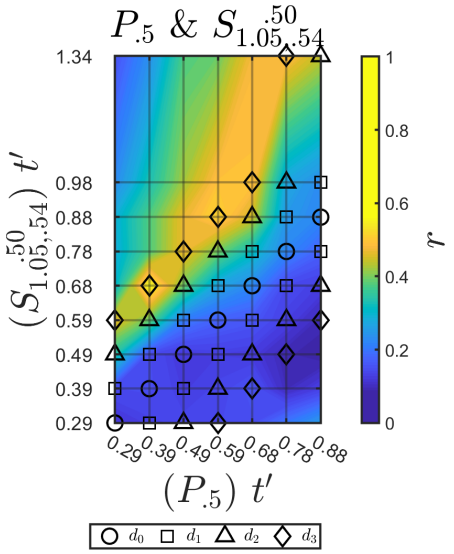

Figure 5.10: Visualization of correlation map showing the cross-correlation of $P_{.5}$ and $S_{1.05,.54}^{.50}$, colored by r

values of t', the vortex topology is similar, however, later in the motion, the LEV in $S_{.46,1.36}^{.37}$ shows significantly less growth in the x' and y' directions. As previously seen in chapter 4.1, the vortex topology of $S_{.46,1.36}^{.37}$ at $\alpha_{\text{eff}} = 35°$ and $t' = 0.88$ is even more cylindrical, resembling the LEV formed by $R_{1.36,33}$, but stays attached to the LE in when the pitching motion is added. Additionally, this LEV is slightly more towards the LE than the previous structures, as the pitching motion has not allowed the LEV to convect away up to this point in the motion. Again, when the wing stops pitching, and continues to roll for 3 phases, the LEV starts to grow and convect in the x' direction causing a spike in correlation strength, as it now lines up with the later phases of $S_{.46,.54}^{.22}$.

The final comparison is of changing the radius of gyration. Figures 5.17-5.19 shows 3 correlation matrices for identical kinematic cases, with only the radius of gyration changing between correlated pairs. As a whole, the matrices show better correlation earlier into the motion, with only the case of $S_{.46,1.36}^{.37}$ vs $s_{.46,1.36}^{.37}$ maintaining good correlation through the later phases, which is an initial indication that the vortex structure of a purely rolling wing is more sensitive to changes of radius of gyration than a simultaneous pitching and rolling

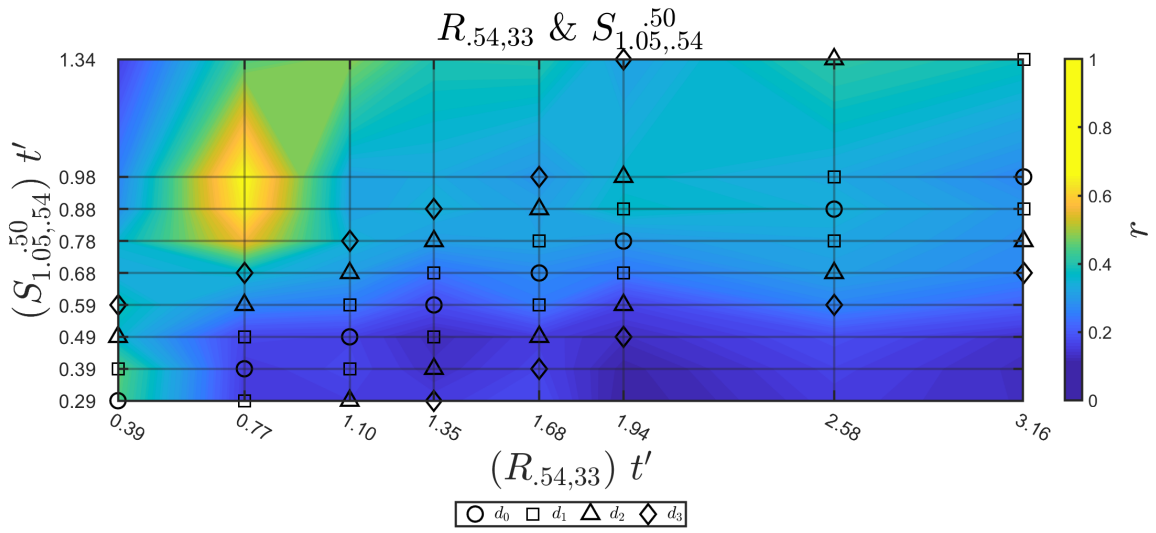

Figure 5.11: Visualization of correlation map showing the cross-correlation of $R_{.54,33}$ and $S^{.50}_{1.05,.54}$, colored by r

wing. Additionally, given the roll rate of $r_{1.36,33}$ and $s^{.37}_{.46,1.36}$ are identical, it is suggested that the vortex topology of a slower rolling wing is less sensitive to changes radius of gyration than that of a faster rolling wing.

Additional correlation matrices are presented in appendix D.

5.3 Helical Density Analysis

For comparison with Wolfinger and Rockwell [35], helical density was calculated for the present study shown in figure 5.20. Beginning with the purely rolling case, $R_{.54,33}$, figure 5.20a, shows a isocontours for λ_{ci} at $t' = 0.77$, colored by helical density. The volume has been rotated such that the LEV is viewed from the trailing edge, similar to the presentation by Wolfinger and Rockwell [35]. A banding pattern is seen here, where the midspan region of the LEV is dominated by a negative helical density, and the localized arch vortex and region near the root exhibit helical density of the opposite sign. In agreement with the observations of Wolfinger and Rockwell [35], this structure ultimately degenerated. In figure

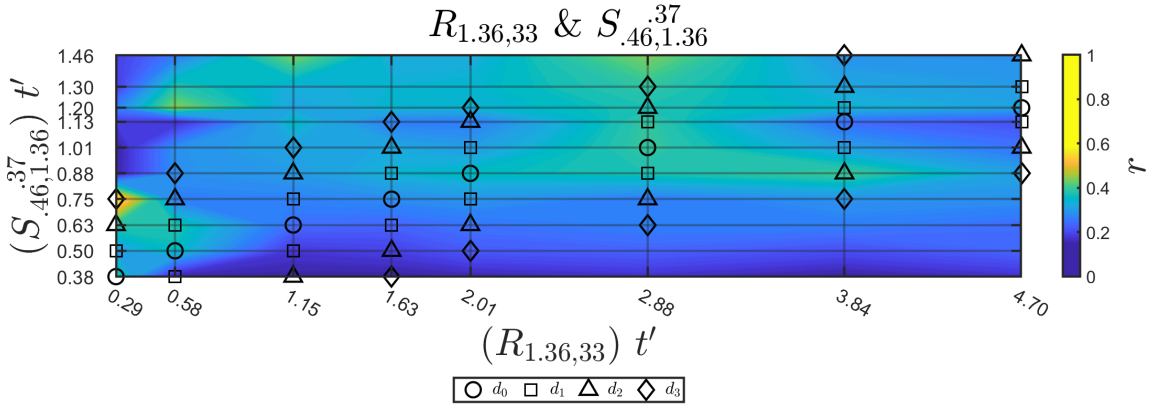

Figure 5.12: Visualization of correlation map showing the cross-correlation of $R_{1.36,33}$ and $S_{.46,1.36}^{.37}$, colored by r

5.20b, negative helical density (blue) dominates the LEV, however, where the vortex has lifted from the wing surface, opposing sign helical density is found on the bottom of the vortex. The helical density in this case is arguably more uniform than the previous for which, the LEV stays intact for the entire recorded motion here.

The simultaneous cases $S_{.46,.54}^{.22}$ and $S_{1.05,.54}^{.50}$ are shown in figures 5.20c and 5.20d, which reiterate the previous findings. The case of $S_{.46,.54}^{.22}$ exhibits similar helical density patterns to $R_{.54,33}$ foreshadowing the degradation of the vortex structure, although it is not observed in the recorded motion. The vortex structure formed by $S_{1.05,.54}^{.50}$ does appear more uniformly blue than $S_{.46,.54}^{.22}$, which may be an effect of the faster pitch rate. It has been previously noted that the addition of the pitching motion to the rolling motion helped stabilize and delay the evolution of the vortex structure. From the helical density plots presented here, it follows that the pitching motion may be helping create a more established helical LEV, characterized by a more dominant sign of helical density, thus keeping the LEV near the leading edge for a prolonged time.

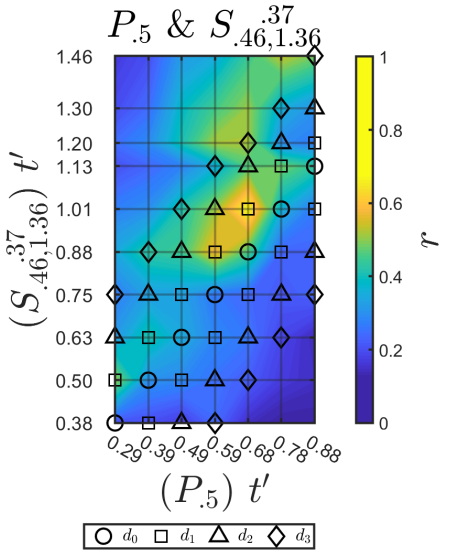

Figure 5.13: Visualization of correlation map showing the cross-correlation of $P_{.5}$ and $S^{.37}_{.46,1.36}$, colored by r

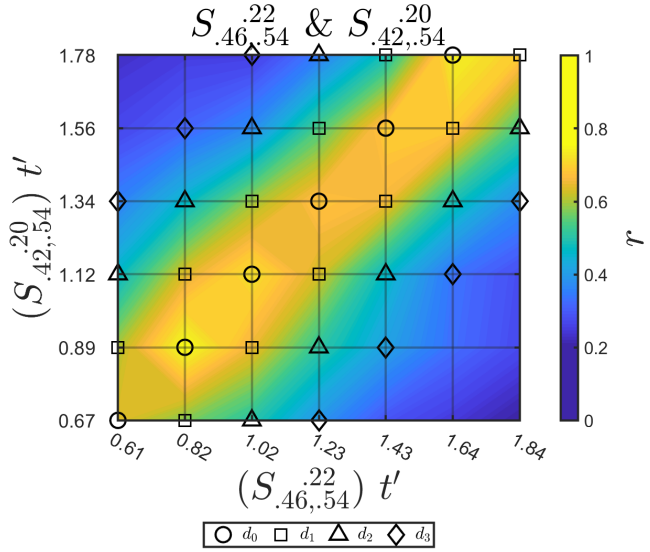

Figure 5.14: Visualization of correlation map showing the cross-correlation of $S^{.22}_{.46,.54}$ and $S^{.20}_{.42,.54}$, colored by r

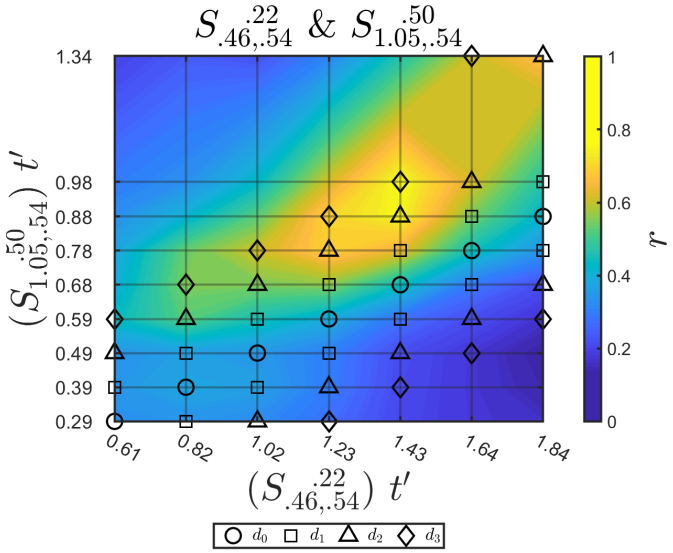

Figure 5.15: Visualization of correlation map showing the cross-correlation of $S_{.46,.54}^{.22}$ and $S_{1.05,.54}^{.50}$, colored by r

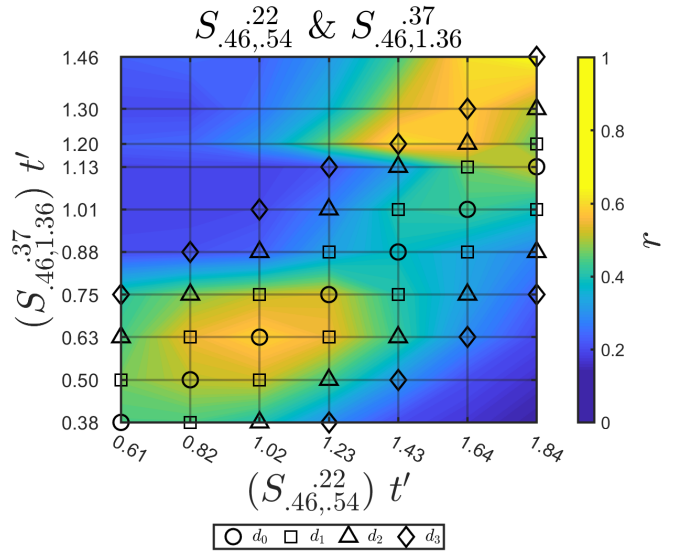

Figure 5.16: Visualization of correlation map showing the cross-correlation of $S_{.46,.54}^{.22}$ and $S_{.46,1.36}^{.37}$, colored by r

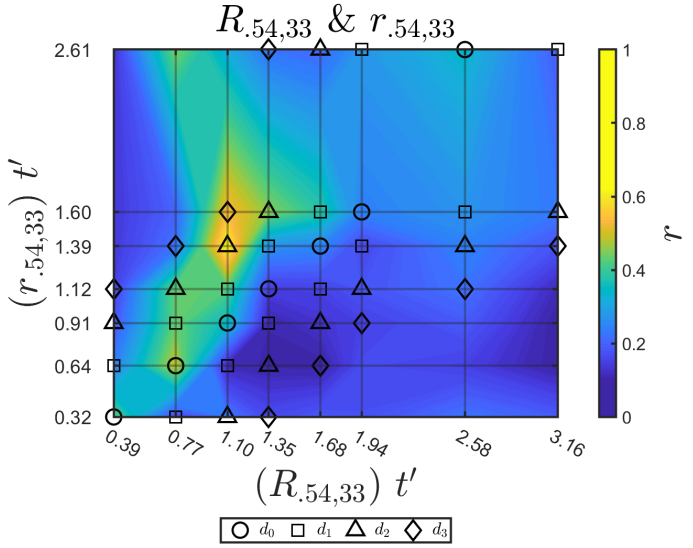

Figure 5.17: Visualization of correlation map showing the cross-correlation of $R_{.54,33}$ and $r_{.54,33}$, colored by r

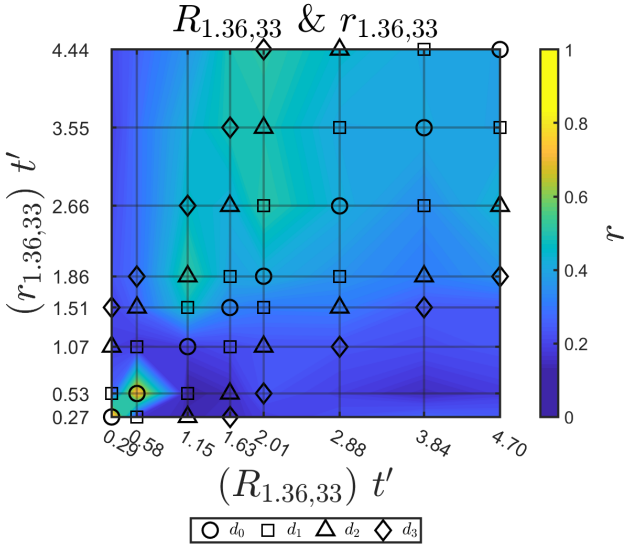

Figure 5.18: Visualization of correlation map showing the cross-correlation of $R_{1.36,33}$ and $r_{1.36,33}$, colored by r

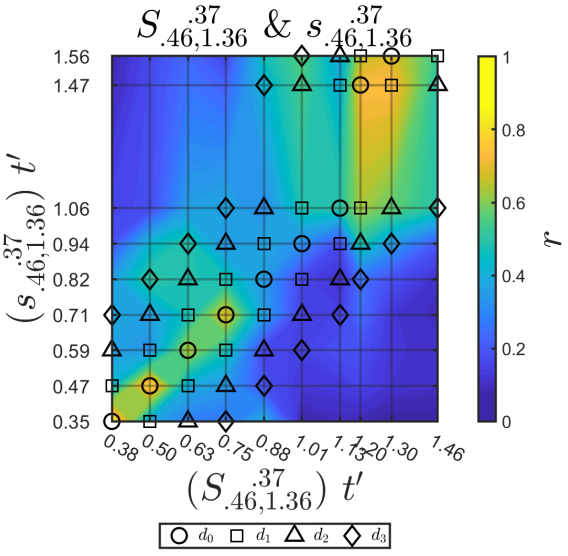

Figure 5.19: Visualization of correlation map showing the cross-correlation of $S_{.46,1.36}^{.37}$ and $s_{.46,1.36}^{.37}$, colored by r

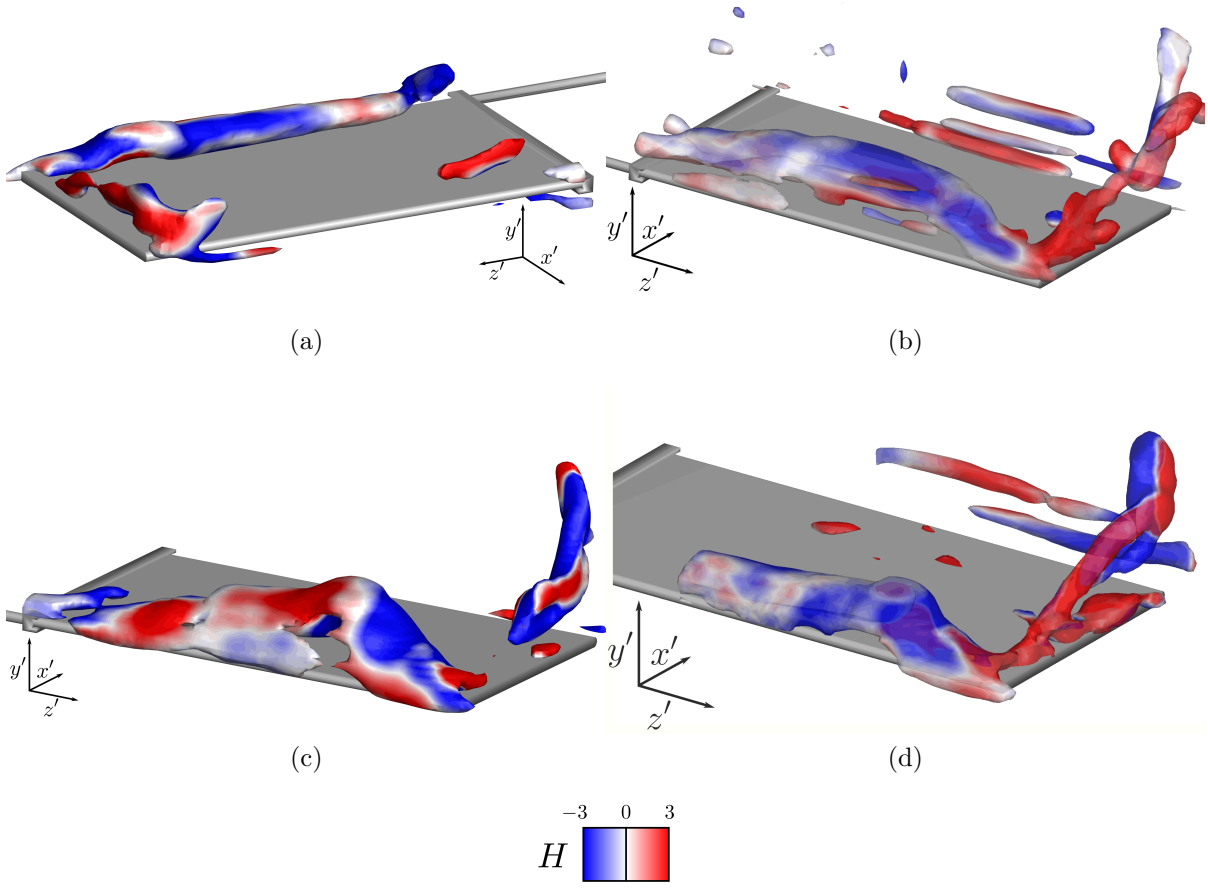

Figure 5.20: Isocontours of λ_{ci} set to 5% of the maximum value, colored by helical density H, depicting alternating signs of helical density in the LEV: (a) $R_{.54,33}$ at $t' = 0.77$ (b) $P_{.5}$ at $t' = 0.88$ (c) $S_{.46,.54}^{.22}$ at $t' = 1.84$ (d) $S_{1.05,.54}^{.50}$ at $t' = 0.88$

Chapter 6

Conclusions and Contributions

In this dissertation, the examination of vortical structures across a multi-variable parameter space revealed how variations in kinematics affect the early development of the LEV on a pitching and rolling wing, both independently and simultaneously, while subjected to a uniform flow. Vortex structures were quantitatively visualized through isocontours of swirling strength computed from 3D-3C vector fields produced from plenoptic PIV measurements, the first ever made on a maneuvering wing. Through visual inspection of the results, the evolution of the LEV was characterized into 3 stages: formation & growth, transitional, and detached. Through each stage, the topology was described. These descriptions of each case were used to understand a new proposed parameter, k_{Rg}.

The purely pitching cases formed LEVs that were initially cylindrical, then transitioned into a broad arch vortex, symmetrical about the half-span. The LEVs formed by the purely rolling kinematics also had cylindrical topologies during the formation and growth stage that evolved into asymmetric structures soon thereafter. For each value of advance ratio studied here, a dual-vortex system was formed and a correlation between the bifurcation point of this dual-vortex system and the effective angle of attack was found. Moreover, the formation of the dual-vortex system was exclusively followed by the shedding of vortical structures from the leading edge. For both the purely pitching and purely rolling kinematics, this study has presented what the author believe to be some of the most comprehensive volumetric measurements for a wing in forward flight.

The core of this dissertation was built around a simultaneously pitching and rolling wing in forward flight, for which this paper has presented 3D-3C measurements documenting the vortex topology and evolution in detail. For each of the simultaneously pitching and rolling

cases, the evolution of the LEV was less eventful than the purely pitching and purely rolling cases as the LEV consistently stayed closer to the wing surface and leading edge than the previous cases. In each case, asymmetric structures were formed that eventually led to a dual-vortex system. To aid in the understanding of the role of the wing kinematics in the formation and evolution of these structures, the k_{Rg} parameter was introduced, analogous to the reduced pitch rate k, yet utilizing the effective velocity. Through this parameter, purely pitching cases were directly compared to simultaneously pitching and rolling cases of equal k_{Rg} value. Through this matching of k_{Rg} values, it was found that the addition of a rolling motion to a pitching wing delayed the evolution of the LEV in nondimensionalized time and reduced spanwise extent of where the LEV detached from the leading edge. Furthermore, when comparing the 4 different simultaneously pitching and rolling cases, it was found that increasing k_{Rg} initiated the transition to a detached LEV sooner in nondimensionalized time and accelerated the process of detachment.

This study also linked the behavior of the LEVs to the kinematics of the wing through comparisons of vortex topology using a correlation technique. Overall, it was found that the vortex topology of a simultaneously pitching and rolling wing more closely resembled the topology of a purely rolling wing, yet the addition of a pitching motion helped to stabilize the vortex, increasing the lifetime at the LE. In addition, the vortical structures at greater t' for simultaneously pitching and rolling kinematics correlated well with the smaller values of t' for purely rolling kinematics; suggesting a time shift of the 3D evolution caused by the addition of pitching motion. This is similar to the time-shift that Granlund et al. [17] found for a purely pitching flat plate immersed in a freestream. Across the parameter space, kinematic cases of simultaneously pitching and rolling wings were less correlated with purely pitching cases using identical pitch rates. The effect of changing R_g/c was also elucidated through this approach, such that reducing the R_g/c was found to advance and the vortex evolution of the purely rolling cases, while little effect was observed in the simultaneously pitching and rolling cases. Arguably, reducing the R_g/c had the most prolific effect on the $r_{1.36,33}$ case,

which is the identical advance ratio to $s_{.46,1.36}^{37}$, that remained relatively unchanged. Thus, for this case it is concluded that the pitching motion has such a stabilizing effect that the vortex evolution remained insensitive to the change in R_g/c.

As the working principle of the dissertation, the comparison of a purely pitching wing to a simultaneously pitching and rolling wing prompted the experimental design such that, during the simultaneously pitching and rolling kinematics, the rolling motion was initiated first and allowed to stabilize. Thus, when the pitching motion was commanded, the result was a pitching wing in a rolling reference frame. It may be that the vortical structures and evolution of LEVs would be significantly different if the pitching motion was initiated first. In the context of mUAVs or aggressively maneuvering aircraft, there is likely a greater window of operable roll angles than pitch angles. The detailed insights into the flow evolution gained in this work could be leveraged to device strategies to control the aerodynamic loads, which may be critical, especially for vehicles that rely on the LEV for flight or post-stall performance.

6.1 Further Considerations and Future Work

Across the parameter space, this study noted a link between the unpinning of the LEV at the tip and the establishment of a coherent TiV. It may be that the TiV is actually causing the LEV to come unpinned or that the pinned LEV is not allowing the TiV to grow strong enough to be detected here. Thus a future study specifically on the interaction between the LEV and the TiV is suggested. This study should use higher resolution data at the LE-tip corner of the wing and perhaps explore an elliptical wing or adding a winglet. A study such as this would help shape future LEV control schemes.

Embedded in the data presented in this dissertation are 31,250 instantaneous volumetric flow fields which will further elucidate the development of the flow topology resulting from the various kinematics in the parameter space used in these experiments. The observations from the instantaneous flow fields presented agree well with the trends of the phase-averaged

flow fields, but do show notable variations. Future work on these instantaneous flow fields includes vortex tracking and a POD analysis, to explore these variations in the instantaneous flow topology and link them to possible mechanisms. Additionally, instantaneous 3D-3C measurements have never been presented on flow fields resulting from similar kinematics, of which a small preview was shown in this dissertation. The characterization of the instantaneous flow represents an intimidating, yet important task, as ultimately it is the instantaneous flow physics that any aerospace body would be subjected to. Thus, a better understanding of the instantaneous flow will yield better performing aerospace applications.

The author recognizes a clear trajectory that future work will follow. As previously mentioned, the parameter space can always be expanded and further resolved, to help concrete the hypotheses and observations shown here. However, the ultimate goal is time-resolved 3D-3C acquisition, yet, the technology to make this practical is not quite available. Provided a suitable measurement system did exist, the employment of a camera to track the rotating wing would be difficult. The author envisions a possible solution using mirrors at the pivot points to always keep the optical path of the camera down the span wing. Enabling such measurements would take much of the speculating out of the evolution of the vortex topology, which in turn would provide the best understanding of the performance of pitching and rolling wings, yielding superior applications.

Bibliography

[1] J. Zhou, R. J. Adrian, S. Balachandar, and T. M. Kendall. Mechanisms for generating coherent packets of hairpin vortices in channel flow. *Journal of Fluid Mechanics*, 387 (October):353–396, 1999. ISSN 00221120. doi: 10.1017/S002211209900467X.

[2] Marc Levoy. Light fields and computational imaging. *Computer*, 39(8):46–55, 2006. ISSN 00189162. doi: 10.1109/MC.2006.270.

[3] Diana D. Chin and David Lentink. Flapping wing aerodynamics: from insects to vertebrates. *The Journal of Experimental Biology*, 219(7):920–932, apr 2016. ISSN 0022-0949. doi: 10.1242/jeb.042317. URL `http://jeb.biologists.org/lookup/doi/10.1242/jeb.042317`.

[4] T. O. Yilmaz and D. Rockwell. Flow structure on finite-span wings due to pitch-up motion. *Journal of Fluid Mechanics*, 691(2012):518–545, 2012. ISSN 0022-1120. doi: 10.1017/jfm.2011.490.

[5] Vrishank Raghav and Narayanan Komerath. Advance ratio effects on the flow structure and unsteadiness of the dynamic-stall vortex of a rotating blade in steady forward flight. *Physics of Fluids*, 27(2), 2015. ISSN 10897666. doi: 10.1063/1.4906803.

[6] Eric Limacher, Chris Morton, and David Wood. On the trajectory of leading-edge vortices under the influence of Coriolis acceleration. *Journal of Fluid Mechanics*, 800: R1, 2016. ISSN 0022-1120. doi: 10.1017/jfm.2016.395. URL `http://www.journals.cambridge.org/abstract{_}S0022112016003955`.

[7] K. Mulleners, K. Kindler, and M. Raffel. Dynamic stall on a fully equipped helicopter model. *Aerospace Science and Technology*, 19(1):72–76, 2012. ISSN 12709638. doi: 10.1016/j.ast.2011.03.013. URL http://dx.doi.org/10.1016/j.ast.2011.03.013.

[8] David H. Bridges. Toward a theoretical description of vortex wake asymmetry. *Progress in Aerospace Sciences*, 46(2-3):62–80, 2010. ISSN 03760421. doi: 10.1016/j.paerosci.2009.11.005. URL http://dx.doi.org/10.1016/j.paerosci.2009.11.005.

[9] Hsiao Mun Lee and Yanhua Wu. A Tomo-PIV study of the effects of freestream turbulence on stall delay of the blade of a horizontal-axis wind turbine. *Wind Energy*, 17(April 2013):1185–1205, 2014. ISSN 1099-1824. doi: 10.1002/we. URL http://wileyonlinelibrary.com/doi/10.1002/we.1754.

[10] Wei Shyy, Hikaru Aono, Chang-Kwon Kang, and Hao Liu. *An Introduction to Flapping Wing Aerodynamics*. Cambridge Univeristy Press, 2013.

[11] W. Shyy, H. Aono, S. K. Chimakurthi, P. Trizila, C. K. Kang, C. E.S. Cesnik, and H. Liu. Recent progress in flapping wing aerodynamics and aeroelasticity. *Progress in Aerospace Sciences*, 46(7):284–327, 2010. ISSN 03760421. doi: 10.1016/j.paerosci.2010.01.001. URL http://dx.doi.org/10.1016/j.paerosci.2010.01.001.

[12] Z. Jane Wang. Dissecting Insect Flight. *Annual Review of Fluid Mechanics*, 37(1): 183–210, 2005. ISSN 0066-4189. doi: 10.1146/annurev.fluid.36.050802.121940. URL http://www.annualreviews.org/doi/10.1146/annurev.fluid.36.050802.121940.

[13] Fritz Olaf Lehmann. The mechanisms of lift enhancement in insect flight. *Naturwissenschaften*, 91(3):101–122, 2004. ISSN 00281042. doi: 10.1007/s00114-004-0502-3.

[14] Sanjay P Sane. The aerodynamics of insect flight. *The Journal of experimental biology*, 206(Pt 23):4191–4208, 2003. ISSN 0022-0949. doi: 10.1242/jeb.00663.

[15] Vrishank Raghav and Narayanan Komerath. An Exploration of Radial Flow on a Rotating Blade in Retreating Blade Stall. *Journal of the American Helicopter Society*, 58(2):1–10, 2013. ISSN 21616027. doi: 10.4050/jahs.58.022005. URL http://www.ingentaconnect.com/content/ahs/jahs/2013/00000058/00000002/art00005{%}255Cnhttp://dx.doi.org/10.4050/JAHS.58.022005.

[16] Michael H. Dickinson and Karl Götz. Unsteady aerodynamic performance of model wings at low reynolds numbers. *J. exp. Biol.*, 174:45–64, 1993. ISSN 0022-0949. doi: 10.1242/jeb.00739.

[17] Kenneth O Granlund, Michael V Ol, and Luis P Bernal. Unsteady pitching flat plates. 733(2013):1–13, 2013. doi: 10.1017/jfm.2013.444.

[18] Colin Hartloper and David Rival. Vortex development on pitching plates with lunate and truncate planforms. *Jfm*, 732(2013):332–344, 2013. ISSN 0022-1120. doi: 10.1017/jfm.2013.400.

[19] Kyle Hord and Yongsheng Lian. Leading Edge Vortex Circulation Development on Finite Aspect Ratio Pitch-Up Wings. *AIAA Journal*, 54(9):1–13, 2016. ISSN 0001-1452. doi: 10.2514/1.J053911. URL http://arc.aiaa.org/doi/10.2514/1.J053911.

[20] Ryan T. Jantzen, Kunihiko Taira, Kenneth O. Granlund, and Michael V. Ol. Vortex dynamics around pitching plates. *Physics of Fluids*, 26(5), 2014. ISSN 10897666. doi: 10.1063/1.4879035.

[21] Mathieu Olivier and Guy Dumas. A parametric investigation of the propulsion of 2D chordwise-flexible flapping wings at low Reynolds number using numerical simulations. *Journal of Fluids and Structures*, 63:210–237, 2016. ISSN 10958622. doi: 10.1016/j.jfluidstructs.2016.03.010. URL http://dx.doi.org/10.1016/j.jfluidstructs.2016.03.010.

[22] D T Polet, D E Rival, and G D Weymouth. Unsteady dynamics of rapid perching manoeuvres. *Journal of Fluid Mechanics*, 767(2014):323–341, 2015. ISSN 0022-1120. doi: DOI10.1017/jfm.2015.61.

[23] Kiran Ramesh, Ashok Gopalarathnam, and Kenneth Granlund. Discrete-vortex method with novel shedding criterion for unsteady aerofoil flows with intermittent leading-edge vortex shedding. *Journal of Fluid Mechanics*, 751:500–538, 2014. doi: 10.1017/jfm.2014.297.

[24] P. R. R. J. Stevens and H. Babinsky. Experiments to investigate lift production mechanisms on pitching flat plates. *Experiments in Fluids*, 58(1):7, 2017. ISSN 0723-4864. doi: 10.1007/s00348-016-2290-x. URL `http://link.springer.com/10.1007/s00348-016-2290-x`.

[25] Miguel R Visbal. Analysis of the Onset of Dynamic Stall Using High-Fidelity Large-Eddy Simulations. (January):1–25, 2014. URL `Visbal2014a`.

[26] Miguel R Visbal. Numerical Exploration of Flow Control for Delay of Dynamic Stall on a Pitching Airfoil. (June):1–28, 2014.

[27] T. Yilmaz, M. Ol, and D. Rockwell. Scaling of flow separation on a pitching low aspect ratio plate. *Journal of Fluids and Structures*, 26(6):1034–1041, 2010. ISSN 08899746. doi: 10.1016/j.jfluidstructs.2010.07.003.

[28] Craig James Wojcik and James H.J. Buchholz. Parameter Variation and the Leading-Edge Vortex of a Rotating Flat Plate. *AIAA Journal*, 52(2):348–357, 2014.

[29] C. A. Ozen and D. Rockwell. Vortical structures on a flapping wing. *Experiments in Fluids*, 50(1):23–34, 2011. ISSN 07234864. doi: 10.1007/s00348-010-0888-y.

[30] M. Bross, C. A. Ozen, and D. Rockwell. Flow structure on a rotating wing: Effect of steady incident flow. *Physics of Fluids*, 25(8), 2013. ISSN 10706631. doi: 10.1063/1.4816632.

[31] James M Birch and Michael H Dickinson. Spanwise flow and the attachment of the leading-edge vortex on insect wings. 412(August):0–4, 2001.

[32] H. Aono, F. Liang, and H. Liu. Near- and far-field aerodynamics in insect hovering flight: an integrated computational study. *Journal of Experimental Biology*, 211(2):239–257, 2008. ISSN 0022-0949. doi: 10.1242/jeb.008649. URL `http://jeb.biologists.org/cgi/doi/10.1242/jeb.008649`.

[33] Jeff D. Eldredge and Anya R. Jones. Leading-Edge Vortices: Mechanics and Modeling. *Annual Review of Fluid Mechanics*, 51(1):annurev–fluid–010518–040334, 2019. ISSN 0066-4189. doi: 10.1146/annurev-fluid-010518-040334. URL `https://www.annualreviews.org/doi/10.1146/annurev-fluid-010518-040334`.

[34] Daniel J. Garmann, Miguel R. Visbal, and Paul D. Orkwis. Three-dimensional flow structure and aerodynamic loading on a revolving wing. *Physics of Fluids*, 25(3), 2013. ISSN 10706631. doi: 10.1063/1.4794753.

[35] Maxwell Wolfinger and Donald Rockwell. Transformation of flow structure on a rotating wing due to variation of radius of gyration. *Experiments in Fluids*, 56(7), 2015. ISSN 07234864. doi: 10.1007/s00348-015-2005-8.

[36] Felipe Bohorquez. *Rotor Hover Performance and System design of an Efficient Coaxial Rotary Wing Micro Air Vehicle*. PhD thesis, 2007.

[37] Miguel R Visbal and J S Shang. Investigation of the flow structure around a rapidly pitching airfoil. *AIAA Journal*, 27(8):1044–1051, aug 1989. ISSN 0001-1452. doi: 10.2514/3.10219. URL `https://doi.org/10.2514/3.10219`.

[38] Daniel J. Garmann and Miguel R. Visbal. Numerical investigation of transitional flow over a rapidly pitching plate. *Physics of Fluids*, 23(9), 2011. ISSN 10706631. doi: 10.1063/1.3626407.

[39] G. C. Lewin and H. Haj-Hariri. Modelling thrust generation of a two-dimensional heaving airfoil in a viscous flow. *Journal of Fluid Mechanics*, 492(492):339–362, 2003. ISSN 00221120. doi: 10.1017/S0022112003005743.

[40] Azar Eslam Panah, James M. Akkala, and James H.J. Buchholz. Vorticity transport and the leading-edge vortex of a plunging airfoil. *Experiments in Fluids*, 56(8):1–15, 2015. ISSN 07234864. doi: 10.1007/s00348-015-2014-7.

[41] K. B. Lua, T. T. Lim, and K. S. Yeo. Wake-Structure Formation of a Heaving Two-Dimensional Elliptic Airfoil. *AIAA Journal*, 45(7):1571–1583, 2007.

[42] James M. Akkala and James H.J. Buchholz. Vorticity transport mechanisms governing the development of leading-edge vortices. *Journal of Fluid Mechanics*, 829:512–537, 2017. ISSN 14697645. doi: 10.1017/jfm.2017.559.

[43] I. Calderon, D.E.; Wang, Z.; Gursul. Lift Enhanement of a Rectangular Wing Undergoing a Small Amplitude Plunging Motion. *48th AIAA Aerospace Sciences Meeting*, (January):2010, 2010. doi: 10.2514/6.2010-386.

[44] D. E. Calderon, Z. Wang, I. Gursul, and M. R. Visbal. Volumetric measurements and simulations of the vortex structures generated by low aspect ratio plunging wings. *Physics of Fluids*, 25(6), 2013. ISSN 10706631. doi: 10.1063/1.4808440.

[45] Yeon Sik Baik, Luis P. Bernal, Kenneth Granlund, and Michael V. Ol. Unsteady force generation and vortex dynamics of pitching and plunging aerofoils. *Journal of Fluid Mechanics*, 709:37–68, 2012. ISSN 00221120. doi: 10.1017/jfm.2012.318.

[46] David Lentink and Michael H Dickinson. Biofluiddynamic scaling of flapping , spinning and translating fins and wings. *The Journal of Experimental Biology*, pages 2691–2704, 2009. doi: 10.1242/jeb.022251.

[47] David Lentink and Michael H Dickinson. Rotational accelerations stabilize leading edge vortices on revolving fly wings. *The Journal of Experimental Biology*, pages 2705–2719, 2009. doi: 10.1242/jeb.022269.

[48] Craig J. Wojcik and James H. J. Buchholz. Vorticity transport in the leading-edge vortex on a rotating blade. *Journal of Fluid Mechanics*, 743(2014):249–261, 2014. ISSN 0022-1120. doi: 10.1017/jfm.2014.18. URL `http://www.journals.cambridge.org/abstract{_}S0022112014000184`.

[49] Anya R. Jones, Albert Medina, Hannah Spooner, and Karen Mulleners. Characterizing a burst leading-edge vortex on a rotating flat plate wing. *Experiments in Fluids*, 57(4): 1–16, 2016. ISSN 07234864. doi: 10.1007/s00348-016-2143-7.

[50] Albert Medina and Anya R. Jones. Leading-edge vortex burst on a low-aspect-ratio rotating flat plate. *Physical Review Fluids*, 1(4):044501, 2016. ISSN 2469-990X. doi: 10.1103/PhysRevFluids.1.044501. URL `https://link.aps.org/doi/10.1103/PhysRevFluids.1.044501`.

[51] D. J. Garmann and M. R. Visbal. Dynamics of revolving wings for various aspect ratios. *Journal of Fluid Mechanics*, 748(2014):932–956, 2014. ISSN 0022-1120. doi: 10.1017/jfm.2014.212. URL `http://www.journals.cambridge.org/abstract{_}S0022112014002122`.

[52] C. A. Ozen and D. Rockwell. Flow structure on a rotating plate. *Experiments in Fluids*, 52(1):207–223, 2012. ISSN 07234864. doi: 10.1007/s00348-011-1215-y.

[53] Charles P. Ellington, Coen van den Berg, Alexander P. Willmott, and Adrian L. R. Thomas. Leading-edge vortices in insect flight. *Nature*, 384(6610):626–630, 1996. ISSN

0028-0836. doi: 10.1038/384626a0. URL http://www.nature.com/doifinder/10.1038/384626a0.

[54] James R Usherwood and Charles P Ellington. The aerodynamics of revolving wings I. Model hawkmoth wings. *The Journal of experimental biology*, 205(Pt 11):1547–1564, 2002. ISSN 0022-0949.

[55] James M Birch, William B Dickson, and Michael H Dickinson. Force production and flow structure of the leading edge vortex on flapping wings at high and low Reynolds numbers. pages 1063–1072, 2004. doi: 10.1242/jeb.00848.

[56] Zakery R. Carr, Adam C. DeVoria, and Matthew J. Ringuette. Aspect-ratio effects on rotating wings: circulation and forces. *Journal of Fluid Mechanics*, 767, 2015. ISSN 0022-1120. doi: 10.1017/jfm.2015.44.

[57] R. R. Harbig, J. Sheridan, and M. C. Thompson. Reynolds number and aspect ratio effects on the leading-edge vortex for rotating insect wing planforms. *Journal of Fluid Mechanics*, 730:52–75, 2013. ISSN 0022-1120. doi: 10.1017/jfm.2013.335. URL http://journals.cambridge.org/abstract{_}S0022112013003352{%}5Cnhttp://www.journals.cambridge.org/abstract{_}S0022112013003352.

[58] C. Van den Berg and C. P. Ellington. The three-dimensional leading-edge vortex of a 'hovering' model hawkmoth. *Philosophical Transactions of the Royal Society B: Biological Sciences*, 352(1351):329–340, 1997. ISSN 0962-8436. doi: 10.1098/rstb.1997.0024. URL http://rstb.royalsocietypublishing.org/cgi/doi/10.1098/rstb.1997.0024.

[59] Mao Sun and Jian Tang. Unsteady aerodynamic force generation by a model fruit fly wing in flapping motion. *The Journal of experimental biology*, 205(Pt 1):55–70, 2002. ISSN 0022-0949.

[60] Nathan Phillips, Kevin Knowles, and Richard J Bomphrey. The effect of aspect ratio on the leading-edge vortex over an insect-like flapping wing. *Bioinspiration & Biomimetics*, 10(5):056020, 2015. ISSN 1748-3190. doi: 10.1088/1748-3190/10/5/056020. URL http://stacks.iop.org/1748-3190/10/i=5/a=056020?key=crossref.670af6abfcf482b0fa381358fa14e798.

[61] Iman Borazjani and Mohsen Daghooghi. The fish tail motion forms an attached leading edge vortex. *Proceedings. Biological sciences / The Royal Society*, 280, 2013. ISSN 1471-2954. doi: 10.1098/rspb.2012.2071.

[62] James R. Usherwood. The aerodynamic forces and pressure distribution of a revolving pigeon wing. *Animal Locomotion*, pages 429–441, 2010. ISSN 07234864. doi: 10.1007/978-3-642-11633-9_33.

[63] Adrian L R Thomas, Graham K Taylor, Robert B Srygley, Robert L Nudds, and Richard J Bomphrey. Dragonfly flight : free-flight and tethered flow visualizations reveal a diverse array of unsteady lift-generating mechanisms , controlled primarily via angle of attack. pages 4299–4323, 2004. doi: 10.1242/jeb.01262.

[64] Edward H. Adelson and James R. Bergen. The plenoptic function and the elements of early vision. *Computational models of visual ...*, pages 3–20, 1991. ISSN 03741338.

[65] Ren Ng. *Digital light field photography.* Doctorate, Standford University, 2006. URL https://www.lytro.com/renng-thesis.pdf{%}5Cnhttp://testcis.cis.rit.edu/{~}cnspci/references/dip/light{_}field{_}photography/ng2006.pdf.

[66] Timothy W Fahringer, Kyle P Lynch, and Brian S Thurow. Volumetric particle image velocimetry with a single plenoptic camera. *Measurement Science and Technology*, 26(11):1–25, 2015. ISSN 0957-0233. doi: 10.1088/0957-0233/26/11/115201. URL http://stacks.iop.org/0957-0233/26/i=11/a=115201?key=crossref.324b3a85fc9196137efd1fa4ec233b89.

[67] Jeffrey Bolan, Elise Hall, Chris Clifford, and Brian Thurow. Light-Field Imaging Toolkit. *SoftwareX*, 5:101–106, 2015. ISSN 23527110. doi: 10.1016/j.softx.2016.05.004.

[68] Elise M. Hall, Timothy W. Fahringer, Brian S. Thurow, and Daniel R. Guildenbecher. Volumetric calibration of a plenoptic camera. *55th AIAA Aerospace Sciences Meeting*, (January):1–14, 2017. doi: 10.2514/6.2017-1642. URL `http://arc.aiaa.org/doi/10.2514/6.2017-1642`.

[69] Shengxian Shi, Junfei Ding, T. H. New, and Julio Soria. Light-field camera-based 3D volumetric particle image velocimetry with dense ray tracing reconstruction technique. *Experiments in Fluids*, 58(7):1–16, 2017. ISSN 07234864. doi: 10.1007/s00348-017-2365-3.

[70] Brian E Rice, J Adam Mckenzie, Scott J Peltier, Christopher S Combs, Christopher Clifford, and Brian Thurow. Comparison of 4-camera Tomographic PIV and Single-camera Plenoptic PIV. (January):1–11, 2018. doi: 10.2514/6.2018-2036.

[71] Shengxian Shi, Junfei Ding, Callum Atkinson, Julio Soria, and T. H. New. A detailed comparison of single-camera light-field PIV and tomographic PIV. *Experiments in Fluids*, 59(3):46, 2018. ISSN 0723-4864. doi: 10.1007/s00348-018-2500-9. URL `http://link.springer.com/10.1007/s00348-018-2500-9`.

[72] Kyle C K.C. Johnson, Brian S B.S. Thurow, Taehoon Kim, Gianluca Blois, K.T. Christensen, and Kenneth T Christiansen. Volumetric velocity measurements in the wake of a hemispherical roughness element. *AIAA Journal*, July(7):1–16, 2017. ISSN 0001-1452. doi: 10.2514/1.J055454.

[73] Jeff Eldredge and Chengjie Wang. High-Fidelity Simulations and Low-Order Modeling of a Rapidly Pitching Plate. *40th Fluid Dynamics Conference and Exhibit*, (June 2010), 2010. doi: 10.2514/6.2010-4281. URL `http://arc.aiaa.org/doi/10.2514/6.2010-4281`.

[74] M. A. Mendez, M. Raiola, A. Masullo, S. Discetti, A. Ianiro, R. Theunissen, and J. M. Buchlin. POD-based background removal for particle image velocimetry. *Experimental Thermal and Fluid Science*, 80:181–192, 2017. ISSN 08941777. doi: 10.1016/j.expthermflusci.2016.08.021. URL `http://dx.doi.org/10.1016/j.expthermflusci.2016.08.021`.

[75] Kyle Lynch. *Advances in time - resolved tomographic particle image velocimetry*. Phd, TU Delft, 2015.

[76] Fulvio Scarano and Christian Poelma. Three-dimensional vorticity patterns of cylinder wakes. *Experiments in Fluids*, 47(1):69–83, 2009. ISSN 07234864. doi: 10.1007/s00348-009-0629-2.

[77] Vivianne Holm. Methods for Vortex Identification. 2012.

[78] H K Moffatt and A Tsinober. Helicity in Laminar and Turbulent Flow. *Annual Review of Fluid Mechanics*, 1992. ISSN 0066-4189. doi: 10.1146/annurev.fl.24.010192.001433.

[79] Ronald Adrian and Jerry Westerweel. *Particle Image Velocimetry*. Cambridge Univeristy Press, 2011.

[80] I. Gursul, R. Gordnier, and M. Visbal. Unsteady aerodynamics of nonslender delta wings. *Progress in Aerospace Sciences*, 41(7):515–557, 2005. ISSN 03760421. doi: 10.1016/j.paerosci.2005.09.002.

[81] David P. Stern and Mauricio Peredo. Thoughts on Ray Vibrations, 2010. URL `http://www-spof.gsfc.nasa.gov/Education/wfarad1846.html`.

[82] G Lippmann. Epreuves reversibles donnant la sensation du relief. *J. Phys. Theor. Appl.*, pages 921–925, 1908.

[83] Kyle Lynch, T Fahringer, and B Thurow. Three-Dimensional Particle Image Velocimetry Using a Plenoptic Camera. *50th AIAA Aero Sciences Meeting including the New Horizons Forum and Aerospace Exposition*, (January):1–14, 2012. doi: 10.2514/6.2012-1056. URL `http://arc.aiaa.org/doi/pdf/10.2514/6.2012-1056`.

[84] John L. Lumley. The structure of imhogeneous turbulence. *Atmospheric Turbulence and Wave Propogation*, pages 166–178, 1967.

[85] A. A. Townsend. *The Structure of Turbulent Shear Flow*. Cambridge Univeristy Press, Cambridge, 2nd edition, 1956. ISBN 0 521 20710.

[86] Steven J. Leon. *Linear Algebra with Applications*. Pearson Learning Solutions, eighth edition, 2010.

[87] John David Logan. *Applied Mathematics*. John Wiley & Sons, Inc., third edition, 2006. ISBN 9789462390089. doi: 10.1090/S0002-9904-1950-09444-0.

[88] Lindsay I Smith. A tutorial on Principal Components Analysis Introduction. *Statistics*, 51:52, 2002. ISSN 03610926. doi: 10.1080/03610928808829796. URL `http://www.mendeley.com/research/computational-genome-analysis-an-introduction-statistics-for-biology-and-health/`.

[89] Anindya (Penn State University) Chatterjee. An introduction to the proper orthogonal decomposition. *Computational Science Section Tutorial*, 2000.

[90] Holger Nobach, Cameron Tropea, Laurent Cordier, Jean-Paul Bonnet, Joël Delville, Jacques Lewalle, Marie Farge, Kai Schneider, and Ronald Adrian. Proper Orthogonal Decomposition: POD. In Cameron Tropea, John Foss, and Alexander Yarin, editors, *Springer Handbook of Experimental Fluid Mechanics*, chapter 22.4, pages 1346–1370. Springer, 2007. ISBN 978-3-540-25141-5.

[91] Philip Holmes, John L. Lumley, and Gal Berkooz. *Turbulence, Coherent Structures, Dynamical Systems and Symmetry*. Cambridge Univeristy Press, 1998.

[92] Lawrence Sirovich. Turbulence and the dynamics of coherent structures part i: coherent structures*. *Quarterly of Applied Mathematics*, XLV(3):561–571, 1987. ISSN 0033-569X.

Appendix A

Movie References

Movies are hosted here: `https://auburn.box.com/s/16cwl2jp3214wm9ecbuljatghcbv20k1`

Movie 1: Phase-averaged results from $P_{.5}$, shown with isocontours of normalized swirling strength and stream ribbons of normalized chordwise velocity

Movie 2: Phase-averaged results from $P_{.2}$, shown with isocontours of normalized swirling strength and stream ribbons of normalized chordwise velocity

Movie 3: Phase-averaged results from $R_{.54,33}$, shown with isocontours of normalized swirling strength and stream ribbons of normalized chordwise velocity

Movie 4: Phase-averaged results from $R_{1.36,33}$, shown with isocontours of normalized swirling strength and stream ribbons of normalized chordwise velocity

Movie 5: Phase-averaged results from $R_{.54,23}$, shown with isocontours of normalized swirling strength and stream ribbons of normalized chordwise velocity

Movie 6: Phase-averaged results from $R_{.54,43}$, shown with isocontours of normalized swirling strength and stream ribbons of normalized chordwise velocity

Movie 7: Phase-averaged results from $R_{1.36,43}$, shown with isocontours of normalized swirling strength and stream ribbons of normalized chordwise velocity

Movie 8: Phase-averaged results from $r_{.54,33}$, shown with isocontours of normalized swirling strength and stream ribbons of normalized chordwise velocity

Movie 9: Phase-averaged results from $r_{1.36,33}$, shown with isocontours of normalized swirling strength and stream ribbons of normalized chordwise velocity

Movie 10: Phase-averaged results from $S_{.46,.54}^{.22}$, shown with isocontours of normalized swirling strength and stream ribbons of normalized chordwise velocity

Movie 11: Phase-averaged results from $S_{.42,.54}^{.20}$, shown with isocontours of normalized swirling strength and stream ribbons of normalized chordwise velocity

Movie 12: Phase-averaged results from $S_{1.05,.54}^{.50}$, shown with isocontours of normalized swirling strength and stream ribbons of normalized chordwise velocity

Movie 13: Phase-averaged results from $S_{.46,1.36}^{.37}$, shown with isocontours of normalized swirling strength and stream ribbons of normalized chordwise velocity

Movie 14: Phase-averaged results from $s_{.46,1.36}^{.37}$, shown with isocontours of normalized swirling strength and stream ribbons of normalized chordwise velocity

Appendix B

Plenoptic Camera Design and Realization

Before understanding a plenoptic camera, it is important to understand what it is capturing: the light field. Levoy formally defines the light field, or photic field as "radiance along rays in empty space" [2]. It serves well to closely examine this definition.

First, consider the phrase *light field*. It is natural to think that light flows through an environment, but Michael Faraday first suggested that light should be interpreted as a field, in a lecture titled *Thoughts on Ray Vibrations*, summarized in a letter which NASA hosts online [81]. By treating light as a field, Adelson and Bergen [64], set out to mathematically describe this field. Citing Leonardo da Vinci for their inspiration, Adelson and Bergen [64] begin by asking what can potentially be seen by an observer. The answer is defined as the plenoptic function. Adelson and Bergen [64] consider the plenoptic function to be a complete holographic representation of the visual world, allowing for reconstruction of every possible view, at every moment, from every position, and at every wavelength. Thus, the plenoptic function P is expressed as

$$P = P(\theta, \phi, \lambda, t, V_x, V_y, V_z) \tag{B.1}$$

where *theta* and *phi* represent the spherical coordinates of light seen from a viewpoint, λ is the wavelength of the light seen from a viewpoint, t is the time that the light is seen from a viewpoint, and V_x, V_y, and V_z are the Cartesian coordinates of a viewpoint. Thus, the plenoptic function is a seven dimensional (7D) function.

Next, consider the definition of *radiance*: the amount of light traveling along a ray. Radiance is denoted by L and has units of watts per steradian per square meter ($W \cdot sr^{-1} \cdot m^{-2}$). By considering the plenoptic function for radiance and a single instant in time, the plenoptic function is averaged over the wavelengths and reduced to the five dimensional (5D)

function given by

$$L = L(x, y, z, \theta, \phi) \ . \tag{B.2}$$

Levoy [2] notes that, if nothing is blocking the ray, the radiance along the ray remains constant. This leads to a redundancy of the 5D plenoptic function. The plenoptic function can be reduced to a four dimensional (4D) function using two-plane parameterization, shown below in figure B.1.

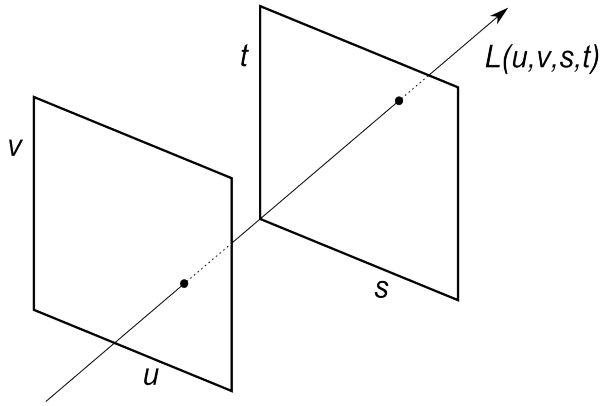

Figure B.1: Two plane parametrization of the plenoptic function for radiance adapted from Levoy [2]

Many different methods have been proposed to record the light field. Perhaps the simplest to imagine is moving a camera all around a scene, to capture many different views. For this application to work, the scene would have to remain completely stationary, as a technician moved the camera around to gather many different views. A logical improvement to this technique is to use multiple cameras, so that many different views can be captured at the same time. Photographers and cinematographers will use arrays of cameras to capture many different views of a scene at an instant in time, so that the scene does not have to be stationary. These camera arrays can quickly grow very large, requiring many cameras, which is both expensive and difficult to operate. If the range of viewpoints does not span more than a couple centimeters, we can replace the array of cameras, with a single camera and an array of lenses. First suggested by Gabriel Lippmman in 1908, a sensor behind an

array of lenses (microlenses) records a different perspective view of the scene depending on the position of the microlens in the array. Using the two plane parameterization, this records a light field with a uv resolution depending on the number of microlenses and st resolution depending on the number of pixels (px) behind each microlens [2, 82]. If a standard lens is placed in front of the microlens array, focusing the light onto the microlens array, the light field is transposed such that the uv resolution depends on the number of pixels behind each microlens and the st resolution depends on the number of microlenses. This is the basis of a plenoptic camera. A schematic showing a 2D comparison between a conventional camera and a plenoptic camera is seen in figure 2.2. In a conventional camera, a point source on the world focal plane is focused onto a single pixel, shown in figure 2.2a. When a microlens array is inserted, angular information is encoded onto the image sensor. To illustrate this effect, light is colored depending on which pixel it strikes behind the microlens. For example, in figure 2.2b, the light that strikes the bottom-most pixel behind the illuminated microlens, comes only from the rays that are emitted from the point source in the range of angles colored purple. Thusly, the same point source is now focused over 8 px with the plenoptic camera instead of 1 with the conventional camera.

The plenoptic camera used in this dissertation was designed to be a high resolution version of the prototype camera built by Lynch et al. [83]. The design, assembly, and operation of this plenoptic camera has been optimized through 10 previous iterations of the high resolution version, all built by the author. The camera body is an Imperx Bobcat B6640 conventional scientific camera. The image sensor is a 29 megapixel (MP) TRUESENSE KAI-29050 interline transfer CCD which provides an image resolution of $6600 \times 4400\,\mathrm{px}^2$, with square pixels 5.5 microns in size. The microlens array was manufactured by Adaptive Optics Associates, Inc. to have a focal length of 308 microns and a microlens pitch of 77 microns such that there are approximately $14 \times 14\,\mathrm{px}^2$ per microlens. A hexagonal grid of 471×362 microlenses image light onto the image sensor [66]. The physical components of the plenoptic camera are illustrated in the rendering, shown in figure 2.3. The micorlens array

is the translucent glass slab in the center of the exploded view. The physical microlenses are glued to the back of a thick glass slab to allow for easier mounting and positioning of the lenses. The glass slab has a flange around the top edge, opposite to the microlenses, which rests in the microlens mount (MLM) assembly, shown in figure 2.3 as the 3 components surrounding the microlens array. The MLM assembly has undergone a number of revisions by the author with 3 specific goals in mind: (1) the precise positioning of the microlens array in front of the immage sensor, (2) the relative risk to the image sensor during installation of the MLM, and (3) the risk of dust accumulation on the image sensor and related components during regular use of the camera. The MLM shown in figure 2.3 is the latest design iteration, machined out of aluminum at Auburn University consisting of 3 main components: the MLM bracket, the MLM bracket holder, and the MLM cover plate. The microlens array rests in the MLM bracket supported by the glass flange. Each component is anodized black and then throughly cleaned in an ultrasonic cleaner. The MLM bracket is secured to the MLM bracket holder where it supported by 3 adjustment screws and 3 springs. Tightening each of these screws will bring the microlens array closer to the image sensor and when the screws are loosened, the springs push the microlens array further away from the image sensor. The 3 screws are situated to give the degrees of freedom to tilt the microlens array, in order to ensure the microlens array is uniformly 1 focal length away from the image sensor. The densely threaded screws allow for movement as precise as 18 µm. The MLM cover plate keeps the microlens array in the MLM bracket. The MLM bracket holder has been designed to resemble a part that is removed from the Imperx Bobcat B4820 such that the two feet on the bracket holder fit securely into the camera body, and the microlens array is straddling the image sensor, seen in figure 2.3 as the surface in the camera body that is slightly purple in color.

The plenoptic camera was assembled in the clean room following the standard operating procedure (SOP) designed by the author of this dissertation. The entire process takes place in Auburn University's Class-100 clean room, having less than $1 \cdot 10^5$ particles less than 0.1 µm

in size, per cubic meter. Additionally, all of the following operations occur on an ESD free mat while the engineers wear ESD bracelets. To begin, a dab of Threadlocker Blue is put ont oeach of the 3 adjustment screws, which are put through the MLM bracket and the springs are slipped over the protruding ends of the screws. While the MLM bracket is upside down on the mat (so that the springs do not fall off), the MLM bracket holder is place on top. These parts are flipped over and the each of the 3 screws is only slightly threaded into the MLM bracket holder. Now the microlens array is removed from the protective case and placed into the MLM bracket. The MLM cover plate is then secured on top of the bracket. Next, the F-mount bezel of the Bobcat B6640 was removed allowing access to the 4 screws that secured the part that protects the circuitry around the image sensor. This part was also removed, granting access to the cover glass of the image sensor, which was peeled off and discarded. Using a deionized air gun, the image sensor and MLM assembly are liberally cleaned. Finally, the MLM assembly is inserted into the B6640 body and secured. The microlens array is then aligned by shining a single LED at the camera and monitoring the output on a laptop. The adjustment screws are slowly tightened until the image formed behind each of the microlenses is a uniform, tight circle, less than 4 pixels in diameter. This indicates that the microlens array is situated 1 focal distance from the image sensor. The camera is stored safely and the f-mount bezel is taken to the machinist to have the interior diameter turned out to accommodate the MLM assembly. After reattaching the f-mount bezel, the camera is ready for use.

Appendix C

Proper Orthogonal Decomposition

The study of fluid mechanics has been associated with large data sets for some time now, both computationally and experimentally. The differences in the resolution of these two branches is an important factor when considering the decomposition of a data set using POD. The computational branch is standard in both industry and research as a powerful tool that produces finely sampled data sets with large spatial domains. Although the time resolution of computer generated simulations is highly resolved, it is often too computationally expensive to simulate long temporal periods. Conversely, experimental fluid mechanics are generally associated with extensive time domains that have exceedingly fine resolution. However, data-capturing methods such as hot-wire anemometry and laser Doppler anemometry record a relatively small spatial resolution. An outlier in the experimental branch of fluid mechanics is the optical measurement technique PIV, used in this thesis.

Credit for the application of POD to fluid mechanics is given to Lumley [84] who used POD to more accurately describe the turbulent flow structures that Townsend [85] originally termed "big eddies." These phenomena are now widely known as coherent structures. Another researcher, A. M. Yaglom, told Lumley in a personal conversation that POD is the natural idea to replace the usual Fourier decomposition in nonhomogeneous directions. This idea truly was natural because it was a solution reached by many researchers in a wide variety of fields. As a result, this technique is known by an assortment of names, primarily as principle component analysis (PCA) in mathematics, the Karhunen-Loève transform (KLT) in signal processing, and the Hotelling transform in multivariate quality control. The process of POD and its many affiliates all share a common goal: representing a data set with a linear combination of orthogonal functions that form the best basis to represent the data.

C.0.1 Basic Math Review

Despite being a relatively simple method to apply, the math behind POD is complex. The less math savvy reader is encouraged to review linear algebra and applied mathematics. The author recommends *Linear Algebra with Applications* [86] and *Applied Mathematics* [87] as a reference. Furthermore, readers that are first beginning POD are referred to *A tutorial on Principal Components Analysis* [88] and *An introduction to the proper orthogonal decomposition* [89]. Emphasis is placed on the covariance matrix [86, 88], the eigenvalue-eigenvector problem [86, 88], the Fredholm integral equation [87], and calculus of variations [87]. A workable example is found in the tutorial on PCA [88].

C.0.2 Overview of POD

The overall objective of POD is to approximate a data set u, defined in equation C.1. In this definition, t is the time instance that the data is sampled and x is a the data recorded at each instance, t. In fluid mechanics, this data is often velocity measurements, both two component and three component, or vorticity measurements. The following definitions in this section and the next follow the procedure outlined in The Springer Handbook of Fluid Mechanics [90].

$$u = f(x,t) \tag{C.1}$$

The approximation of u will be written as a sum defined in equation C.2, where $\phi^{(k)}(x)$ are basis functions, $a^{(k)}(t)$ are time function coefficients, and K is the number of basis and time functions to be used in the approximation. As $K \to \infty$, this approximation will become exact. This approximation is not exclusive to POD, for example, if the basis functions are defined as functions given *a priori*, equation C.2 could define a Fourier series, Legendre polynomials, or Chebyshev polynomials. Alternatively, POD seeks to determine basis functions that are "naturally intrinsic for the approximation of the function $u(x,t)$"

[90].

$$u(x,t) \approx \sum_{k=1}^{K} a^{(k)}(t)\phi^{(k)}(x) \tag{C.2}$$

Thus, the general objective of POD is to choose the basis functions $\phi^{(k)}(x)$ and then determine the time functions, $a^{(k)}(t)$, by using the corresponding basis functions, the former being more challenging. The next section defines the approach to defining this "naturally intrinsic" basis function, which is shown to reduce to an eigenvalue-eigenvector problem.

C.0.3 POD: The Eigenvalue Problem

This section familiarizes the reader with the proper orthogonal decomposition drawing from both Nobach et al. [90] and Holmes et al. [91]. To begin, let equation C.3 denote a set of observations, or snapshots, that exist in the real positive 3 dimensional space. These snapshots are obtained at discrete times throughout the domain of interest, $\Omega(\boldsymbol{x} = (x, y, z) \in \Omega)$

$$\{\boldsymbol{u}(\boldsymbol{X}), \boldsymbol{X} = (\boldsymbol{x}, t_n) \in D = \mathbb{R}^3 \times \mathbb{R}^+\} \tag{C.3}$$

These snapshots could be velocity fields, vorticity fields, temperature, etc. either measured experimentally or simulated numerically, recorded at different time steps or physical parameters (such as Reynolds number). Lumley [84] proposes to extract coherent structures from these random vector fields and defines a coherent structure as "the deterministic function which is best correlated on average with the realization $\boldsymbol{u}(\boldsymbol{X})$". Simply put, we seek a function $\boldsymbol{\Phi}$ that has the largest mean squared projection onto the observations. Mathematically, $\boldsymbol{\Phi}$ is the solution to constrained optimization problem defined in equation C.4, where $\langle\cdot\rangle$ denotes an averaging operation (temporal, spatial, ensemble, phase average).

$$\max_{\boldsymbol{\Psi}\in L^2(D)} \frac{\langle|(\boldsymbol{u},\boldsymbol{\Psi})|^2\rangle}{||\boldsymbol{\Psi}||^2} = \frac{\langle|(\boldsymbol{u},\boldsymbol{\Phi})|^2\rangle}{||\boldsymbol{\Phi}||^2} \tag{C.4}$$

Here $(\cdot,\cdot)$ and $||\cdot||^2$ denote the L^2 inner product and the L^2 norm, respectively, over D:

$$(\boldsymbol{u},\boldsymbol{\Phi}) = \int_D \boldsymbol{u}(\boldsymbol{X}) \cdot \boldsymbol{\Phi}^*(\boldsymbol{X}) \mathrm{d}\boldsymbol{X}, \qquad ||\boldsymbol{u}||^2 = (\boldsymbol{u},\boldsymbol{u}) \tag{C.5}$$

where the * represents the complex conjugate. Furthermore, the function $\mathbf{\Phi}$ is defined such that

$$||\mathbf{\Phi}||^2 = (\mathbf{\Phi}, \mathbf{\Phi}) = 1 \ . \tag{C.6}$$

Previously, it was suggested that defining the basis reduces to an eigenvalue problem. The current objective is to show that the solution to the maximization problem defined in equation C.4 can be cast in an equivalent eigenvalue problem of the form

$$\boldsymbol{A}\boldsymbol{v} = \lambda \boldsymbol{v}. \tag{C.7}$$

To accomplish this, equation C.4 first needs to be modified to the form of the Fredholm Integral Equation, a linear equation defined as

$$\int_a^b k(x,y)u(y)\mathrm{d}y - \lambda u(x) = f(x), \quad a \leqslant x \leqslant b \tag{C.8}$$

by Logan [87]. Here, u is the unknown function, f is a given continuous function, and λ is a parameter. The function k is called the kernel and is given *a priori*. The kernel is assumed continuous on the square $a \leqslant x \leqslant b, a \leqslant y \leqslant b$. If it is required that equation C.8 is homogeneous ($f \equiv 0$) and of the second kind ($\lambda \neq 0$), it follows that

$$\lambda u(x) = \int_a^b k(x,y)u(u)\mathrm{d}y \ . \tag{C.9}$$

This notation can be simplified by using integral operator notation. Seen below in equation C.10, K is the Fredholm integral operator. equation C.9 can be rewritten as equation C.11, which is observed to have the same form as the eigenvalue-eigenvector equation defined in equation C.7.

$$Ku(x) = \int_a^b k(x,y)u(y)\mathrm{d}y \tag{C.10}$$

$$Ku = \lambda u \tag{C.11}$$

Returning to the problem defined in equation C.4, define a new operator $\mathscr{R} : L^2(D) \to L^2(D)$ as

$$\mathscr{R}\mathbf{\Phi}(\boldsymbol{X}) = \int_D R(\boldsymbol{X}, \boldsymbol{X}')\mathbf{\Phi}(\boldsymbol{X}')\mathrm{d}\boldsymbol{X}' \tag{C.12}$$

where $R(\boldsymbol{X}, \boldsymbol{X}') = \langle \boldsymbol{u}(\boldsymbol{X}) \otimes \boldsymbol{u}^*(\boldsymbol{X}') \rangle$, termed the two-point space-time correlation tensor. The operator $\otimes$ is the dyadic product, such that if a and b are vectors, $a \otimes b = ab^T$. $\boldsymbol{X}'$ represents another snapshot, that may be identical to $\boldsymbol{X}$ but is not explicitly required to be. Here the operator $\mathscr{R}$ is a Fredholm integral operator, the function R is the kernel, and $\mathbf{\Phi}$ is the unknown function. In a general sense, this operator $\mathscr{R}$ is building what amounts to a covariance matrix of a zero-mean data set. This generalization is helpful when implementing POD computationally.

The L^2 inner product $(\mathscr{R}\mathbf{\Phi}, \mathbf{\Phi})$ in equation C.13 is expanded to equation C.14, then rearranged to form equation C.15.

$$(\mathscr{R}\mathbf{\Phi}, \mathbf{\Phi}) = \left(\int_D \langle \boldsymbol{u}(\boldsymbol{X}) \otimes \boldsymbol{u}^*(\boldsymbol{X}') \rangle \mathbf{\Phi}(\boldsymbol{X}')\mathrm{d}\boldsymbol{X}', \mathbf{\Phi}(\boldsymbol{X}) \right) \tag{C.13}$$

$$(\mathscr{R}\mathbf{\Phi}, \mathbf{\Phi}) = \int_D \int_D \langle \boldsymbol{u}(\boldsymbol{X}) \otimes \boldsymbol{u}^*(\boldsymbol{X}') \rangle \mathbf{\Phi}(\boldsymbol{X}')\mathrm{d}\boldsymbol{X}'\mathbf{\Phi}^*(\boldsymbol{X})\mathrm{d}\boldsymbol{X} \tag{C.14}$$

$$(\mathscr{R}\mathbf{\Phi}, \mathbf{\Phi}) = \left\langle \int_D \boldsymbol{u}(\boldsymbol{X})\mathbf{\Phi}^*(\boldsymbol{X})\mathrm{d}\boldsymbol{X} \int_D \boldsymbol{u}^*(\boldsymbol{X}')\mathbf{\Phi}(\boldsymbol{X}')\mathrm{d}\boldsymbol{X} \right\rangle \tag{C.15}$$

Finally, it is seen that equation C.15 is reduced to

$$(\mathscr{R}\mathbf{\Phi}, \mathbf{\Phi}) = \langle |\boldsymbol{u}, \mathbf{\Phi}||^2 \rangle \tag{C.16}$$

Observe that the right hand side of equation C.16 is identically equal to the numerator of the right hand side of equation C.4.

By repeating the steps in Equations C.13–C.15, it can be shown that

$$(\mathscr{R}\mathbf{\Phi}, \mathbf{\Upsilon}) = (\mathbf{\Phi}, \mathscr{R}\mathbf{\Upsilon}) \text{ for any } (\mathbf{\Phi}, \mathbf{\Upsilon}) \in [L^2(D)]^2. \tag{C.17}$$

The implications of this relationship in equation C.17 can be proved using spectral theory or calculus of variations to guarantee the maximization problem in equation C.4 has a solution equal to the largest eigenvalue of equation C.18. In summary, because of the equality of $(\mathscr{R}\mathbf{\Phi}, \mathbf{\Phi})$ and the numerator of equation C.4 (shown in equation C.16 and the relationship shown in equation C.17, it is concluded that maximizing $\mathscr{R}\mathbf{\Phi}$ will maximize equation C.4. As defined in equation C.11, the Fredholm operator of the unknown function is equal to the parameter λ times the unknown basis function $\mathbf{\Phi}$. It follows that the parameter λ represents the eigenvalues of equation C.18, and the basis functions $\mathbf{\Phi}$ are the eigenvectors, often called eigenmodes or modes.

$$\mathscr{R}\mathbf{\Phi} = \lambda\mathbf{\Phi} \tag{C.18}$$

To determine the time coefficients $a^{(k)}$, simply restructure equation C.2 to find that the time coefficients are actually projections of $\boldsymbol{u}$ onto $\mathbf{\Phi}$. This conclusion is a result of the orthonormality of eigenfunctions $\mathbf{\Phi}$, defined below in equation C.19. Then $a^{(k)}$ can be found using equation C.20. The coefficients $a^{(k)}$ are mutually uncorrelated and their mean square values are the eigenvalues themselves (equation C.21.

$$\sum_{i=1}^{n_c} \int_D \Phi_i^{(m)}(\boldsymbol{X})\Phi_i^{*(n)}(\boldsymbol{X})\mathrm{d}\boldsymbol{X} = \delta_{mn}; \quad \delta_{mn} = \begin{cases} 0, & \text{for } m \neq n \\ 1, & \text{for } m = n \end{cases} \tag{C.19}$$

$$a^{(k)} = (\boldsymbol{u}, \mathbf{\Phi}) \tag{C.20}$$

$$\langle a^{(n)} a^{*(m)} \rangle = \delta_{mn}\lambda^{(n)} \tag{C.21}$$

The basis and the coefficients are now defined and equation C.2 can now be used to approximate the data set. As K is increased, the snapshot is projected onto more modes and the approximation becomes more accurate. Because the modes are ranked from the most energy to least, it follows that the approximation is altered less as each successive mode is added to the summation.

This section has described the essence of the proper orthogonal decomposition in the classical approach. The following subsections will outline the procedure for implementing this technique in practice.

C.0.4 Classical Method vs Snapshots Method

Recall in the previous section that the averaging operation $\langle \cdot \rangle$ in equation C.4 remains undefined. This section describes the differences between two methods depending on how the averaging operation is defined. The Classical, or Direct, method averages over time while the Snapshots Method averages over space. These two methods are juxtaposed in figure C.1. Selecting one method over the other is as straightforward as categorizing the working data set.

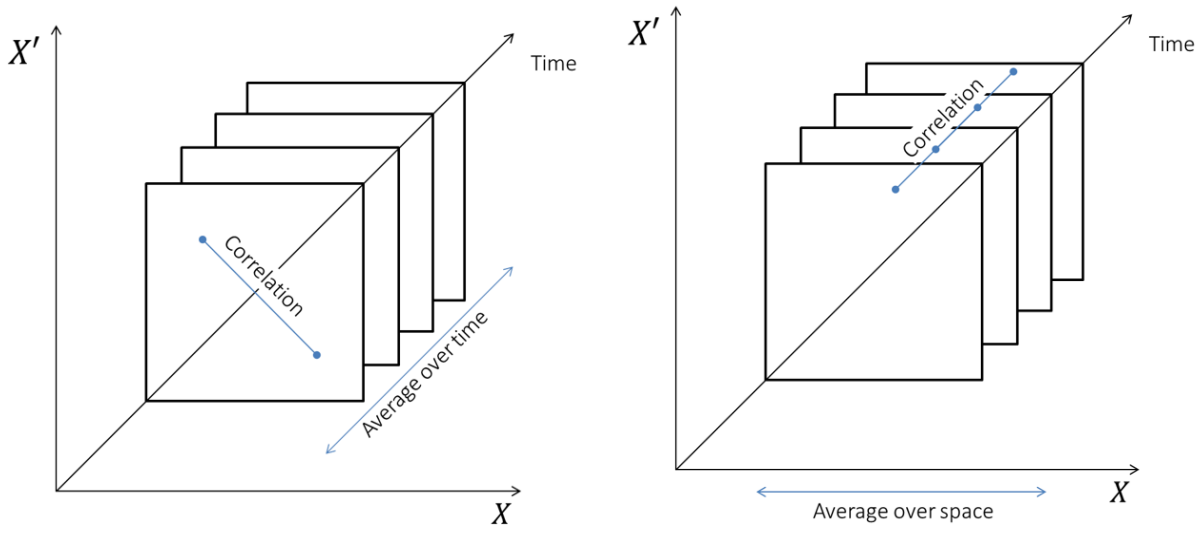

(a) (b)

Figure C.1: A comparison between two POD methods: (a) Classical Method; (b) Snapshots Method

Regarding fluid mechanics, Classical POD works best for experimental data. The averaging operation is over time, and the correlation is across space, which works well with data gathered using hot-wire anemometry or laser Doppler anemometry. These experimental methods record data at specific spatial locations (often limited by the number of instruments

in a measurement array), resulting in a data set with coarse spatial resolution. However, the measurements made by these instruments have a dense temporal resolution. During POD, this high-resolution temporal data is averaged and correlated across the low-resolution spatial data. While Classical POD is best suited for experimental data, Snapshot POD, first suggested by Sirovich [92], handles numerical simulation nicely. Data sets from numerical simulation (direct numerical simulation, large-eddy simulation, *etc.*), are usually highly resolved in space and time. However, due to computational cost, the time sample is generally very short. As a result of this constraint, computational data is more densely sampled in the spatial domain than the temporal. Snapshot POD averages this densely sampled spatial domain and correlates the data temporally.

An exception to this categorization is the experimental method, PIV. A typical PIV experiment gathers image pairs, which are correlated to form a data set of velocity vectors taken at different instances in time. A typical experiment could contain data at 1000 time instances, with each instance corresponding to thousands or tens of thousands of velocity vectors. In this way, PIV is more similar to numerical simulation than to the previously mentioned experimental methods.

As shown in figure C.1, Snapshot POD is the exact symmetry of classical POD. The mathematical implications of this are straightforward. The difference revolves around the assumption that $\mathbf{\Phi}$ has the form

$$\mathbf{\Phi}(\boldsymbol{x}) = \sum_{k=1}^{N_t} a(t_k)\boldsymbol{u}(\boldsymbol{x}, t_k) \tag{C.22}$$

where the coefficients $a(t_k), k = 1, \ldots, N_t$ are to be determined so that $\mathbf{\Phi}$ is a maximum to the optimization problem previously defined in equation C.4. Following the same process, it is shown that the maximum of equation C.4 is given by

$$\int_\Omega R(\boldsymbol{x}, \boldsymbol{x}')\mathbf{\Phi}(\boldsymbol{x}')\mathrm{d}\boldsymbol{x}' = \lambda\mathbf{\Phi}(\boldsymbol{x}) \tag{C.23}$$

It follows that the two-point correlation tensor $R(\boldsymbol{x}, \boldsymbol{x}')$ can be estimated assuming stationarity and ergodicity conditions as

$$R(\boldsymbol{x}, \boldsymbol{x}') = \frac{1}{N_t} \sum_{i=1}^{N_t} \boldsymbol{u}(\boldsymbol{x}, t_i) \otimes \boldsymbol{u}^*(\boldsymbol{x}', t_i) \ . \tag{C.24}$$

Finally, substituting the expression of R in equation C.24 and the decomposition of $\boldsymbol{\Phi}$ in equation C.22 into Equation (C.23 yields

$$\sum_{i=1}^{N_t} \left[\sum_{k=1}^{N_t} \frac{1}{N_t} \left(\int_\Omega \boldsymbol{u}(\boldsymbol{x}', t_k) \cdot \boldsymbol{u}^*(\boldsymbol{x}', t_i) \mathrm{d}\boldsymbol{x}' \right) a(t_k) \right] \times \boldsymbol{u}(\boldsymbol{x}, t_i) = \lambda \sum_{k=1}^{N_t} a(t_k) \boldsymbol{u}(\boldsymbol{x}, t_k) \ . \tag{C.25}$$

Which can be simplified to

$$\sum_{k=1}^{N_t} \frac{1}{N_t} \left[\boldsymbol{u}(\boldsymbol{x}'.t_k) \cdot \boldsymbol{u}^*(\boldsymbol{x}', t_i) \right] a(t_k) = \lambda a(t_i) \ , \ i = 1, \ldots, N_t \tag{C.26}$$

where the coefficients $a(t_k)$ are defined. equation C.26 can be recast as the eigenvalue-eigenvector problem

$$\boldsymbol{C}\boldsymbol{V} = \lambda \boldsymbol{V} \tag{C.27}$$

where

$$C_{ki} = \frac{1}{N_t} \int_\Omega \boldsymbol{u}(\boldsymbol{x}, t_k) \cdot \boldsymbol{u}^*(\boldsymbol{x}, t_i) \mathrm{d}\boldsymbol{x} \text{ and}$$
$$\boldsymbol{V} = \left[a(t_1), a(t_2), \ldots, a(t_N) \right]^T \ .$$

The definition of C is found to be the two-point temporal correlation tensor, which is straightforward to calculate. In direct symmetry to the calculation of the time coefficients in equation C.20, the basis function, or modes can be calculated similarly as

$$\boldsymbol{\Phi}^{(n)}(\boldsymbol{x}) = \frac{1}{N_t \lambda^{(n)}} \sum_{k=1}^{N_t} a^{(n)}(t_k) \boldsymbol{u}(\boldsymbol{x}, t_k) \ . \tag{C.28}$$

Appendix D

Correlation Matrices

D.1 auto-correlations

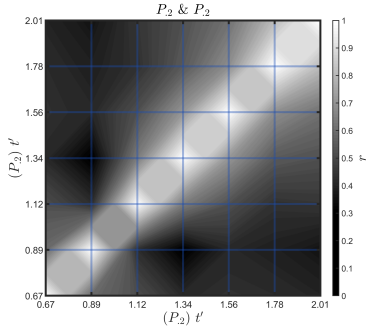

(a)

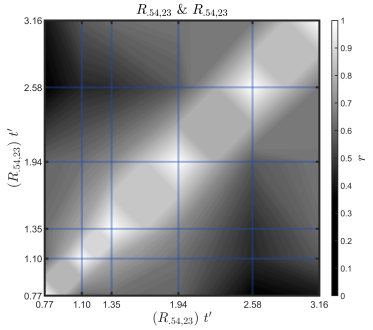

(b)

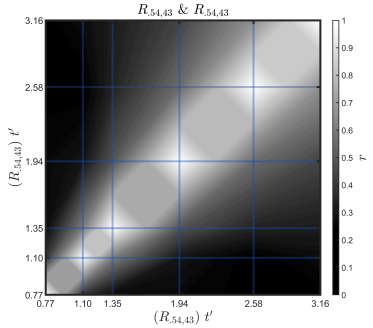

(c)

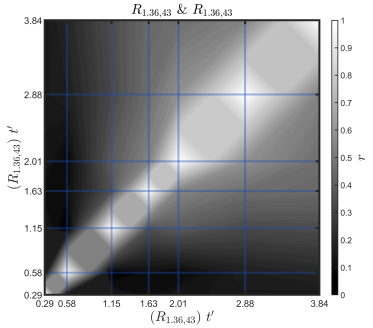

(d)

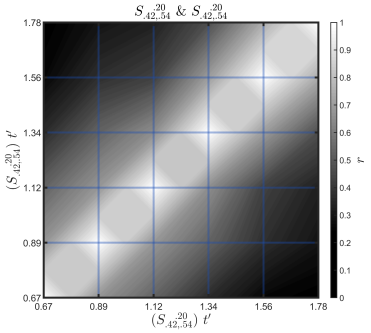
$S_{.42,.54}^{20}$ & $S_{.42,.54}^{20}$
$(S_{.42,.54}^{20})\ t'$
$(S_{.42,.54}^{20})\ t'$
r

(e)

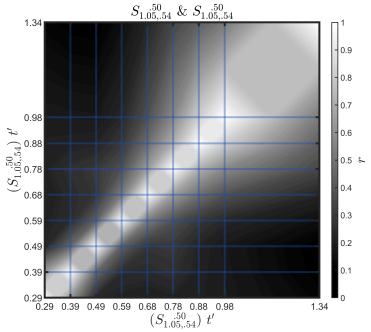
$S_{1.05,.54}^{50}$ & $S_{1.05,.54}^{50}$
$(S_{1.05,.54}^{50})\ t'$
$(S_{1.05,.54}^{50})\ t'$
r

(f)

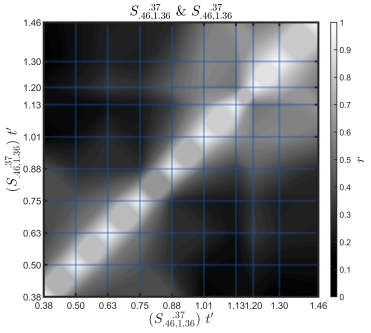
$S_{.46,1.36}^{37}$ & $S_{.46,1.36}^{37}$
$(S_{.46,1.36}^{37})\ t'$
$(S_{.46,1.36}^{37})\ t'$
r

(g)

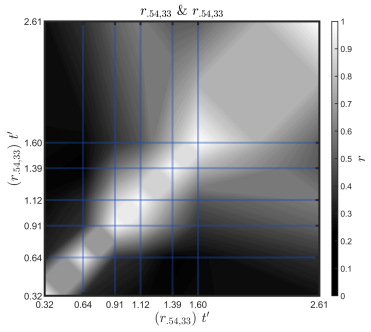
$r_{.54,33}$ & $r_{.54,33}$
$(r_{.54,33})\ t'$
$(r_{.54,33})\ t'$
r

(h)

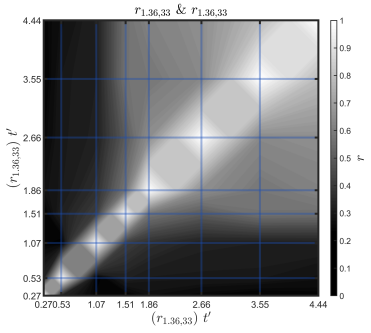
$r_{1.36,33}$ & $r_{1.36,33}$
$(r_{1.36,33})\ t'$
$(r_{1.36,33})\ t'$
r

(i)

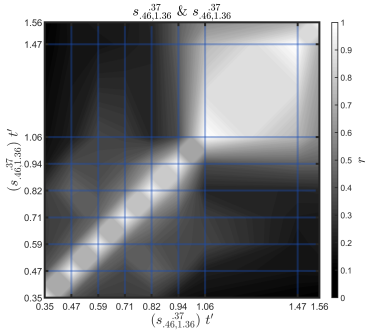
$s_{.46,1.36}^{37}$ & $s_{.46,1.36}^{37}$
$(s_{.46,1.36}^{37})\ t'$
$(s_{.46,1.36}^{37})\ t'$
r

(j)

D.2 Selected Correlations

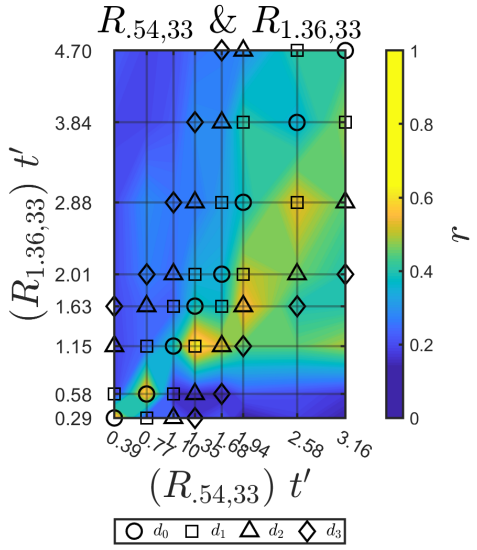

Figure D.0: Visualization of correlation map showing the cross-correlation of $R_{.54,33}$ and $R_{1.36,33}$, colored by r

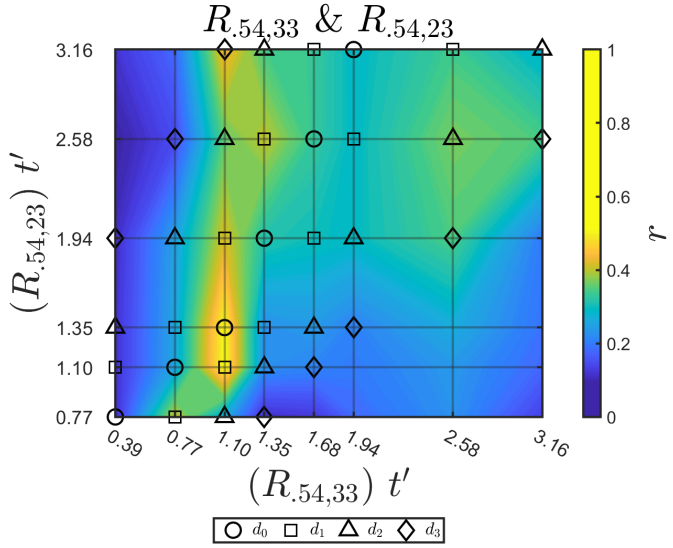

Figure D.1: Visualization of correlation map showing the cross-correlation of $R_{.54,33}$ and $R_{.54,23}$, colored by r

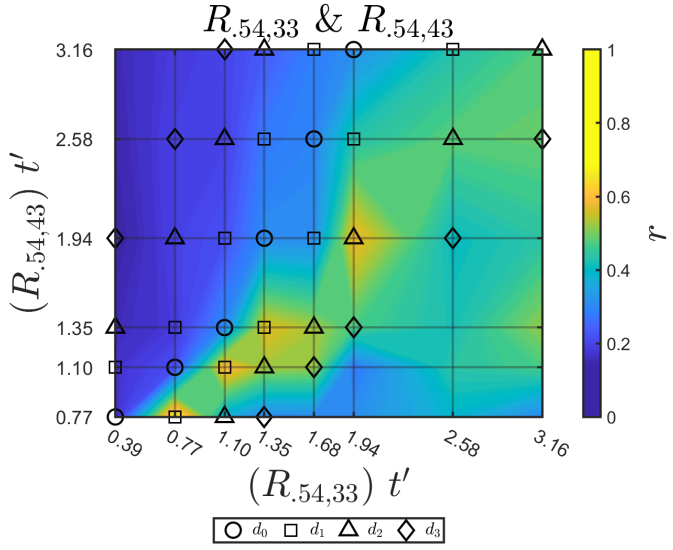

Figure D.2: Visualization of correlation map showing the cross-correlation of $R_{.54,33}$ and $R_{.54,43}$, colored by r

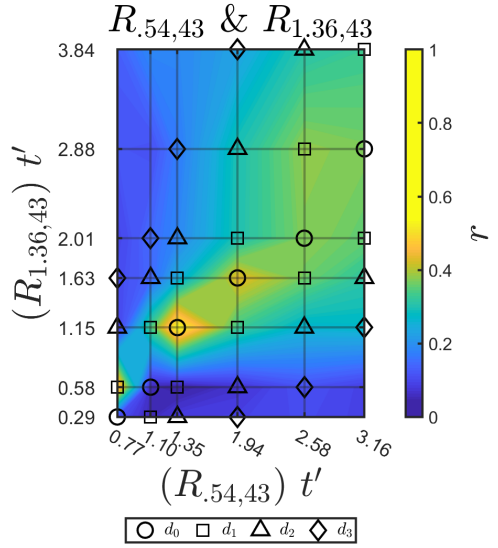

Figure D.3: Visualization of correlation map showing the cross-correlation of $R_{.54,43}$ and $R_{1.36,43}$, colored by r

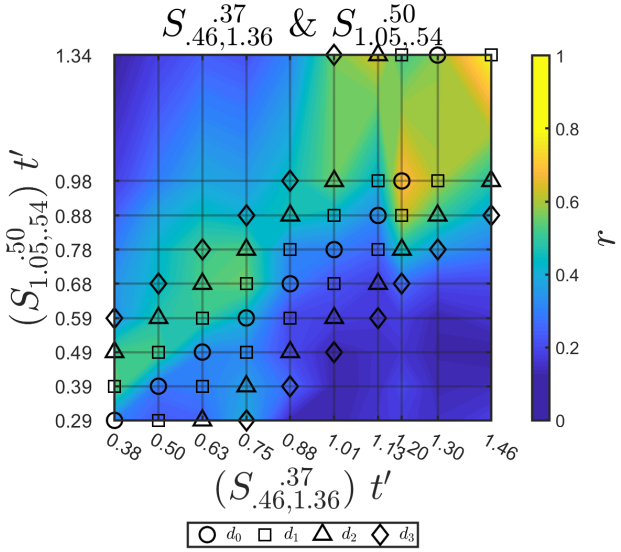

Figure D.4: Visualization of correlation map showing the cross-correlation of $S_{.46,1.36}^{.37}$ and $S_{.46,1.36}^{.37}$, colored by r

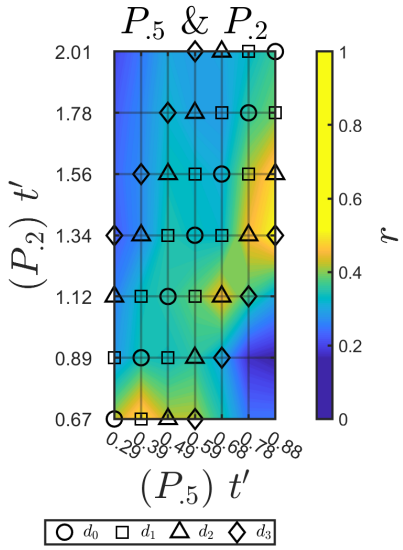

Figure D.5: Visualization of correlation map showing the cross-correlation of $P_{.5}$ and $P_{.2}$, colored by r

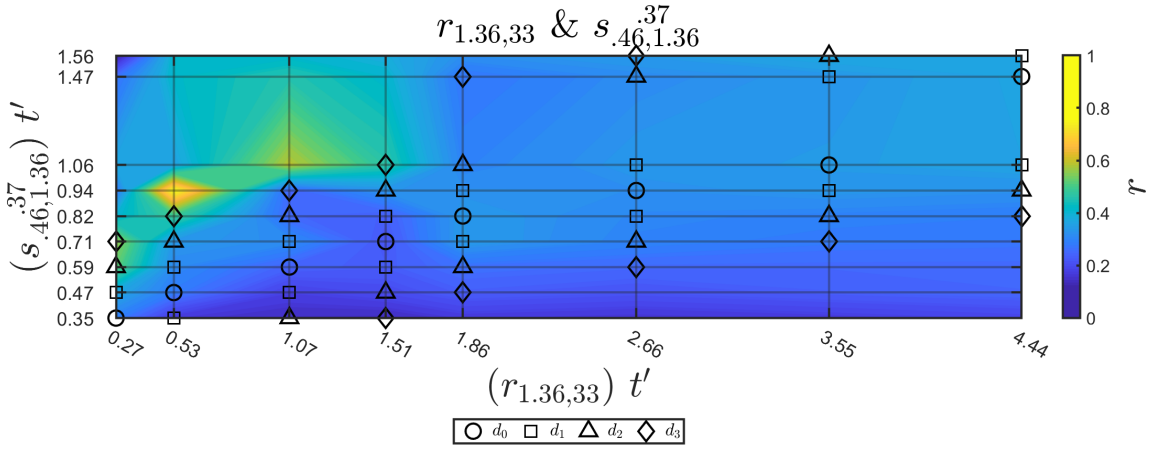

Figure D.6: Visualization of correlation map showing the cross-correlation of $r_{1.36,33}$ and $s^{.37}_{.46,1.36}$, colored by r

Appendix E

Code Appendix

E.1 POD Background Subtraction

```
#define _CRT_SECURE_NO_WARNINGS

#include <stdio.h>
#include <stdlib.h>
#include <time.h>
#include <armadillo>
#include <sys/stat.h>
#include "tiffio.h"
#include "mpi.h"
#include "DragonJSON.h"


static int readImage(char *imageFileName, double **imageData, int &width,
    int &length)
{
  TIFF *tif = TIFFOpen(imageFileName, "r");
  uint16 bpp;
  TIFFGetField(tif, TIFFTAG_IMAGELENGTH, &length);
  TIFFGetField(tif, TIFFTAG_IMAGEWIDTH, &width);
  TIFFGetField(tif, TIFFTAG_BITSPERSAMPLE, &bpp);

  tdata_t buffer = _TIFFmalloc(TIFFScanlineSize(tif));

  *imageData = (double*)calloc(width*length, sizeof(double));
  for (int j = 0; j < length; ++j) {
    TIFFReadScanline(tif, buffer, j, 0);
    for (int i = 0; i < width; ++i) {
      if (bpp == 16) {
        (*imageData)[i*length + j] = ((uint16*)buffer)[i];
      }
      else {
        (*imageData)[i*length + j] = ((uint8*)buffer)[i];
      }
    }
  }
  _TIFFfree(buffer);
  TIFFClose(tif);
  return 0;
}

int writeImage(char *imageFileName, double * image, int length, int width)
{
```

```
42
43
44    uint16 *imageData = (uint16*)calloc(length*width, sizeof(uint16));
45
46    for (int i = 0; i < width; ++i)
47      for (int j = 0; j < length; ++j) {
48        if (image[j * width + i] < 0) {
49          imageData[j * width + i] = 0;
50        }
51        else {
52          imageData[j * width + i] = static_cast<uint16>(image[j * width + i
                ]);
53        }
54      }
55    TIFF *tif = TIFFOpen(imageFileName, "wb");
56    TIFFSetField(tif, TIFFTAG_IMAGELENGTH, length);
57    TIFFSetField(tif, TIFFTAG_IMAGEWIDTH, width);
58    TIFFSetField(tif, TIFFTAG_SAMPLESPERPIXEL, 1);
59    TIFFSetField(tif, TIFFTAG_BITSPERSAMPLE, 16);
60    TIFFSetField(tif, TIFFTAG_PHOTOMETRIC, PHOTOMETRIC_MINISBLACK);
61    TIFFSetField(tif, TIFFTAG_ORIENTATION, ORIENTATION_TOPLEFT);
62
63    // CREATE BUFFER
64    uint16* buffer = (uint16*)_TIFFmalloc(TIFFScanlineSize(tif));
65
66    // WRITE BUFFER
67    for (int j = 0; j < length; ++j) {
68      for (int i = 0; i < width; ++i) {
69        buffer[i] = imageData[i*length + j];
70      }
71      int check_IO = TIFFWriteScanline(tif, buffer, j, 0);
72    }
73    free(imageData);
74    TIFFClose(tif);
75    _TIFFfree(buffer);
76    return 1;
77  }
78
79  void PODsnapshotsBackground(char* imageDir, char* resultsDir, int imStart,
        int imEnd, int imInc, int covImages, bool loadAve, bool loadC, bool
      loadMode, int camID)
80  {
81    clock_t begin = clock();
82    int totalImages = (imEnd - imStart) / imInc + 1;
83    // PRE ALLOCATION //
84
85    int width, height;
86    char imageFileNameTest[512];
87    char PODitemsDir[512];
88    sprintf(PODitemsDir,"%s/PODitems",resultsDir);
89    mkdir(PODitemsDir,0755);
90    double *imageTest;
91    sprintf(imageFileNameTest, "%s/0003.tif", imageDir);
```

```
92  readImage(imageFileNameTest, &imageTest, width, height); // GET WIDTH
        AND HEIGHT OF IMAGE
93  free(imageTest);
94  double *ave = (double*)calloc(width*height, sizeof(double));
95  arma::mat Cmat(covImages, covImages, arma::fill::zeros);
96
97
98  // LOG File
99  char logFileName[512];
100 sprintf(logFileName, "%s/log.txt", PODitemsDir);
101 FILE* logFile = fopen(logFileName, "w");
102 setbuf(logFile, NULL);
103 time_t startTime = time(0);
104 char buff[20];
105 strftime(buff, sizeof(buff), "%Y-%m-%d %H:%M:%S", localtime(&startTime))
        ;
106 fprintf(logFile, "\t%s\n--------------------------------\n", buff);
107 fprintf(logFile, "LOG FILE FOR POD BACKGROUND SUBTRACTION\n");
108
109 // CALCULATE AVERAGE
110 fprintf(logFile, "Averaging Images: ");
111
112 if (!loadAve) {
113
114   #pragma omp parallel for
115   for (int aveInd = 0; aveInd < covImages; ++ aveInd) {
116     char imageFileNameA[512];
117     double *imageA;
118     sprintf(imageFileNameA, "%s/%04d.tif", imageDir, (aveInd*imInc)+
          imStart);
119     readImage(imageFileNameA, &imageA, width, height);
120
121     for (int k = 0; k < width*height; ++k) {
122     #pragma omp atomic
123       ave[k] += imageA[k] / covImages;
124       //ave[k] = 0;
125     }
126     free(imageA);
127   }
128
129   char aveFileName[512];
130   sprintf(aveFileName, "%s/ave.bin", PODitemsDir);
131   FILE* fileID = fopen(aveFileName, "wb");
132   fwrite(ave, sizeof(double), height*width, fileID);
133   fclose(fileID);
134   sprintf(aveFileName, "%s/ave.tif", PODitemsDir);
135   writeImage(aveFileName, ave, height, width);
136 }
137 else {
138   char aveFileName[512];
139   sprintf(aveFileName, "%s/ave.bin", PODitemsDir);
140   FILE* fileID = fopen(aveFileName, "r");
141   fread(ave, sizeof(double), height*width, fileID);
142   fclose(fileID);
```

```
143   }
144
145
146   clock_t time1 = clock();
147   double elapsedTime = (double)(time1 - begin) / CLOCKS_PER_SEC;
148   fprintf(logFile, "Complete. %.2f min \n", elapsedTime / 60);
149
150   // COVARIANCE LOOP
151   fprintf(logFile, "Calculating Covariance Matrix: ");
152
153   if (!loadC) {
154     #pragma omp parallel for
155     for (int i = 0; i < covImages; ++i) {
156       char imageFileName1[512];
157       double *image1;
158       sprintf(imageFileName1, "%s/%04d.tif", imageDir, (i*imInc)+imStart);
159       readImage(imageFileName1, &image1, width, height);
160       for (int j = i; j < covImages; ++j) {
161         char imageFileName2[512];
162         double *image2;
163         sprintf(imageFileName2, "%s/%04d.tif", imageDir, (j*imInc)+imStart
              );
164         readImage(imageFileName2, &image2, width, height);
165         for (int k = 0; k < width*height; ++k) {
166           Cmat(i,j) += (image1[k] - ave[k]) * (image2[k] - ave[k]) /
                covImages;
167         }
168
169         Cmat(j, i) = Cmat(i, j);
170         free(image2);
171
172       }
173       free(image1);
174     }
175     char CmatFileName[512];
176     sprintf(CmatFileName, "%s/Cmat.txt", PODitemsDir);
177     Cmat.save(CmatFileName,arma::raw_ascii);
178   }
179   else {
180     char CmatFileName[512];
181     sprintf(CmatFileName, "%s/Cmat.txt", PODitemsDir);
182     Cmat.load(CmatFileName, arma::raw_ascii);
183   }
184
185   clock_t time2 = clock();
186   elapsedTime = (double)(time2 - time1) / CLOCKS_PER_SEC;
187   fprintf(logFile, "Complete. %.2f min \n", elapsedTime / 60);
188
189   // SOLVE THE EIGNENVALUE-EIGENVECTOR PROBLEM
190   fprintf(logFile, "Solving the Eigenvalue-Eigenvector Problem: ");
191   arma::cx_vec eigval;
192   arma::cx_mat eigvec;fprintf(logFile, ".");
193   arma::eig_gen(eigval, eigvec, Cmat);fprintf(logFile, "."); //try arma::
        eig_sym
```

```
194   arma::mat eigvalReal = arma::real(eigval);fprintf(logFile, ".");
195   arma::mat eigvecReal = arma::real(eigvec);fprintf(logFile, ".");
196   arma::uvec energyInd = arma::sort_index(eigvalReal, "descend");fprintf(
          logFile, ".");
197   arma::vec lam = arma::sort(eigvalReal, "descend");fprintf(logFile, ".");
198   arma::mat evector(covImages, covImages, arma::fill::zeros);fprintf(
          logFile, ".");
199
200 #pragma omp parallel for
201   for (int i = 0; i < energyInd.n_elem; ++i) {
202     evector.col(i) = eigvecReal.col(energyInd(i));
203   }
204   char eVecFileName[512];
205   sprintf(eVecFileName, "%s/evector.txt", PODitemsDir);
206   char lamFileName[512];
207   sprintf(lamFileName, "%s/lam.txt", PODitemsDir);
208   evector.save(eVecFileName, arma::raw_ascii);
209   lam.save(lamFileName, arma::raw_ascii);
210
211   clock_t time3 = clock();
212   elapsedTime = (double)(time3 - time2) / CLOCKS_PER_SEC;
213
214   fprintf(logFile, "Complete. %.2f min\n", elapsedTime / 60);
215
216   // CALCULATE THE NUMBER OF MODES FOR EACH ENERGY LEVEL
217
218   double lamSum = arma::sum(lam);
219   arma::vec lamNorm = lam / lamSum;
220   arma::vec cumLam = cumsum(lamNorm);
221
222   // CALCULATE OPTIMIZED NUMBER OF MODES TO SUBTRACTION
223   bool optimizeFlag = 0;
224
225     optimizeFlag = 1;
226     arma::vec lamDiff = lamNorm;
227     for (int i =0; i<covImages-2; ++i){
228       lamDiff(i) = lamNorm(i)-lamNorm(i+1);
229     }
230
231     double epsilon = 1/(double)covImages;
232     int autoMode = 0;
233
234     for (int i =0; i<covImages-2; ++i){
235
236       if(lamDiff(i)<epsilon){
237         if(lamDiff(i+1)<epsilon){
238           if(lamDiff(i+2)<epsilon){
239           autoMode = i;
240           break;
241           }
242         }
243       }
244     }
245     fprintf(logFile,"Optimized Number of modes: %d\n",autoMode);
```

```
246     arma::mat modes2use(1, 1, arma::fill::zeros);
247     modes2use(0)= autoMode;
248 
249 
250   int numOfModes = modes2use[modes2use.n_elem - 1];
251 
252   // CALCULATE EACH MODE //
253 
254   fprintf(logFile, "Calculating Modes: ");
255 
256   if (!loadMode) {
257 
258     for (int modeInd = 0; modeInd < numOfModes; ++modeInd) {
259       double *mode;
260       mode = (double*)calloc(height * width, sizeof(double));
261 #pragma omp parallel for
262       for (int imageInd = 0; imageInd < covImages; ++imageInd) {
263         double *imageM;
264         char imageFileNameM[512];
265         sprintf(imageFileNameM, "%s/%04d.tif", imageDir, (imageInd*imInc)
              + imStart);
266         readImage(imageFileNameM, &imageM, width, height);
267         for (int j = 0; j < width*height; ++j) {
268           mode[j] += evector(imageInd, modeInd)*(imageM[j]-ave[j]);
269         }
270         free(imageM);
271       }
272       char modeFileName[512];
273       sprintf(modeFileName, "%s/mode%d.bin", PODitemsDir, modeInd + 1);
274       FILE* fileID = fopen(modeFileName, "wb");
275       fwrite(mode, sizeof(double), width*height, fileID);
276       fclose(fileID);
277       free(mode);
278     }
279   }
280 
281   clock_t time4 = clock();
282   elapsedTime = (double)(time4 - time3) / CLOCKS_PER_SEC;
283 
284   fprintf(logFile, "Complete. %.2f min\n", elapsedTime / 60);
285 
286 
287   // SUBTRACTION OF REDUCED ORDER PROJECTIONS
288   //Main Loop
289 
290   fprintf(logFile, "Calculating Reduced Order Projections and Subtracting:
          ");
291 
292 
293   for (int reconInd = 0; reconInd < modes2use.n_elem; ++reconInd) {
294     // Make Output Dirs
295 
296     char energyDir[512], subDir[512];
297     if(optimizeFlag){
```

```
298     sprintf(energyDir, "%s/Optimized", resultsDir);
299     }
300     else {
301     sprintf(energyDir, "%s/%.0f", resultsDir, modes2use(reconInd));
302     }
303     sprintf(subDir, "%s/camera%d", energyDir,camID);
304     mkdir(energyDir,0755);
305     mkdir(subDir,0755);
306     // Image loop
307       #pragma omp parallel for
308     for (int imageInd = 0; imageInd < totalImages; ++imageInd ) {
309       double *image;
310       char imageFileName[512];
311       sprintf(imageFileName, "%s/%04d.tif", imageDir, (imageInd*imInc)+
              imStart);
312       readImage(imageFileName, &image, width, height);
313       double *RO = (double*)calloc(height * width, sizeof(double));
314       for (int k = 0; k < width*height; ++k) {
315         RO[k] = ave[k];
316       }
317       // Mode Loop
318       for (int modeInd = 0; modeInd < modes2use(reconInd); ++modeInd) {
319         double *mode;
320         mode = (double*)calloc(height * width, sizeof(double));
321         char modeFileName[512];
322         sprintf(modeFileName, "%s/mode%d.bin", PODitemsDir, modeInd+1);
323         FILE* fileID = fopen(modeFileName, "r");
324         fread(mode, sizeof(double), width*height, fileID);
325         fclose(fileID);
326         double a_num = 0, a_den = 0;
327         // Calc time coefficient
328         for (int k = 0; k < width*height; ++k) {
329           a_num += (image[k]-ave[k]) * mode[k];
330           a_den += mode[k] * mode[k];
331         }
332         double a = a_num / std::max(0.01,a_den);
333         // Calc Reduced Order
334         for (int k = 0; k < width*height; ++k) {
335           RO[k] += a*mode[k];
336         }
337
338         free(mode);
339       }
340       // Save Image minus Projection
341       double *imageSub = (double*)calloc(height * width, sizeof(double));
342       for (int k = 0; k < height*width; ++k) {
343         imageSub[k] = image[k] - RO[k];
344       }
345       char imageSubFileName[512];
346       sprintf(imageSubFileName, "%s/%04d.tif", subDir, (imageInd*imInc) +
              imStart);
347       writeImage(imageSubFileName, imageSub, height, width);
348
349       free(RO);
```

```
350       free(image);
351       free(imageSub);
352     }
353   }
354
355   clock_t end = clock();
356   elapsedTime = (double)(end - time4) / CLOCKS_PER_SEC;
357
358   fprintf(logFile, "Complete. %.2f min\n", elapsedTime / 60);
359   double totalTime = (double)(end - begin) / CLOCKS_PER_SEC;
360   fprintf(logFile, "Total Computation Time: %.2f min\n", totalTime / 60);
361   time_t endTime = time(0);
362   strftime(buff, sizeof(buff), "%Y-%m-%d %H:%M:%S", localtime(&endTime));
363   fprintf(logFile, "-------------------------------\n\t%s\n", buff);
364   fclose(logFile);
365
366
367 }
368
369 int main(int argc,char* argv[]) {
370 setbuf(stdout,NULL);
371
372
373 MPI_Init(&argc, &argv);
374 int nodeCount, nodeID;
375 MPI_Comm_size( MPI_COMM_WORLD, &nodeCount );
376 MPI_Comm_rank( MPI_COMM_WORLD, &nodeID);
377
378
379
380 JSON *jsonID = JSON_readFile(argv[1]);
381
382 char *mainDir       = JSON_getArrayStringElement(jsonID,"mainDirectory",
      nodeID);
383
384 //char *mainDir       = JSON_getString(jsonID,"mainDirectory");
385 printf("Node %d is loading images from '%s'\n",nodeID,mainDir);
386 /*
387 bool loadAve        = JSON_getBool(jsonID,"loadAverage") ;
388 bool loadC          = JSON_getBool(jsonID,"loadCovariance") ;
389 bool loadMode       = JSON_getBool(jsonID,"loadModes");
390 int  imStart    = JSON_getInt(jsonID,"imageStart");
391 int  imEnd      = JSON_getInt(jsonID,"imageEnd");
392 int  imInc      = JSON_getInt(jsonID,"imageIncrement") ;
393 int  covImages      = JSON_getInt(jsonID,"covarianceImages");
394 int  nCameras       = JSON_getInt(jsonID,"nCameras");
395
396 char *mainDir       = JSON_getArrayStringElement(jsonID,"mainDirectory",
      nodeID);
397 //char *mainDir       = JSON_getString(jsonID,"mainDirectory");
398 */
399 bool loadAve        = JSON_getBool(jsonID,"loadAverage") ? JSON_getBool(
      jsonID,"loadAverage") :0;
```

```
bool loadC          = JSON_getBool(jsonID,"loadCovariance") ? JSON_getBool
    (jsonID,"loadCovariance"): 0;
bool loadMode       = JSON_getBool(jsonID,"loadModes") ? JSON_getBool(
    jsonID,"loadModes"): 0;
int  imStart    = JSON_getInt(jsonID,"imageStart");
int  imEnd      = JSON_getInt(jsonID,"imageEnd");
int  imInc      = JSON_getInt(jsonID,"imageIncrement") ? JSON_getInt(
    jsonID,"imageIncrement"): 1;
int  covImages      = JSON_getInt(jsonID,"covarianceImages") ? JSON_getInt
    (jsonID,"covarianceImages"): imEnd - imStart +1;
int  nCameras       = JSON_getInt(jsonID,"nCameras") ? JSON_getInt(jsonID,
    "nCameras"): 1;

  //
     ------------------------------------------------------------------------


  for (int camID = 0; camID < nCameras; ++camID){
    int camID = 0;
    char resultsDir[512];
    sprintf(resultsDir,"%s/Processed",mainDir);
    char imageDir[512];
    sprintf(imageDir,"%s/camera%i",mainDir,camID);
    mkdir(resultsDir,0755);



    PODsnapshotsBackground(imageDir, resultsDir, imStart, imEnd, imInc,
        covImages, loadAve, loadC, loadMode,camID);
    }


    JSON_destroy(jsonID);
    MPI_Finalize();

    return 0;
  }
```

E.2 Coordinate Transformation Functions

E.2.1 Visually Click LE and TE

```
function [settings] = clickTransformationPoints(jsonFileName,forceFun)

settings = JSON.parsefile(jsonFileName);
fields = fieldnames(settings);

if ~any(strcmp(fields,'coordinateTransformation')) || forceFun == 1
    addpath(genpath('K:\Documents\Dragon\Dragon_matlab'))
                                % add Dragon functions to path
    DragonFilePath = 'K:\Documents\Dragon\Dragon_redist\Dragon';
    isDragonLoaded = DragonLoadLibrary(DragonFilePath);

    settings.algorithm = 0;
```

```
12      struct2json(settings,jsonFileName);
13      DragonInitFromSettingsFile(jsonFileName);
14      rawImageFile = [settings.imageDirectoryLocal(1:18) 'Raw/' settings.
            imageDirectoryLocal(19:end) 'camera0/0000.tif'];
15      rawImage = double(imread(rawImageFile));
16      xVec = linspace(-settings.nPixelsX * settings.p_p/2,settings.nPixelsX
            * settings.p_p/2,settings.nVoxelsX);
17      yVec = linspace(-settings.nPixelsY * settings.p_p/2,settings.nPixelsY
            * settings.p_p/2,settings.nVoxelsY);
18  %
19      xVec = linspace( settings.xMin, settings.xMax, settings.nVoxelsX );
20      yVec = linspace( settings.yMin, settings.yMax, settings.nVoxelsY );
21
22      % Read in Volumetric Calbration Coefficients
23      fileID = fopen([settings.lfcalDirectoryLocal 'camera0.drg-lfcal'],'r')
            ;
24      lfcoeff = fscanf(fileID,'%f,%f',[2,56]);
25      fclose(fileID);
26
27      DragonBuildRadiance([settings.mcalDirectoryLocal 'camera0.drg-mcal'],
            rawImage);
28  %     [perspectiveImage] = DragonGeneratePerspectiveViews(xVec,yVec,0,0);
29      refocusImage = DragonReconstructToImage(xVec,yVec,0,1,lfcoeff(1,:),
            lfcoeff(2,:));
30      sound(randn(4096, 1), 5000)
31      pause(1);
32      fh = figure; set(fh,'Position',[ 9 169 1424 1188]);
33      imagesc(xVec,yVec,refocusImage');
34      title('Click the Leading Edge and Trailing Edge of the Volume')
35      [Ax,Ay] = ginput(2);
36      close(fh)
37      beta = atan2(diff(Ay),diff(Ax));
38
39      settings.algortihm = 2;
40      settings.coordinateTransformation = [Ax(1), Ay(1), beta];
41      struct2json(settings,jsonFileName);
42      DragonQuit();
43  end
```

E.2.2 Coordinate Transformation to $x', y'z'$ grid

```
1   function [vectorFolderOut] = coordinateTransformation(jsonFileName,
        forceFun)
2
3   settings = JSON.parsefile(jsonFileName);
4   fields = fieldnames(settings);
5
6   k = strfind(settings.vectorDirectoryLocal,'vecs');
7   dirOut = [settings.vectorDirectoryLocal(1:k-1) 'Processed' settings.
        vectorDirectoryLocal(k:end)];
8
9   if exist(dirOut,'dir') && forceFun ~= 1
10      vectorFolderOut = folder(dirOut);
11  else
```

```
12
13      vectorFolderOut = folder(dirOut);
14
15      [settings] = clickTransformationPoints(jsonFileName,0);
16
17      mmPerVox = [(settings.xMax-settings.xMin)/settings.nVoxelsX;
18          (settings.yMax-settings.yMin)/settings.nVoxelsY;
19          (settings.zMax-settings.zMin)/settings.nVoxelsZ];
20
21      fContents = dir([settings.vectorDirectoryLocal '*.plt']);
22
23      for idx = 1:2%numel(fContents)
24
25          dataStruct = loadplt([settings.vectorDirectoryLocal fContents(idx)
                .name]);
26
27          % Make the uniform grid for output
28          xVecLoc = linspace(settings.xMin,settings.xMax,size(dataStruct.X
                ,1));
29          yVecLoc = linspace(settings.yMin,settings.yMax,size(dataStruct.Y
                ,2));
30          zVecLoc = linspace(settings.zMin,settings.zMax,size(dataStruct.Z
                ,3));
31          xVecSpace = mean(diff(xVecLoc));
32          yVecSpace = mean(diff(yVecLoc));
33          zVecSpace = mean(diff(zVecLoc));
34
35          [Xq,Yq,Zq] = ndgrid(xVecLoc(1):xVecSpace:xVecLoc(end)*2,yVecLoc(1)
                :yVecSpace:yVecLoc(end)*2,zVecLoc);
36
37
38          % shift, scale and rotate the X-Y plane
39          dataStruct.X = mmPerVox(1)*dataStruct.X + settings.xMin - settings
                .coordinateTransformation(1);% This shifts the coordinate
                system to centered on the LE
40          dataStruct.Y = mmPerVox(2)*dataStruct.Y+ settings.yMin - settings.
                coordinateTransformation(2); % but still aligned with image
41
42          % scale and roatate the U-V velocities
43          dataStruct.U = dataStruct.U*mmPerVox(1)/(1000*settings.deltaT);
44          dataStruct.V = dataStruct.V*mmPerVox(2)/(1000*settings.deltaT);
45          %
46          % shift and scale Z and W
47          dataStruct.Z = -(mmPerVox(3)*dataStruct.Z + settings.zMin);
48          dataStruct.W = -(dataStruct.W*mmPerVox(3)/(1000*settings.deltaT));
49
50
51          dataInterp = struct;
52          dataInterp.X = Xq*cos(-settings.coordinateTransformation(3)) + Yq*
                sin(-settings.coordinateTransformation(3));
53          dataInterp.Y = Yq*cos(-settings.coordinateTransformation(3)) - Xq*
                sin(-settings.coordinateTransformation(3));
54          dataInterp.Z = Zq;
55
```

```
        varNames = fieldnames(dataStruct);
        for vInd = 4:numel(varNames)
            switch varNames{vInd}
                case 'IS_VALID'
                    dataInterp.(varNames{vInd})= interpn(dataStruct.X,
                        dataStruct.Y,dataStruct.Z,dataStruct.(varNames{vInd
                        }),dataInterp.X,dataInterp.Y,dataInterp.Z,'nearest'
                        ,0);
                otherwise
                    dataInterp.(varNames{vInd})= interpn(dataStruct.X,
                        dataStruct.Y,dataStruct.Z,dataStruct.(varNames{vInd
                        }),dataInterp.X,dataInterp.Y,dataInterp.Z,'linear'
                        ,0);
            end
        end

        dataInterp.U = dataInterp.U*cos(settings.coordinateTransformation
            (3)) + dataInterp.V*sin(settings.coordinateTransformation(3));
        dataInterp.V = dataInterp.V*cos(settings.coordinateTransformation
            (3)) - dataInterp.U*sin(settings.coordinateTransformation(3));

        dataInterp.X = Xq/1000; % mm  to m
        dataInterp.Y = Yq/1000; % mm  to m
        dataInterp.Z = Zq/1000; % mm  to m

        dataInterp.IS_MASKED(dataInterp.X > 0 & dataInterp.X <0.0726 &
            dataInterp.Y < 0 & dataInterp.Y > -0.002) =  1; % mask wing
        dataInterp = wingvelocity(dataInterp,settings);
        writeplt(dataInterp,[vectorFolderOut fContents(idx).name]);
    end

end

end
```

E.2.3 Remove Wing Velocity

```
function [data,phi_dot,alpha_dot] = wingvelocity(data,settings)


slashes = strfind(settings.imageDirectory,'/');
j = strfind(settings.imageDirectory,'j0.');
k = strfind(settings.imageDirectory,'k0');
krg = strfind(settings.imageDirectory,'k_rg');
Rgc = strfind(settings.imageDirectory,'Rg_c');

d = slashes - Rgc;
d(d<0) = 100;
a = min(d)-1;
RGC = settings.imageDirectory(Rgc+4:Rgc+a);
span = settings.imageDirectory(Rgc+a+2:Rgc+a+3);
Rgc = str2double(RGC);
span = str2double(span);
phi_dot = 0;
```

```
alpha_dot = 0;

if isempty(j)
    j = strfind(settings.imageDirectory,'j1.');
end

if ~isempty(j)
    d = slashes - j;
    d(d<0) = 100;
    a = min(d)-1;
    J = settings.imageDirectory(j+1:j+a);
    J = str2double(J);
    phi_dot = 0.12/(J*Rgc*.0762);
elseif ~isempty(k)
    d = slashes - k;
    d(d<0) = 100;
    a = min(d)-1;
    K = settings.imageDirectory(k+1:k+a);
    K = str2double(K);
    alpha_dot = .12*K/.0762;
elseif ~isempty(krg)
    d = slashes - krg;
    d(d<0) = 100;
    a = min(d)-1;
    KRG = settings.imageDirectory(krg+4:krg+a);
    KRG = str2double(KRG);
    switch KRG
        case 0.22
            J = 0.5;
            K = 0.5;
        case 0.39
            J = 1.25;
            K = 0.5;
        case 0.2
            J = 0.5;
            K = 0.5;
        case 0.5
            J = 0.5;
            K = 1.12;
    end
    alpha_dot = .12*K/.0762;
    phi_dot = 0.12/(J*Rgc*.0762);
end


data.V = data.V +alpha_dot*data.X + phi_dot*(data.Z+Rgc*.0762*-.0762 +
    span/100*2*.0762);
data.Z = data.Z + span/100*2*.0762;
```

E.3 Correlation Analysis

```
clear;clc;

corrFolder = 'K:\IowaExperiment\Correlations\';
```

```
outFolder = 'C:\Users\kzj0017\Box\My Research\Correlations\';
contents = dir([corrFolder '*.plt']);

N = numel(contents);
C = zeros(N,N);

t = loadplt([corrFolder 'Rg_c3.25j0.5_35__6.plt']);
zer = zeros(size(t.L,1)+5,size(t.L,2)+5,size(t.L,3)+5);
Z = t.Z;
X = t.X;
Y = t.Y;
fprintf('Correlating:              ')
for i = 1:N
    f1 = loadplt([corrFolder contents(i).name]);
    X1 = zer;
    [~,x1] = min(abs(X(:,1,1)-f1.X(1,1,1)));
    x2 = x1+numel(f1.X(:,1,1))-1;
    [~,y1] = min(abs(Y(1,:,1)-f1.Y(1,1,1)));
    y2 = y1+numel(f1.Y(1,:,1))-1;
    [~,z1] = min(abs(Z(1,1,:)-f1.Z(1,1,1)));
    z2 = z1+numel(f1.Z(1,1,:))-1;
    X1(x1:x2,y1:y2,z1:z2) = f1.L;
    fprintf('\b\b\b\b\b\b\b%3d     ',i)
    for j = i:N
        f2 = loadplt([corrFolder contents(j).name]);
        X2 = zer;
        [~,x1] = min(abs(X(:,1,1)-f2.X(1,1,1)));
        x2 = x1+numel(f2.X(:,1,1))-1;
        [~,y1] = min(abs(Y(1,:,1)-f2.Y(1,1,1)));
        y2 = y1+numel(f2.Y(1,:,1))-1;
        [~,z1] = min(abs(Z(1,1,:)-f2.Z(1,1,1)));
        z2 = z1+numel(f2.Z(1,1,:))-1;
        X2(x1:x2,y1:y2,z1:z2) = f2.L;
        C(i,j) = sum(X1(:).*X2(:));
        C(j,i) = C(i,j);
        fprintf('\b\b\b%3d',j)
    end
end
save([corrFolder 'C.mat'],'C');

load([corrFolder 'C.mat']);
Cn = C;
for i=1:N
    for j = i:N
        Cn(i,j) = C(i,j)/(sqrt(C(i,i)*C(j,j)));
        Cn(j,i) = Cn(i,j);
    end
end
```

```
clear;clc;close all
corrFolder = 'K:\IowaExperiment\Correlations\';
SVGFolder =  'D:\Dropbox\My Research\JFMv2\figures\Correlations\';
figFolder = folder([corrFolder 'plots\']);
load([corrFolder 'C_j.mat'])
```

```
load([corrFolder 'ordered_j.mat'])
load([corrFolder 'data.mat'])
C= Cn;
f = figure(1);
bounds = [  1   6;
    7   13;
    14  22'
    23  28;
    29  36;
    37  42;
    43  52;
    53  60;
    61  67;
    68  74;
    75  81;
    82  89;
    90  99;
    100 107
    ];

names =  {
    'S_{m-,f}';   %1
    'S_{m,f}';      %2
    'S_{f,f}';   %3
    'R_{f25}';   %4
    'R_{f35}';      %5
    'R_{f45}';   %6
    'S_{m,s}';    %7
    'R_{s35}';   %8
    'R_{s45}';   %9
    'P_{s}';    %10
    'P_{m}';    %11
    'r_{f35}';      %12
    's_{m,s}';      %13
    'r_{s35}';      %14

    };

for b1 = 5
    for b2 =2
        b = [b1 b2];
        tau =zeros(size(data,1),1);
        for ind = 1:size(data,1)
            tau(ind) =  taucalc(data(ind,:));
        end

        tauX = repmat(tau,[1 size(C,2)]);
        tauY = tauX';
        Cmap = flipud(gray(100));
        ind = b(1);


        c = C(bounds(ind,1):bounds(ind,2),:);
        i = tauX(bounds(ind,1):bounds(ind,2),:);
```

```
60          j = tauY(bounds(ind,1):bounds(ind,2),:);
61          iMin = min(i(:)); iMax = max(i(:));
62          jMin = min(j(:)); jMax= max(j(:));
63          iRange = linspace(iMin-iMin/5,iMax+iMin/5,20);
64          jRange = linspace(jMin-jMin/5,jMax+jMin/5,20);
65          H = zeros(numel(iRange),numel(jRange));
66          h = H;
67          for idx = 1:numel(c)
68              [~,iInd] = min(abs(i(idx)-iRange));
69              [~,jInd] = min(abs(j(idx)-jRange));
70              H(iInd,jInd)= H(iInd,jInd) + c(idx);
71              h(iInd,jInd)= h(iInd,jInd) + 1;
72          end
73          MkrI = 1;
74          if numel(b) == 1
75              idx = b;
76          else
77              flag = 1;
78              idx = b(2);
79          end
80          ii = i(:,bounds(idx,1):bounds(idx,2));
81          jj = j(:,bounds(idx,1):bounds(idx,2));
82          cc = c(:,bounds(idx,1):bounds(idx,2));
83          %
84          set(f,'Color',[1 1 1],'Position',[1 1 1001 1001],'visible','off');
85          pause(.5)
86          for idx2 = 1:numel(ii)
87              scatter(ii(idx2),jj(idx2),cc(idx2).^2.*1000,[0 0 0],'s','
                    filled')
88              hold on
89          end
90
91
92
93
94          ylabel('\fontsize{20}{0}\selectfont $\frac{t}{\tau}$','interpreter
                ','latex')
95          xlabel('\fontsize{20}{0}\selectfont $\frac{t}{\tau}$','interpreter
                ','latex')
96          axis square
97          set(gca,'fontsize',20)
98          title([names{b(1)} ' vs ' names{b(2)}],'fontsize',30,'fontweight',
                'normal')
99          f.PaperPositionMode = 'auto';
100         f_pos = f.PaperPosition;
101         f.PaperSize = [f_pos(3) f_pos(4)];
102         n1 = names{b(1)};
103         n2 = names{b(2)};
104         if any(b1 == [12 13 14])
105             n1 = [n1(1) n1];
106         end
107         if any(b2 == [12 13 14])
108             n2 = [n2(1) n2];
109         end
```

```
110
111         print([SVGFolder  n1 '_' n2], '-deps')
112
113
114         h = figure('Color',[1 1 1],'Position',[994 41 559 1292]);
115
116         subplot(9,1,1:3)
117         plot(ii(:,1),data(bounds(b(1),1):bounds(b(1),2),5),'-ok')
118         hold on
119         plot(jj(1,:)',data(bounds(b(2),1):bounds(b(2),2),5),'--sk')
120         ylabel('$\alpha_\mathrm{eff}$','fontsize',15,'interpreter','latex'
              )
121         xlabel('$\frac{t}{\tau}$','fontsize',15,'interpreter','latex')
122         axis square
123         set(gca,'fontsize',20)
124
125         subplot(9,1,5:7)
126         plot(ii(:,1),data(bounds(b(1),1):bounds(b(1),2),7),'-ok')
127         hold on
128         plot(jj(1,:)',data(bounds(b(2),1):bounds(b(2),2),7),'--sk')
129         axis square
130         set(gca,'fontsize',20)
131         xlabel('$\frac{t}{\tau}$','fontsize',15,'interpreter','latex')
132         ylabel('$\phi$','fontsize',15,'interpreter','latex')
133
134         s3 = subplot(9,1,9);
135         plot(NaN,NaN,'-ok')
136         hold on
137         plot(NaN,NaN,'--sk')
138         axis off
139
140         legend({ ['$' names{b(1)} '$'] ['$' names{b(2)} '$'] },'
              interpreter','latex','location','northoutside','Orientation','
              horizontal','fontsize',15)
141         print([SVGFolder names{b(1)} '_' names{b(2)} '_k'], '-deps')
142         clf
143     end
144 end
```

E.4 Eigen-decomposition Error

```
1  clear;clc;
2  ep = [.03 .03 .03; .02 .02 .02; .1 .1 .1];
3
4  K = 10^6;
5  err = zeros(K,1);
6  for i = 1:K
7      VGT = 8*rand(3)-4*ones(3);
8      VGTe = VGT+(2*ep*rand(3)-ep.*ones(3));
9
10
11     l1 = eig(VGT);
12     l2 = eig(VGTe);
13     L1 = max(unique(abs(imag(l1))));
```

```
14      L2 = max(unique(abs(imag(l2))));
15      err(i) = abs(L1-L2);
16  end
17  mean(err)
18  std(err)
```